Master's thesis

NTNU
Norwegian University of Science and Technology
Faculty of Natural Sciences
Department of Physics

Jostein Brunvær Steffensen

Developent of an improved B_0-shim method on the 7 tesla Magnetom Terra MRI scanner

Master's thesis in Physics
Supervisor: Pål Erik Goa
Co-supervisor: Desmond H. Y. Tse
May 2021

NTNU
Norwegian University of
Science and Technology

Jostein Brunvær Steffensen

Developent of an improved B_0-shim method on the 7 tesla Magnetom Terra MRI scanner

Master's thesis in Physics
Supervisor: Pål Erik Goa
Co-supervisor: Desmond H. Y. Tse
May 2021

Norwegian University of Science and Technology
Faculty of Natural Sciences
Department of Physics

NTNU
Norwegian University of
Science and Technology

Abstract

Magnetic Resonance Imaging relies on a highly homogeneous static magnetic field in order to avoid image distortion and signal loss. The process of correcting for small magnetic field variations is called B_0-shimming and can be performed by optimizing the currents given to the scanner's shim coils. These coils can superimpose a magnetic field that counteracts the underlying B_0-inhomogeneities. The aim of this project was to replace the vendor provided shim method on the Siemens' 7 tesla Magnetom Terra scanner, that have been found to be non-optimized. We developed a dual-echo gradient echo sequence to measure the underlying B_0-distribution, with the aim of making the conditions for each readout as similar as possible. The repetition time and gradient slew rate was adjusted to minimize the contribution of eddy currents occurring in the map. After the shim coils were calibrated, optimization codes from another project were availed to calculate the optimized shim current given to each coil. The calibration were done by representing each coil field by a linear sum of solid spherical harmonic functions up to 4th order. The finished shim procedure was compared against the vendor provided method by testing them on the brain of two unpaired groups of volunteers and conducting a Wilcoxon rank-sum test on the spread in the resulting B_0-map. The test results clearly states that the new shim method provided a significantly better shim than the one provided from the vendor.

Sammendrag

Magnetresonanstomografi avhenger av et svært homogent og statisk magnetfelt for å unngå bildeforvrenginger og tap av signalstyrke. Prosedyren som retter opp små variasjoner i skannerens hovedmagnetfelt kalles B_0-shimming, og kan gjennomføres ved å optimalisere strømmen som gis til skannerens shim-spoler. Disse shim-spolene generer magnetfelt som kan kombineres for å motvirke de underliggende B_0-inhomogenitetene. Målet med dette prosjektet var å erstatte leverandørens shim-metoden på Siemens' 7 tesla Magnetom Terra skanner, som har vist seg å ikke være optimalisert. Vi har utviklet en dobbel-ekko gradient-ekko sekvens for å måle variasjonene i B_0-feltet, med det underliggende målet om å gjøre utlesningen av de to ekkoene så like som mulige. Repetisjonstiden og endringshastigheten til gradientene ble justert for å minimalisere bidraget av eddy-strømmer i den resulterende B_0-kartet. Etter at skannerens shim-spoler var kalibrert, ble optimaliseringskoder fra et annet prosjekt benyttet for å beregne den optimale shim-strømmen til hver spole. Kalibreringen ble gjort ved å representere feltet fra hver shim-spole som en lineærkombinasjon av sfærisk-harmoniske funksjoner opp til 4. orden. Den endelige shim-prosedyren ble sammenlignet med metoden til leverandøren ved å teste dem på hjernen til to uparede grupper av frivillige og så utføre en Wilcoxon ranksum test på spredningen i det resulterende B_0-kartet. Resultatet fra testen konstaterer tydelig at den nye shim metoden er signifikant bedre en metoden fra leverandøren.

Preface

This thesis is a product of the two final semesters of the Master Program in Physics at the Norwegian University of Science and Technology (NTNU). I feel grateful to have gotten the opportunity to immerse in the complex and beautiful field of Magnetic Resonance Imaging. I would like to thank my supervisor Prof. Pål Erik Goa for his guidance and support during the course of the past year, especially in times when the project felt overwhelming. Together with Maria Tunset Grinde, Eivind Lysheim and Andreas Norum, we have met on the digital platform every week for many usefull discussions and input. Special thanks to Eivind, Andreas, Svein Åmdal and Rasmus Vikhamar-Sandberg for reading my thesis and giving valuable feedback. I would also like to thank Prof. Håkon Tjelmeland for our discussion on statistical analysis, Assoc. Prof. Johanna Vannesjo for tips on eddy current characterization, and Neil Peter Jerome for many useful and inspiring conversations on the MRI topic. At the end, I want to extend my deepest gratitude to my co-supervisor Desmond H. Y. Tse for his profound insight and valuable guidance throughout the year, especially during the first semester. Your skills and hard-working mentality have been truly inspiring.
Finally, I am deeply grateful for my family, friends and all the encouragement and support they give.

Contents

List of Figures

List of Tables

Abbreviations

ADC analog to digital converter. 10, 13, 14

FID free induction decay. 41

FOV field-of-view. 14, 30, 37

FWHM full with at half maximum. 32, 41, 70

GRE gradient recalled echo. 16, 24, 27, 73

MRI Magnetic Resonance Imaging. 1, 3, 5, 6, 83

NMR Nuclear Magnetic Resonance. 3, 33

QSM Quantitative susceptibility mapping. 24, 57, 71, 72

RF radio frequency. 6, 7, 10, 29

sdd standard deviation. 39

SH solid spherical harmonic. xi, 20, 22–24, 34, 36, 49

TE echo time. 16, 18, 19, 64

TR repetition time. 16, 67

VOI volume of interest. 1, 17, 20

1 Introduction

Magnetic Resonance Imaging (MRI) utilizes the magnetic resonance phenomenon to image internal organs for medical examination. This technique requires a strong external magnetic field, commonly called the B_0-field, magnetic gradients, radio waves and computational power. The strong B_0-field normaly has a magnitude of 1.5-3 T, but in recent years several 7 T scanners have been developed for research and medical examination purposes. The drive towards higher field strengths is motivated by potentially increased scanning speed, spatial resolution and better signal [1]. During the fall of 2019, a 7 T Siemens Magnetom Terra scanner was installed at the Norwegian University of science and technology in Trondheim.

In order to provide high quality images and correct information about the signal's spatial distribution, the magnetic B_0-field has to be as homogeneous as possible inside the volume of interest (VOI)[2, 3]. Possible inhomogeneities can originate from imperfections in the magnet construction, but are mainly caused by the subject under investigation during in vivo scans[4]. A material's susceptibility will determine its influence on the local magnitude of the magnetic field. Human tissue and bone are diamagnetic while the surrounding air is paramagnetic [4]. Areas where there is a sudden shift in the material's susceptibility, field distortions will occur and reduce the overall homogeneity of the field.

The process of correcting the small magnetic field deviations ΔB_0 is called *shimming*. In addition to the strong B_0-field originating from the scanner's superconducting magnet, the scanner is provided with several shim coils that can produce a variety of small magnetic fields. By giving each shim coil the optimal current, their superimposed shim field will minimize the size of ΔB_0. The 7 tesla Magnetom Terra scanner is equipped with 12 shim coils [5].

In 2020, Clark et. al. found that the default B_0-shimming method provided by Siemens for the Magnetom Terra scanner is not optimized [1]. By manually adjusting the shim coils they were able to make the shim fields better than the calculated ones. Since manually adjusted shims can be time consuming and dependent on the scanner operator, it is desirable to have an automated process that generates good shim values that are reproducible across volunteers and scanner operators.

This master project was part of a larger project at the Norwegian 7T MR Center aimed at establishing an improved B_0-shimming method to replace the vendor-provided auto-

matic or iterative method. The specific aims of this master project was:

1. Develop efficient and accurate B_0-mapping sequence.
2. Perform calibration of shim coils.
3. Compare in-house B_0-shimming method to vendor-provided method.

2 Theory and background

This chapter will give a general introduction to Magnetic Resonance Imaging (MRI), and then move on to B_0-mapping, shimming, shim-coil calibration, and shim comparison.

2.1 Magnetic Resonance Imaging

2.1.1 Nuclear Magnetic Resonance

When atomic nuclei are placed in a strong external magnetic field, we observe a splitting in energy levels that depend on the spin of the nuclei and the strength of the magnetic field. By applying an electromagnetic wave with a frequency matching the nuclei "precessional" frequency, the nuclei can be excited to a higher energy state [6]. When relaxing back to its original state, a characteristic electromagnetic signal can be recorded. The phenomenon in which a nuclei is absorbing and emitting electromagnetic radiation due to an external magnetic field is the Nuclear Magnetic Resonance (NMR) phenomenon [7].

Precession and the Larmor equation

In classical physics, the magnetic moment $\boldsymbol{\mu}$ originates from charged particles moving in closed loops. Since these charged particles have mass, their orbiting motion also gives rise to an angular momentum $\mathbf{L}$ pointing in the same direction as $\boldsymbol{\mu}$ [8]. This electromagnetic and mechanical property is hence related by a constant factor and can be written as

$$\boldsymbol{\mu} = \gamma \mathbf{L} \tag{2.1}$$

where γ is a nucleus specific constant called the *gyromagnetic ratio* [9]. A magnetic moment $\boldsymbol{\mu}$ in magnetic field $\mathbf{B_0}$ will experience a torque $\mathbf{G}$ according to

$$\mathbf{G} = \boldsymbol{\mu} \times \mathbf{B_0}. \tag{2.2}$$

The torque will cause a change in the particle's angular momentum, since $\mathrm{d}\mathbf{L}/\mathrm{d}t = \mathbf{G}$. Taking the time derivative on both sides of (2.1) yields

$$\frac{\mathrm{d}\boldsymbol{\mu}}{\mathrm{d}t} = \gamma \mathbf{G}$$

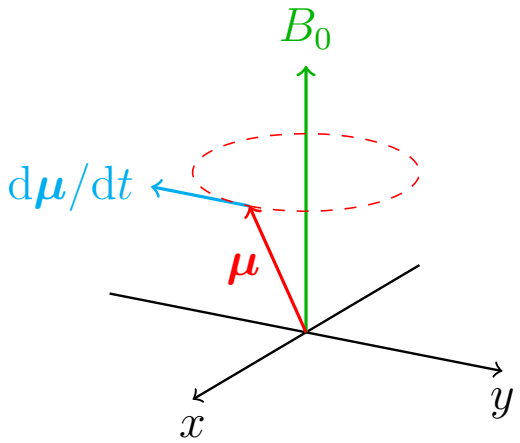

Figure 2.1: The magnetic moment $\boldsymbol{\mu}$ in a magnetic field B_0 pointed in the $\hat{\mathbf{z}}$ direction and the predicted $d\boldsymbol{\mu}/dt$. μ_x and μ_y will change such that $\boldsymbol{\mu}$ precess around B_0. The tip of $\boldsymbol{\mu}$ will follow the red dashed circle.

Combining with equation (2.2) gives a differential equation

$$\frac{d\boldsymbol{\mu}}{dt} = \gamma\boldsymbol{\mu} \times \mathbf{B_0} \tag{2.3}$$

describing the behaviour of the magnetic moment. A magnetic moment which is not parallel with the magnetic field, will experience a change in the direction perpendicular to both the magnetic field and the magnetic moment itself. This will result in precessional motion of the magnetic moment around the direction of the magnetic field (see figure 2.1). Solving the cross product in (2.3) gives the three equations:

$$\dot{\mu}_x = \gamma\mu_y B_0 \qquad \dot{\mu}_y = -\gamma\mu_x B_0 \qquad \dot{\mu}_z = 0 \tag{2.4}$$

Here, $\dot{\mu}$ denotes the time derivative of μ. In equation (2.4), the magnetic field vector is assumed to only have a component in the z direction: $\mathbf{B_0} = B_0\hat{\mathbf{z}}$. μ_z does not change with time and is hence equal to its initial configuration. When assuming that $\boldsymbol{\mu}$ has an angle θ with $\mathbf{B_0}$ at time zero, such that the initial condition of the magnetic moment is

$$\boldsymbol{\mu}(0) = |\boldsymbol{\mu}| \sin\theta\hat{\mathbf{x}} + |\boldsymbol{\mu}| \cos\theta\hat{\mathbf{z}},$$

the solutions to equation (2.4) are

$$\mu_x(t) = |\boldsymbol{\mu}| \sin\theta \cos(\gamma B_0 t) \qquad \mu_y(t) = |\boldsymbol{\mu}| \sin\theta \sin(\gamma B_0 t) \qquad \mu_z(t) = |\boldsymbol{\mu}| \cos\theta \tag{2.5}$$

The z-component of $\boldsymbol{\mu}$ is constant in time, while the x- and y-component will oscillate and cause $\boldsymbol{\mu}$ to precess around $\hat{\mathbf{z}}$ with the frequency γB_0. This is called the Larmor frequency ω_0.

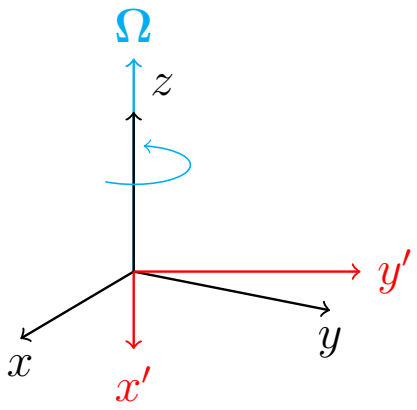

Figure 2.2: The two reference systems. The stationary lab frame and the rotating frame with primed coordinates. The primed frame is rotating counterclockwise with angular velocity $\mathbf{\Omega}$.

$$\omega_0 = \gamma B_0. \tag{2.6}$$

When the gyromagnetic ratio and the magnetic field is known, the wave frequency needed to excite the particle at interest can be calculated. In MRI we are mainly looking at protons, since protons are spin-1/2 particles and therefore have two energy states. Using the classical model above, the angular momentum comes from the protons *spin* and the magnetic moment from its charge moving at the surface.

2.1.2 Rotational reference frame

Introducing the rotating reference frame will be helpful further on in the MRI discussion [6]. The idea is that spins precessing with the Larmor frequency will be fixed in the rotating reference frame, while spins that are off-resonance will move.
A primed coordinate system, the *rotating frame of reference*, rotate around $\mathbf{\Omega}$ counterclockwise with angular velocity $|\mathbf{\Omega}| = \omega$. $\mathbf{\Omega}$ is a fixed vector in the fixed coordinate system, *the lab frame*, parallel with the z-axis (see figure 2.2). The rate of change of the magnetic moment, $(\mathrm{d}\boldsymbol{\mu}/\mathrm{d}t)'$, in the rotating frame, can be shown to follow the equation [6]

$$\left(\frac{\mathrm{d}\boldsymbol{\mu}}{\mathrm{d}t}\right)' = \gamma\boldsymbol{\mu} \times \mathbf{B}_{eff} \tag{2.7}$$

where $\mathbf{B}_{eff} = \mathbf{B_0} + \frac{\mathbf{\Omega}}{\gamma}$(Appendix A). If the primed frame rotate in the same direction as the precession of the magnetic moment with an angular velocity of ω, this is the same as setting $\mathbf{\Omega} = -\omega\hat{\mathbf{z}}$[1]. Using the fact that $\gamma\mathbf{B_0} = \omega_0\hat{\mathbf{z}}$, the equation of motion for $\boldsymbol{\mu}$ in

[1]Note that if $\mathbf{\Omega}$ and $\mathbf{B_0}$ are antiparallel, the rotation of the primed reference frame and the precession

the rotating frame of reference can then be written as

$$\left(\frac{\mathrm{d}\boldsymbol{\mu}}{\mathrm{d}t}\right)' = \boldsymbol{\mu} \times ([\omega_0 - \omega]\hat{\mathbf{z}}) \tag{2.8}$$

We see from equation (2.8) that when the rotating frame's angular velocity ω is equal to the Larmor frequency ω_0, $\boldsymbol{\mu}$ will be fixed in the rotating frame. When there are spatial variations in the main magnetic field, ω_0 will also vary, leading to precession around $\hat{\mathbf{z}}$ in the rotating frame.

2.1.3 Tipping of spins

The energy E of a magnetic moment $\boldsymbol{\mu}$ in a magnetic field $\mathbf{B_0}$ is given by

$$E = -\boldsymbol{\mu} \cdot \mathbf{B_0} \tag{2.9}$$

and therefore minimizes its energy by alignment with the external field [8]. Equation (2.3) implies that there will be no precession when this is the case. Precession is necessary in order to get an oscillating magnetic field that can be recorded by a receiver coil.

To move the magnetic moment away from $\hat{\mathbf{z}}$ into the transverse plane, a radio frequency (RF) magnetic field $\mathbf{B_1}$ is added for a brief time period [6]. In the rotating frame, the RF-field should be fixed in the xy-plane in order to make the magnetic moment precess around it and hence "flip" it away from the $\hat{\mathbf{z}}$-axis. In most MRI experiments, this is done by using a RF-field that is circularly polarized [6][2]. The act of applying a RF-field to tip the spins is called *excitation* of the spins [9]. Since the RF-field is only on for a short time, it is commonly called an RF-pulse or excitation pulse.

A circularly polarized magnetic field can be made by adding two linearly polarized fields with the same frequency and peak amplitude, but perpendicular and 90° out of phase with respect to each other [6]

$$\mathbf{B_1} = b_1(\hat{\mathbf{x}}\cos\omega t - \hat{\mathbf{y}}\sin\omega t) \tag{2.10}$$

where b_1 is the amplitude and ω the rotational frequency of the RF-pulse. From a rotating frame, rotating clockwise with angular velocity ω, the $\hat{\mathbf{x}}'$-axis can be related to the lab frame with the formula

$$\hat{\mathbf{x}}' = \hat{\mathbf{x}}\cos\omega t - \hat{\mathbf{y}}\sin\omega t$$

and hence the $\mathbf{B_1}$ field is stationary along the $\hat{\mathbf{x}}'$-axis in the rotating frame:

$$\mathbf{B_1} = b_1\hat{\mathbf{x}}'. \tag{2.11}$$

of the magnetic moment are going in the same direction.

[2]Here, polarization refers to the direction of change of the magnetic field.

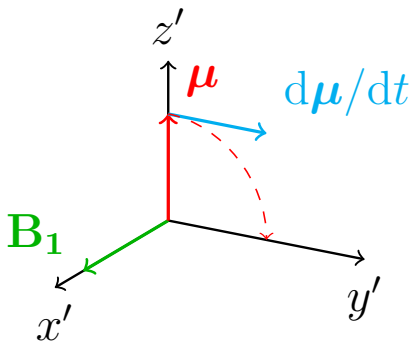

Figure 2.3: Rotating frame with $\mathbf{B_1}$ and $\boldsymbol{\mu}$.

Including the new RF-field, the effective magnetic field $\mathbf{B}_{eff}$ is now

$$\mathbf{B}_{eff} = \mathbf{B_0} - \frac{\omega}{\gamma}\hat{\mathbf{z}} + \mathbf{B_1}$$

and therefore changes the equation of motion for the magnetic moment in the rotating frame:

$$\begin{aligned}\left(\frac{\mathrm{d}\boldsymbol{\mu}}{\mathrm{d}t}\right)' &= \gamma\boldsymbol{\mu} \times (\mathbf{B_0} - \frac{\omega}{\gamma}\hat{\mathbf{z}} + \mathbf{B_1}) \\ &= \boldsymbol{\mu} \times ([\omega_0 - \omega]\hat{\mathbf{z}} + \omega_1\hat{\mathbf{x}}') \end{aligned} \tag{2.12}$$

where $\omega_1 = \gamma b_1$ is the precession frequency generated by the RF-field. When the RF-field is rotating with Larmor frequency ($\omega = \omega_0$), the effective field in the $\hat{\mathbf{z}}$-direction disappears, and the $\mathbf{B_1}$-field is in the best position to flip $\boldsymbol{\mu}$ around $\hat{\mathbf{x}}$:

$$\left(\frac{\mathrm{d}\boldsymbol{\mu}}{\mathrm{d}t}\right)' = \omega_1\boldsymbol{\mu} \times \hat{\mathbf{x}}' \tag{2.13}$$

Since the $\mathbf{B_1}$-field is only applied for a brief period in the form of a short pulse, the amplitude and duration will determine how far the magnetic moment will be flipped away from the $\hat{\mathbf{z}}$-axis. If the applied field is $\mathbf{B_1} = b_1\hat{\mathbf{x}}'$ over the time period τ, the *flip angle* α is given by

$$\alpha = \gamma b_1 \tau = \omega_1 \tau \tag{2.14}$$

2.1.4 Magnetization and spin density

The NMR signal does not originate from a single atom and its magnetic moment alone, but from a collection of magnetic moments. In a volume V large enough to contain a large number of protons, but small enough for the external magnetic field to be approximately

constant, the *Magnetization* $\mathbf{M}$ is given as the sum of all magnetic moments inside the volume divided by the volume [10]

$$\mathbf{M} = \frac{1}{V}\sum_{\boldsymbol{\mu}\in V}\boldsymbol{\mu} \tag{2.15}$$

Hence, the magnetization vector at position $\mathbf{r}$ would depend on the number of protons at that position. When $\mathbf{M}(\mathbf{r})$ is aligned with the external magnetic field, its magnitude is equal to an equilibrium value $M_0(\mathbf{r})$. The value of M_0 is a trade-off between a spin-systems tendency to align with the external field and its ability to gain energy from other spins through thermal contact and is given by [6]

$$M_0(\mathbf{r}) = \frac{1}{4}\rho_0(\mathbf{r})\frac{\gamma^2\hbar^2}{kT}B_0 \tag{2.16}$$

where $\hbar$ is the Planck constant divided by 2π, k is the Boltzmann constant and $\rho_0(\mathbf{r})$ is the spin density at position $\mathbf{r}$. A higher value for ρ_0 will give a higher value of M_0 and a potentially higher signal when $\mathbf{M}$ is flipped away from the $\hat{\mathbf{z}}$ -axis. The local spin density will therefore contribute to determining the local signal strength and thereafter the image contrast. A derivation of (2.16) is done in appendix B.

2.1.5 Relaxation

The spin density, ρ_0, is not the only factor determining the contrast in an image. There are also two relaxation processes taking place, affecting the available signal. The equation of motion for a single magnetic moment in a magnetic field (2.3), can be extended to apply for the magnetization. Starting with

$$\frac{\mathrm{d}\boldsymbol{\mu}}{\mathrm{d}t} = \gamma\boldsymbol{\mu}\times\mathbf{B_0}$$

and then sum over all magnetic moments inside a volume element V and divide by the size of this volume

$$\frac{1}{V}\sum_{\boldsymbol{\mu}\in V}\frac{\mathrm{d}\boldsymbol{\mu}}{\mathrm{d}t} = \frac{\gamma}{V}\sum_{\boldsymbol{\mu}\in V}\boldsymbol{\mu}\times\mathbf{B_0},$$

gives a differential equation for the magnetization resembling the one for a single magnetic moment

$$\frac{\mathrm{d}\mathbf{M}}{\mathrm{d}t} = \gamma\mathbf{M}\times\mathbf{B_0}. \tag{2.17}$$

Equation (2.17) is the equation of motion for the magnetization if the protons spin are non-interacting. In this case, $\mathbf{M}$ will be precessing forever. When interactions are

included, $\mathbf{M}$ will decay back to align with the external magnetic field. This decay process is called relaxation and require an extra term to be added to (2.17) [6]

$$\frac{\mathrm{d}\mathbf{M}}{\mathrm{d}t} = \gamma\mathbf{M} \times \mathbf{B_0} - \begin{bmatrix} M_x/T_2 \\ M_y/T_2 \\ (M_0 - M_z)/T_1 \end{bmatrix} \tag{2.18}$$

This equation is referred to as *the Bloch equation* for a magnetic field pointing in the $\hat{\mathbf{z}}$ direction. The parameters $1/T_1$ and $1/T_2$ are proportionality constants determined by the tissue type. These constants contribute to determine the contrasts in the image. There are two relaxation processes governing the magnetization. We will look at them by decomposing the $\mathbf{M}$ into a transverse and a longitudinal component. The longitudinal component is

$$M_{\parallel} = M_z$$

while the transverse component includes both M_x and M_y

$$\mathbf{M}_{\perp} = M_x\hat{\mathbf{x}} + M_y\hat{\mathbf{y}}$$

Longitudinal relaxation

After an RF-pulse is applied and the magnetization is tipped into the xy-plane, $M_z = 0$, but it will gradually relax back to the equilibrium value. This relaxation process is called *longitudinal relaxation* and is caused by fields from thermal agitation [11]. Viewed from the rotating reference frame, the cross product $\mathbf{M} \times \mathbf{B_0}$ is equal to zero, leaving us with the relaxation term only

$$\frac{\mathrm{d}M_{\parallel}}{\mathrm{d}t} = \frac{1}{T_1}(M_0 - M_z). \tag{2.19}$$

Solving this differential equation gives

$$M_z(t) = M_{z0}e^{-t/T_1} + M_0(1 - e^{-t/T_1}) \tag{2.20}$$

where M_{z0} is the initial state.

Transverse relaxation

We will not consider the direction of $\mathbf{M}_{\perp}$, only its magnitude $|\mathbf{M}_{\perp}| = M_{\perp}$. $M_{\perp}$ will undergo transverse relaxation due to spins experiencing different local fields. These fields are combinations of the applied field and the fields of their neighbors [6]. The deviations in local fields leads to different local precessional frequencies, the spins tend to "fan out" and $M_{\perp}$ is reduced. The relaxation process can be described by [6]

$$\frac{\mathrm{d}M_{\perp}}{\mathrm{d}t} = -\frac{1}{T_2}M_{\perp} \tag{2.21}$$

with the solution

$$M_\perp(t) = M_\perp(0)e^{-t/T_2} \tag{2.22}$$

The process of "fanning out" is often referred to as *dephasing*.

T_2^* and T_2'

The dephasing caused by the T_2 parameter are due to local, random, time-dependent field variations and are not recoverable. In addition to this, there is also dephasing caused by the external field inhomogeneities that can be characterized with a separate decay time T_2'. The total relaxation factor T_2^* is given by

$$\frac{1}{T_2^*} = \frac{1}{T_2} + \frac{1}{T_2'} \tag{2.23}$$

It is possible to remove the contribution from T_2' through an imaging sequence called *spin echo*.

2.1.6 The signal

If all protons are excited simultaneously, they will collectively precess and make an oscillating magnetic field that can be recorded with a receiver coil. Due to T_2-relaxation, the signal will fade away after a short period. The signal in the time and frequency domain can be displayed as seen in figure 2.4a. If additional inhomogeneities in the B_0-field are present, either in the form of magnet imperfections or magnetic susceptibility differences in the sample, the signal will relax with the T_2^* constant [12]. Since T_2^* is smaller than T_2, the signal will decay much faster and also leave a wider resonance peak due to the wider span in precessional frequencies (figure 2.4b).

The transverse magnetization in equation (2.22) can be represented with the complex notation

$$M_\perp(t, \mathbf{r}) = M_\perp(0, \mathbf{r})e^{-t/T_2(\mathbf{r})}e^{i\phi(t,\mathbf{r})} \tag{2.24}$$

when viewed from the labframe at position $\mathbf{r}$. $\phi(t, \mathbf{r})$ is the accumulated phase from precession after the excitation pulse, and $M_\perp(0, \mathbf{r})e^{-t/T_2(\mathbf{r})}$ is the the magnitude. This magnitude can be rewritten as

$$M_\perp(0, \mathbf{r})e^{-t/T_2(\mathbf{r})} = M_\perp(\mathbf{r}, t, \alpha) \tag{2.25}$$

since the initial magnitude of the transverse magnetization $M_\perp(0, \mathbf{r})$ will depend on the RF flip angle, α.

The signal from precessing magnetization is detected by a receiver coil and discretely sampled with an analog to digital converter (ADC). The receiver removes the Larmor

frequency of the transverse magnetization through a process called *demodulation*. This is the same as measuring the phase from the rotating reference frame.

The complex demodulated signal recorded from the scanner at time t after the RF excitation can be written as an integral over the complex transverse magnetization

$$s(t) = \omega_0 \Lambda \mathcal{B}_\perp \int d^3 r M_\perp(\mathbf{r}, t, \alpha) e^{i[\Omega t + \phi(\mathbf{r},t)]} \tag{2.26}$$

where Ω is the demodulation frequency, Λ is a constant that include the gain factors from the electronic detection system and $\mathcal{B}_\perp$ is the receive field amplitude [6]. $\phi(\mathbf{r}, t)$ is the accumulated phase of the magnetization vector during the time t

$$\phi(\mathbf{r}, t) = -\int_0^t dt' \omega(\mathbf{r}, t'). \tag{2.27}$$

The negative sign is due to the precession of $\mathbf{M}$ being clockwise. In equation (2.26) transmitting and receiving RF coils are assumed to be sufficiently uniform for $\mathcal{B}_\perp$ to be independent of position. For a RF pulse with flip angle α,

$$M_\perp(\mathbf{r}, t, \alpha) = M_0(\mathbf{r}) F(\mathbf{r}, t, \alpha) \tag{2.28}$$

where F is a sequence dependent relaxation factor [12]. Combining equation (2.16), (2.26) and (2.28) gives the expression

$$s(t) = \int d^3 r \rho(\mathbf{r}, t, \alpha) e^{i[\Omega t + \phi(\mathbf{r},t)]} \tag{2.29}$$

for the signal, where

$$\rho(\mathbf{r}, t, \alpha) = \frac{1}{4} \omega_0 \Lambda \mathcal{B}_\perp \rho_0(\mathbf{r}) \frac{\gamma^2 \hbar^2}{kT} B_0 \cdot F(\mathbf{r}, t, \alpha)$$

is the effective spin density.

2.1.7 Spatial encoding and k-space

The signal contains information about all excited protons within the body, but no information about their spatial distribution. In order to image, the signal has to be *spatially encoded*. In addition to the superconducting magnetic field of 7 T, the scanner is also equipped with three gradient coils. These coils can superimpose a small linear variation of the main magnetic field along the x, y and z direction. The gradients gives the ability to locally vary the precessional frequencies inside the volunteer. In the following derivations, the time and flip angle dependence of the effective spin density will be left out for simplicity.

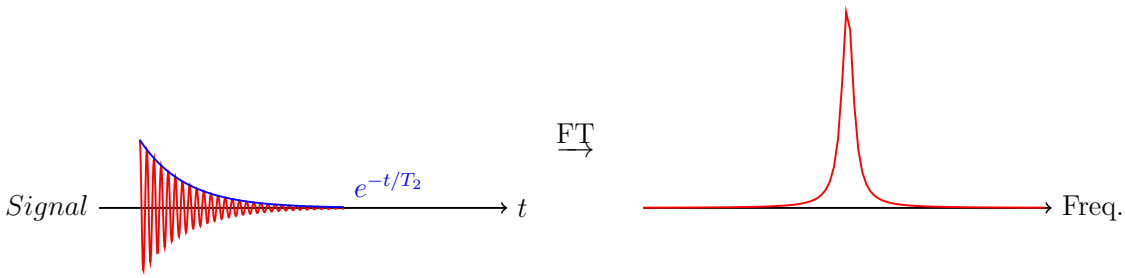

(a) The FID signal in a perfect homogeneous B_0-field decays with the T_2 constant. A Fourier transformation (FT) of the signal gives the distribution of precession frequencies.

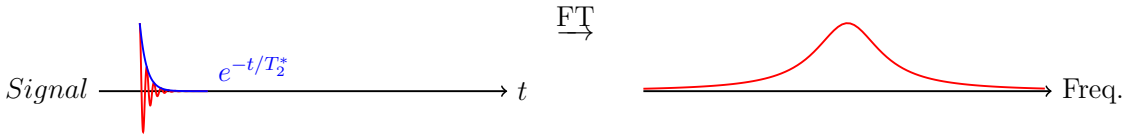

(b) When the external B_0-field is inhomogeneous and when susceptibility differences in tissue are taken into account, the FID signal decays with the T_2^* constant. This signal will decay faster than with the T_2-constant and hence leave a wider peak in the frequency domain.

Figure 2.4

1D imaging and Frequency encoding

We will start by looking at imaging in one dimension. The signal equation is then

$$s(t) = \int dz \rho(z) e^{i[\Omega t + \phi(z,t)]} \tag{2.30}$$

We know from the Larmor equation (2.6) that the precessional frequency depends on the magnetic field magnitude. By turning on the linear gradient in the z direction, the total field along z is

$$B_z(z,t) = B_0 + zG_z(t)$$

with $G_z = \partial B_0/\partial z$. Now, there is a specific frequency associated with every position along the z-axis

$$\omega(z,t) = \omega_0 + \gamma z G_z(t) \tag{2.31}$$

and the axis is then said to be *frequency encoded*. In this case, a perfect B_0-field is assumed, such that $\omega(z,t) = \omega_0$ when the gradient is turned off. Inserting (2.31) into equation (2.27) gives ,

$$\phi(z,t) = -\int_0^t dt'(\omega_0 + \gamma z G_z(t)) \tag{2.32}$$

$$= -\omega_0 t - \int_0^t dt' \gamma z G_z(t')$$
$$= -\omega_0 t - z\gamma \int_0^t dt' G_z(t').$$

Introducing

$$k(t) = \gamma \int_0^t dt' G(t') \tag{2.33}$$

with $\gamma = \gamma/2\pi$, the phase is given by

$$\phi(z,t) = -\omega_0 t - 2\pi z k(t). \tag{2.34}$$

Inserting this into the signal equation (2.30) and setting Ω to match ω_0 yields

$$s(t) = \int dz \rho(z) e^{i[\omega_0 t - \omega_0 t - 2\pi z k(t)]}$$
$$s(k) = \int dz \rho(z) e^{-i2\pi z k} \tag{2.35}$$

and the signal appears to be the Fourier transformation of the effective spin density.

3D imaging and phase encoding

It is possible to extend k-space to three dimensions in order to find the effective spin density in the two remaining dimensions. We will start by extending the signal equation to three dimensions:

$$s(\mathbf{k}) = \int d^3 r \rho(\mathbf{r}) e^{-i2\pi \mathbf{r}\cdot\mathbf{k}} \tag{2.36}$$

where $\mathbf{k} = k_x\hat{\mathbf{x}} + k_y\hat{\mathbf{y}} + k_z\hat{\mathbf{z}}$ is given by the three gradient integrals

$$k_x(t) = \gamma \int_0^t dt' G_x(t') \qquad k_y(t) = \gamma \int_0^t dt' G_y(t') \qquad k_z(t) = \gamma \int_0^t dt' G_z(t'). \tag{2.37}$$

$\int_0^t dt' G(t')$ is called *the gradient moment*. By independently varying the G_x, G_y and G_z gradient, it is possible to sweep over k-space and fill the data "cuboid" with measured signal. A visualization of the connection between the gradient pulses and the position in k-space is shown in figure 2.6, and a description of the gradient stages is shown in figure 2.5.

To fill a data line in the k_x-direction in k-space, the G_x-gradient and the ADC has to be on simultaneously. As the k-space line is traversed, the ADC sample the changing values of $s(\mathbf{k})$ and store them as discrete values in the respective line. For a rectangular gradient lobe, the discrete k-space step in the x-direction, Δk_x, is given like

$$\Delta k_x = \gamma G_x \Delta t \tag{2.38}$$

Figure 2.5: Description of the gradient stages.

according to equation 2.37. Δt is the uniform time interval between each sampling done by the ADC. The sampling rate $1/\Delta t$ is called the *receiver bandwidth*.
When N_x samples are collected, the field-of-view (FOV) of k_x will be

$$\text{FOV}_{k_x} = N_x \Delta k_x. \tag{2.39}$$

In order to fill all k_x-lines in the $k_y k_z$-plane, the G_y and G_z gradient are turned on for a short duration τ before every sampling. This gives an additional phase-offset to the spins linearly varying along the y and z direction, and also changes the value of k_y and k_z. By changing the amplitude of G_y and G_z before every sampling, the whole k-space cuboid can be filled with signal data. Δk_y and Δk_z are given by

$$\Delta k_y = \gamma \Delta G_y \tau \qquad \Delta k_z = \gamma \Delta G_z \tau \tag{2.40}$$

where ΔG_y and ΔG_z are the change in gradient amplitude between each line filling in k-space. When a total of N_y and N_z increments are done, the FOVs in the k_y and k_z direction are given by

$$\text{FOV}_{k_y} = N_y \Delta k_y \qquad \text{FOV}_{k_z} = N_z \Delta k_z \tag{2.41}$$

The process of turning on the gradients for a short time such that the phase of the spin linearly varies along some spatial direction is called *phase encoding*. Taking the inverse 3D-Fourier transformation of the k-space cuboid

$$\rho(\mathbf{r}) = \int d^3k s(\mathbf{k}) e^{i2\pi \mathbf{r}\cdot\mathbf{k}} \tag{2.42}$$

gives the effective spin-density in three dimensions. The spacing between the datapoints in k-space, Δk, is inversely proportional to the respective spatial dimensions, or FOV in image space [13].

2.1.8 The pulse sequence

MRI can produce different contrasts in the image by controlling the timing of the RF-pulses, the gradients and the ADC components. The arrangement of the different components is called a *pulse sequence*. There are mainly two pulse sequence families: The

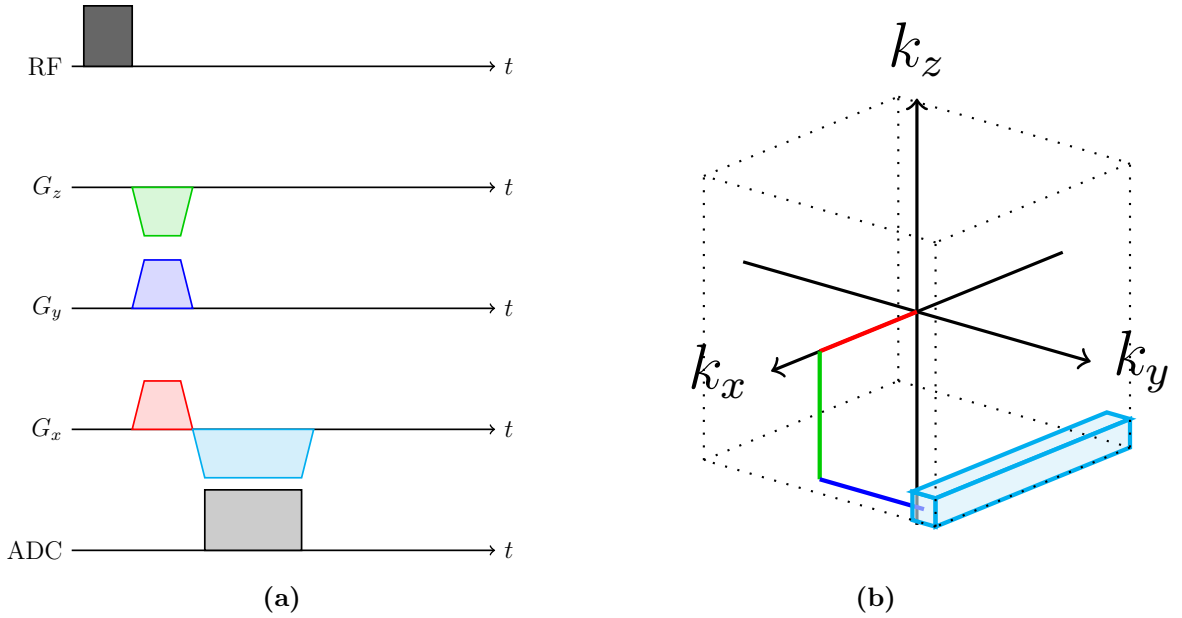

Figure 2.6: An example of how k-space can be traversed by applying the magnetic field gradients. (a) Shows the timing of the RF, gradients and ADC in a sequence diagram. (b) Shows how $\mathbf{k}$ is changed with the applied gradients in (a). The cyan cuboid indicates what the values of $\mathbf{k}$ were when the ADC was turned on. In this line, the discrete values of $s(\mathbf{k})$ are stored. To fill all lines in k-space, the amplitude of G_z and G_y are varied during the MRI sequence. This is the phase encoding.

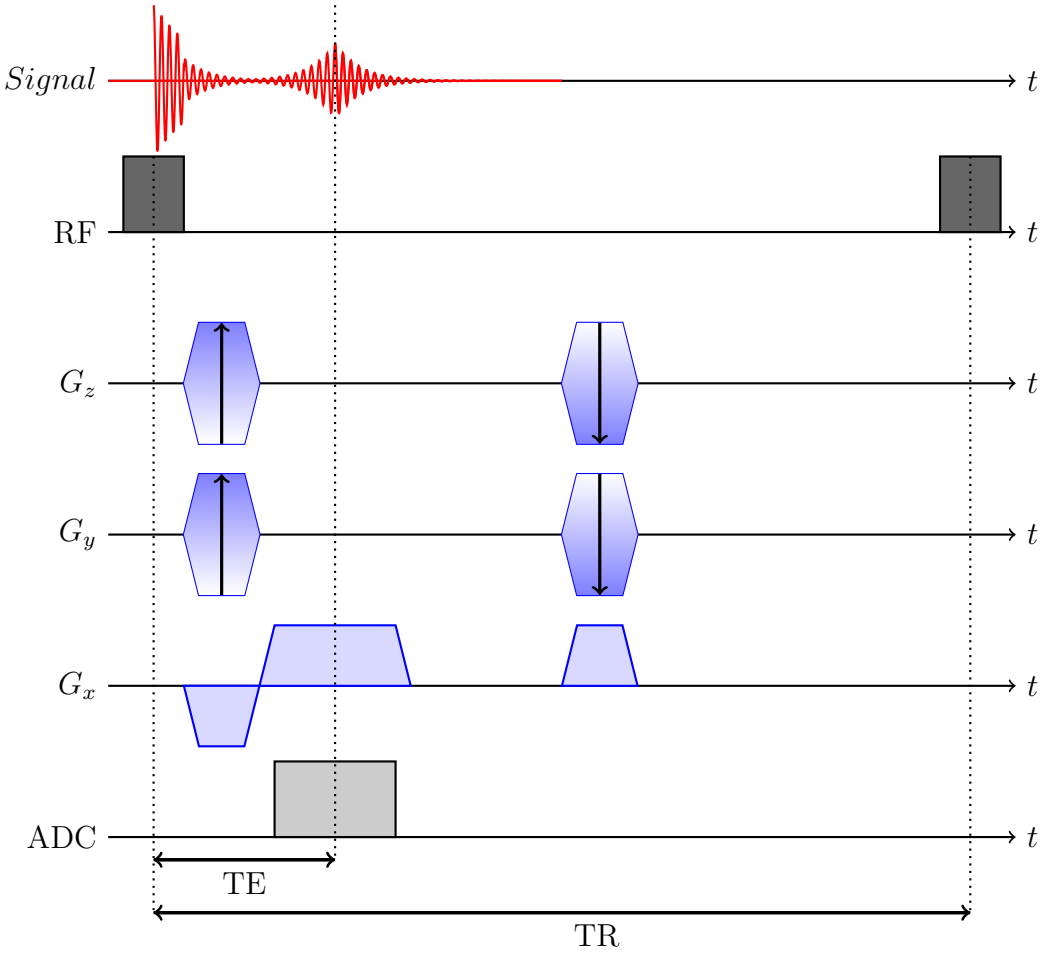

Figure 2.7: A pulse sequence diagram for the gradient echo sequence. The phase encoding gradient pulses are illustrated with a color gradient to indicate the change in amplitude.

spin echo and the gradient recalled echo (GRE). We will later modify a GRE sequence for mapping of the B_0-distribution. For a 3D GRE, there are two phase encoding gradients. Before the the readout, the readout gradient prephase the transverse magnetization, while the phase encoding gradients are turned on. The magnetization is then rephased to form an echo that is measured by the ADC. After the readout, the phase encoding gradients are turned on again, but with opposite polarity, to remove the linearly varying phase-offsets. In addition, a spoiler gradient is applied in the readout direction. A pulse diagram is shown in figure 2.7. Here, the echo time (TE), is the time from the center of the excitation pulse to the center of the echo, while the repetition time (TR) is the time between successive excitation pulses. A derivation of the relaxation factor for the GRE sequence is done in appendix C.

Spoilers

If the residual transverse magnetization is not eliminated after a readout, the signal will effect the subsequent readout and produce artifacts. *The spoiler gradient* dephases the MR-signal by speeding up the transverse relaxation and is commonly applied at the end of each repetition period. The gradient moment of the spoiler gradient is usually very large so it can adequately dephase the residual transverse magnetization [14].

Eddy currents

The time varying field from changing gradients will induce current in nearby conducting structures according to Faraday's law, $\nabla \times \mathbf{E} = -\frac{\partial \mathbf{B}}{\partial t}$. These structures include the magnet, the gradient coils themselves and the RF coils. The generated currents are called *eddy currents*. According to Lenz's law, the eddy currents give rise to time varying magnetic fields which opposes the magnetic field that caused them [14]. The build up of eddy currents are proportional to the gradient's slew rate, i.e. the rate of change of the gradient, $\frac{\mathrm{d}\mathbf{G}}{\mathrm{d}t}$. A component of an eddy current, $\mathcal{E}(t)$, at observation time t can be expressed as:

$$\mathcal{E}(t) = -\int_0^t \alpha \frac{\mathrm{d}G}{\mathrm{d}t'} \cdot e^{-\beta(t-t')} dt' \tag{2.43}$$

were α is an amplitude term, $1/\beta$ is the time constant of the eddy current and $(t - t')$ is the time delay between eddy current generation and observation [15]. When the gradient is not changing, the eddy currents consist of multiple components that each decay exponentially with different time constants:

$$\mathcal{E}(t) = \mathcal{E}(t_R) \cdot e^{-\beta(t-t_R)} \tag{2.44}$$

Here t_R is time of the end gradient ramp [15]. An approximation of the eddy current generation and decay for a trapezoidal gradient is shown in figure 2.8. Magnetic fields from eddy currents will influence the phase accumulation in the image. In addition, these fields can lead to a shift in k-space if present in the readout direction. For applications depending on accurate phase images, the presence of eddy currents can lead to artifacts.

2.2 B_0-mapping

2.2.1 Homogeneous B_0-field

In order to acquire high quality images and provide correct spatial mapping, the main magnetic field has to be as homogeneous as possible inside the volume of interest (VOI). Although imperfections in the scanner's manufacturing process can have an influence on the magnetic field homogeneity, the majority of inhomogeneties in-vivo are caused by the sample itself [4]. The material's susceptibility governs its effect in the magnetic field.

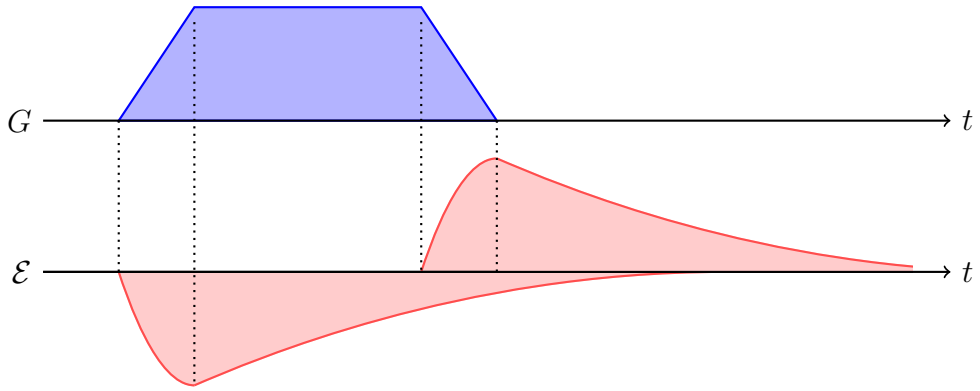

Figure 2.8: The generation and decay of an eddy current ($\mathcal{E}$) for a trapezoidal gradient pulse (G).

Human tissue and bone are diamagnetic, while the surrounding air is paramagnetic, which leads to transition zones were the B_0-field magnitude gets a strong gradient. For brain imaging, the largest susceptibility differences occur between brain tissue an the nasal and auditory passages [4].

2.2.2 B_0-mapping

The process of estimating the magnetic field off-sets $\Delta B_0(x, y, z)$ is called B_0-mapping. From the Larmor equation (2.6), we know that the Larmor frequency depends on the local magnetic field. Off resonances due to B_0-inhomogeneities will give an unintended phase offset. After collecting the image raw-data, a Fourier transformation will transform the data from k-space to image-space. Each voxel in the image is associated with a complex number with both a magnitude and a phase [14]. If two images are taken with slightly different echo times, the accumulated phase can be found by comparing the two images voxel-vise.

Assume two images with N voxels each. For an arbitrary voxel $n \in N$ there is an associated complex number

$$Z_1 = \mu_1 e^{i\phi_1}$$

and

$$Z_2 = \mu_2 e^{i\phi_2}$$

for image 1 and 2 respectively. Assuming image 1 has an echo time TE_1 and image 2 TE_2, the phase can be calculated from the Larmor equation

$$\phi_1 = \gamma \Delta B_0 \mathrm{TE}_1 \qquad \phi_2 = \gamma \Delta B_0 \mathrm{TE}_2 \tag{2.45}$$

By subtracting ϕ_2 from ϕ_1 and rearrange, we get an equation for the magnetic field in voxel n

$$\Delta B_0(n) = \frac{\Delta\phi}{\gamma \Delta \mathrm{TE}} \tag{2.46}$$

where $\Delta\phi$ is the phase difference $\phi_2 - \phi_1$ and $\Delta\mathrm{TE} = \mathrm{TE}_2 - \mathrm{TE}_1$. The phase difference can be calculated from the four-quadrant arctan function,

$$\Delta\phi_{wrapped} = \mathrm{ATAN2}[\mathrm{Im}(Z_1 Z_2^*), \mathrm{Re}(Z_1 Z_2^*)] \tag{2.47}$$

Notice that ATAN2$[\cdot,\cdot]$ only calculates the *wrapped* phase difference[3]. This means that a phase difference outside the $[-\pi, \pi]$ interval will be wrapped back to this interval and give a wrong B_0 measurement. In order to be used in (2.46) the phase difference has to be unwrapped.

Choice of ΔTE

The phase difference in the B_0-mapping sequence is based on the assumption of a single resonance frequency, which is not the case in lipid rich tissue. The signal at voxel $\mathbf{r}$ can be expressed as a sum over n different signal components

$$S(\mathbf{r}, \mathrm{TE}) = \sum_{i=1}^{n} a_i e^{-i\mathrm{TE}[\gamma \Delta B_0(\mathbf{r}) + 2\pi\Delta f_i]} e^{-\mathrm{TE}/T_{2i}^*} \tag{2.48}$$

where a_i, T_{2i}^* and Δf_i is the amplitude, relaxation constant and offset frequency of signal component i [16]. Under these conditions, equation (2.46) no longer holds for arbitrary ΔTE's. Nevertheless, it is still possible to make the phase difference proportional to ΔB_0 by making sure water and fat have the same phase in both images. This can be done by setting ΔTE equal to a multiple inverse of the water-lipid frequency separation $k/\Delta f_{wf} = k/(\Delta f_w - \Delta f_f)$ [16], where $k \in \mathbb{N}$. Here Δf_w and Δf_f are the off-resonance frequencies of water and fat respectively. The water peak is located at approximately 4.7ppm (parts per million) while the signal from fat is generally assumed to be dominated by the methylene lipid at 1.3ppm [16]. This gives Δf_{wf} the numerical value

$$\Delta f_{wf} = \left(\frac{4.7 - 1.3}{10^6}\right) \frac{\gamma}{2\pi} B_0 \approx 1013.4\mathrm{Hz} \tag{2.49}$$

with $\gamma/2\pi = 42.58$ MHz$\cdot$T^{-1} and $B_0 = 7$ T. In this project, the value of ΔTE was set to 1.98 ms, which is the same as using $k = 2$:

$$\Delta\mathrm{TE} = \frac{2}{1013.4\mathrm{Hz}} \approx 1.9735\mathrm{ms} \tag{2.50}$$

[3]The ATAN2$[\cdot,\cdot]$ function is essentially an arctan function that is valid inside the range $[-\pi, \pi]$ instead of only $[-\pi/2, \pi/2]$.

2.3 B_0-shimming and shim coil calibration

2.3.1 Shimming

The scanner is provided with additional coils that can compensate for changes in the magnetic field. These coils are called *shim coils*. By adjusting the current going into each shim coil, the inhomogenities ΔB_0 within the VOI can be minimized. A magnetic field in free space can be shown to follow Laplace's equation (appendix D),

$$\nabla^2 \mathbf{B_0} = (\nabla^2 B_x, \nabla^2 B_y, \nabla^2 B_z) = \vec{0}$$

where the equation $\nabla^2 B_0 = 0$ is the only interesting one since $\mathbf{B_0} = B_0(x, y, z)\hat{\mathbf{z}}$ in the scanner. The solution to Laplace's equation can be expressed as a linear combination of the solid spherical harmonic (SH) functions:

$$\Delta B_0(r, \theta, \phi) = \sum_{n=0}^{\infty} \sum_{m=-n}^{n} I_n^m r^n P_n^{|m|}(\cos\theta) \cos\left(m\phi - \phi_n^m\right) \tag{2.51}$$

Here, ΔB_0 is the magnetic field offsets expressed in spherical coordinates r, θ and ϕ, I_n^m are the weighting of each SH-function and P_n^m are the associated Legendre polynomials of order n and degree. $\phi_n^m = 0$ for $m \geq 0$ and $\pi/2$ for $m > 0$ [13]. The scanner's shim coils are designed to generate these SH functions. By putting the right amount of current on each coil, I_n^m, the superimposed field can minimize the B_0-inhomogeneities.

For each order n there is a number of $2n + 1$ SH terms. The highest order of the SH present in the scanner is referred to as its shim capability. A scanner with a second order shim system has all first and second order shim coils. The 7 T Magnetom Terra scanner has a total of 12 shim coils[5], making it partly a third order shim system. The 12 solid spherical harmonic functions the Terra scanners shim coils intend to create are displayed in figure 2.9[4]. With the number of coils fixed, the shimming procedure reduces to finding the shim currents I_n^m given to each coil that minimizes the magnetic field offset.

If the magnetic field produced in the N voxels by each shim coil is mapped to a column vector in matrix $\mathbf{A}$, and the associated currents I_n^m given to each coil is arranged in a column vector $\mathbf{I}$, the combined field is given by

$$\mathbf{b_0^{coil}} = \mathbf{AI} \tag{2.52}$$

Here, $\mathbf{b_0^{coil}}$ is a vector containing the magnetic field generated by the shim coils in the N voxels. Row j in matrix $\mathbf{A}$ contains contributions from each of the different shim coils in voxel $j \in N$. Written out, the matrix equation in (2.52) will look as follow

[4]The single 0th order SH is not a coil, but a frequency adjustment of the excitation pulse and therefore not counted.

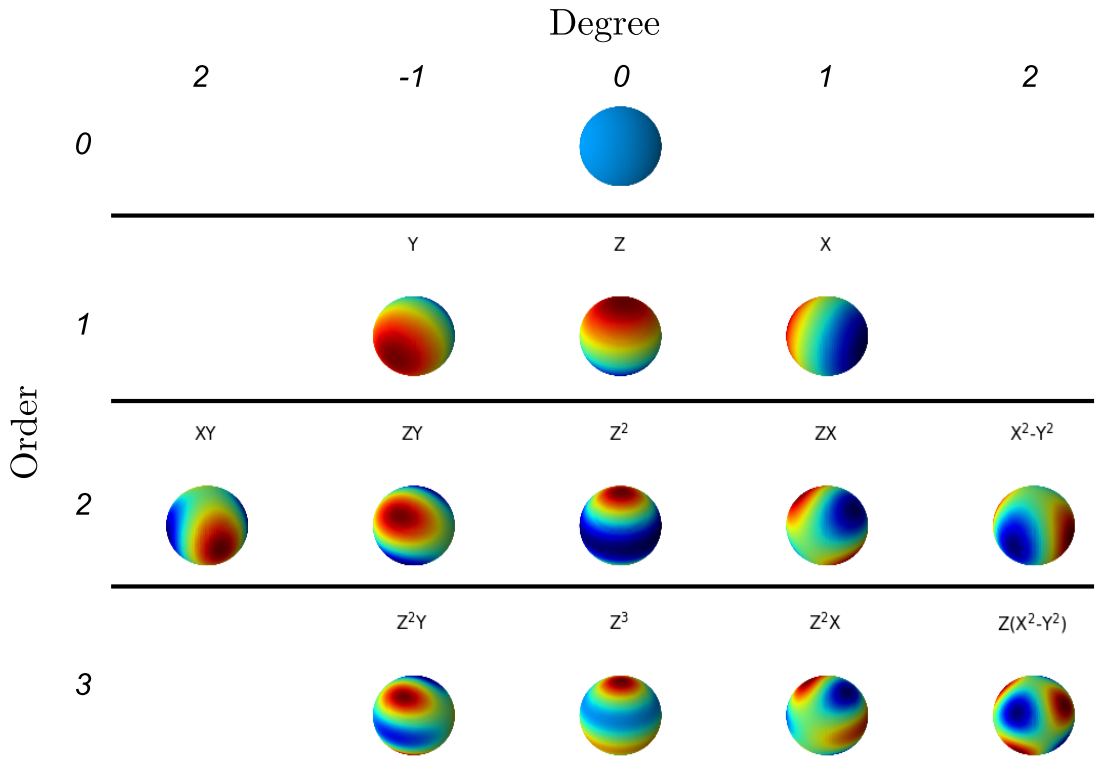

Figure 2.9: The available solid spherical harmonic fields on the 7T Magnetom Terra scanner.

$$\begin{bmatrix} B_1 \\ B_2 \\ \vdots \\ B_N \end{bmatrix}^{\mathbf{coil}} = \begin{bmatrix} A_{11} & A_{12} & \cdots & A_{1,12} \\ A_{21} & A_{22} & \cdots & A_{2,12} \\ \vdots & \vdots & \vdots & \vdots \\ A_{N1} & A_{N2} & \cdots & A_{N,12} \end{bmatrix} \begin{bmatrix} I_1^0 \\ I_1^1 \\ \vdots \\ I_3^2 \end{bmatrix} \tag{2.53}$$

If the measured ΔB_0 values from the mapping process is arranged in a vector $\mathbf{b_0}$, the shim currents can be calculated by solving the optimization problem

$$\min \left\| \mathbf{b_0} - \mathbf{b_0^{coil}} \right\| \tag{2.54}$$

where the i^{th} shim current I_i is subjected to some current limit $\|I_i\| \leq I_i^{lim}$ set by the vendor. If the shim currents applied during the B_0-mapping was $\mathbf{I_{old}}$, the new currents, $\mathbf{I_{new}}$ that will minimize equation (2.54) are related as follows:

$$\mathbf{I_{new}} = \mathbf{I_{old}} - \mathbf{I} \tag{2.55}$$

The new ΔB_0-field after shimming, $\mathbf{b_0^{shim}}$, is then

$$\mathbf{b_0^{shim}} = \mathbf{b_0} - \mathbf{b_0^{coil}}$$

Notice the dimensions of the different matrices:

- $\mathbf{b_0^{coil}}$, $\mathbf{b_0} \in \mathbb{R}^{N\times 1}$
- $\mathbf{A} \in \mathbb{R}^{N\times 12}$
- $\mathbf{I}$, $\mathbf{I_{old}}$, $\mathbf{I_{new}} \in \mathbb{R}^{12\times 1}$

2.3.2 Calibration of shim-coils

The calibration matrix

In equation (2.52) we assume the SH generated by the shim coils to be perfectly pure and orthogonal. This is not the case as most shim coils produce cross terms in addition to their primary shape [16]. If ignored, the calculated shim currents will not give the best shim field and more iterations of the optimization (2.54) are necessary. An alternative to this, is to represent the field produced by a shim coil with several SH-functions instead of one. This can be done by fitting the shim coils' field to SH-functions up to k^{th} order and store the information in a shim coil calibration matrix $\mathbf{W}$. This matrix can be related to the $\mathbf{A}$ matrix like so

$$\mathbf{A} = \mathbf{TW} \tag{2.56}$$

where $\mathbf{T}$ is a matrix describing the spatial distribution of k pure theoretical SH functions in the different voxels. Each of these k functions are represented as column vectors with length N in matrix $\mathbf{T}$. The shim coil calibration matrix $\mathbf{W}$ has one column vector for each of the shim coils. The column is not a description of the produced shim field in space, but rather a vector containing k weighting factors. One for each of the pure functions in matrix $\mathbf{T}$. The size of the weighting factors indicates how much a certain theoretical pure SH function is contributing to the field generated by one of the shim coils per one unit of current. Multiplication of $\mathbf{T}$ and $\mathbf{W}$ would give a shim field matrix $\mathbf{A}$ that accounts for the cross terms. The different matrix dimensions are as follows:

- $\mathbf{A} \in \mathbb{R}^{N\times 12}$
- $\mathbf{T} \in \mathbb{R}^{N\times k}$
- $\mathbf{W} \in \mathbb{R}^{k\times 12}$

Equation (2.56) in full matrix form:

$$\begin{bmatrix} A_{11} & A_{12} & \cdots & A_{1,12} \\ A_{21} & A_{22} & \cdots & A_{2,12} \\ \vdots & \vdots & \vdots & \vdots \\ A_{N1} & A_{N2} & \cdots & A_{N,12} \end{bmatrix} = \begin{bmatrix} T_{11} & \cdots & T_{1,k} \\ T_{21} & \cdots & T_{2,k} \\ \vdots & \vdots & \vdots \\ T_{N1} & \cdots & T_{N,k} \end{bmatrix} \begin{bmatrix} W_{11} & \cdots & W_{1,12} \\ W_{21} & \cdots & W_{2,12} \\ \vdots & \vdots & \vdots \\ W_{k1} & \cdots & W_{k,12} \end{bmatrix} \tag{2.57}$$

Calibration process

The process of shim-coil calibration comprises finding the calibration matrix $\mathbf{W}$. This is done by varying the current input to one coil at the time and then find the best fit of theoretical SH to the produced shim field for each input. If the field produced by the shim coil is totally pure and orthogonal, the only change to the weighting of the different theoretical SH will be to the self-term. When this is not the case, there will be changes to the weighing factors of other SH functions. If the changes to the current given to a coil, and the changes in "current" (weighting factor) given to one of the theoretical SH functions, has a linear relationship, this will be registered in the calibration matrix. For some current to coil X, the magnetic field in all N voxels is given in the $\mathbf{b_0}$ vector. The theoretical B_0 field $\mathbf{b_0^{SH}}$ generated by k pure SH functions is given by

$$\mathbf{b_0^{SH}} = \mathbf{Tw} \tag{2.58}$$

were $\mathbf{w}$ is the set of weighting factors for each SH such that $\left\|\mathbf{b_0} - \mathbf{b_0^{SH}}\right\|$ is as small as possible. In full matrix form, equation (2.58) is

$$\begin{bmatrix} B_1 \\ B_2 \\ \vdots \\ B_N \end{bmatrix}^{\mathbf{SH}} = \begin{bmatrix} T_{11} & \cdots & T_{1,k} \\ T_{21} & \cdots & T_{2,k} \\ \vdots & \vdots & \vdots \\ T_{N1} & \cdots & T_{N,k} \end{bmatrix} \begin{bmatrix} w_1 \\ w_2 \\ \vdots \\ w_k \end{bmatrix} \tag{2.59}$$

where w_i is the weighting factor of the pure SH function in column i.

Repeating the experiment for M different currents will result in M sets of weighting factors $\mathbf{w}^{(1)}, \cdots, \mathbf{w}^{(M)}$. The weighting factors $w_i^{(1)}, \cdots w_i^{(M)}$ for the pure SH in column i of $\mathbf{T}$ can be plotted as a function of the current input to coil X. To see if there is a linear relationship between the field produced by coil X and the field of the pure SH function in column i, a linear fitting can be done to this plot. If the fit is good, the the matrix element $W_{i,X}$ in the calibration matrix is set equal to the the slope of the linear fit, 0 otherwise (see figure 2.10). When linear fittings are done for all k SH functions, the column $\mathbf{W}_X$ in the calibration matrix represents the weighting factors of the pure

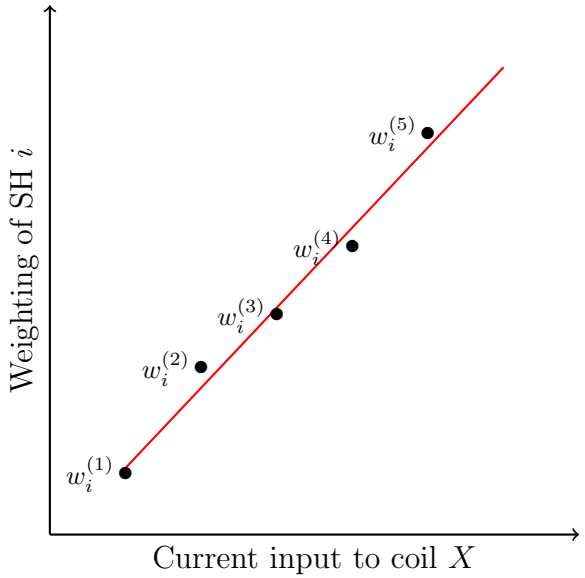

Figure 2.10: Plot of weighting of SH-function i as a function of 5 current inputs to coil X. The red line represents the linear regression to the plotted points. When the linear fit is good, the calibration matrix element $W_{i,X}$ is set to equal the slope of the red line.

SH functions that closest represent the field produced by shim coil X:

$$\mathbf{W}_X = \begin{bmatrix} W_{1,X} \\ W_{2,X} \\ \vdots \\ W_{k,X} \end{bmatrix} \tag{2.60}$$

This is the the calibration of coil X. By repeating the steps above for all available coils, the whole calibration matrix can be completed.

2.4 Shim method comparison

Quantitative susceptibility mapping

Quantitative susceptibility mapping (QSM) is a MRI technique for quantifying and mapping the underlying magnetic susceptibility of tissue. The method enables long term monitoring of diseases across subjects and reduce the chance of observer bias [17]. QSM is based on collected data from a 3D GRE-sequence, similar to the one used for B_0-mapping. Describing how QSM works is beyond the scope of this thesis, but the mentioned QSM 3D GRE sequence can be availed for making a B_0-map to compare the ΔB_0-distribution in brain images after running different shim methods.

2.4.1 Statistical test

The test described below is an example of a statistical hypothesis tests for comparing the median of two datasets. In this particular case, the datasets were the ΔB_0-values inside the brain of a volunteer after applying two different shim methods. In a two-tailed test, the medians between the two datasets are tested for inequality, while in a one-tailed test, the medians are tested for being significantly bigger or smaller than the other one.

Wilcoxon rank-sum test

Is a non-parametric test, meaning no knowledge of the underlying distribution of the datasets is needed. The median of the datasets are tested by comparing their rank-sum; the sum of ranks after listing the observations in both datasets in ascending order and assigning them a rank of 1, 2, etc. If dataset 1 has n_1 observations, and dataset 2 has n_2 observations, the highest value across both datasets are assigned the rank $n_1 + n_2$. Sample sizes does not have to be equal, but needs to be independent.

To check whether the median of dataset 1 is significantly smaller than the median of dataset 2, ($\tilde{\mu}_1 < \tilde{\mu}_2$), the value

$$u_1 = w_1 - \frac{n_1(n_1 + 1)}{2}$$

has to be less or equal to a tabled critical value defined by the set significance level α. Here, w_1 is the sum of the ranks for dataset 1. In a similar manner, $\tilde{\mu}_2 < \tilde{\mu}_1$ can be checked for. For a more detailed description of the Wilcoxon rank-sum test and related table values, see [18].

3 Methods

This chapter describes the development of the B_0-map sequence, the optimization of TR with respect to eddy currents, the shim codes, completion of the shim coil calibration, and how three different shim methods were compared. All experiments were conducted at the 7 T Magnetom Terra scanner at NTNU, Trondheim with two different coils; A 32 channel receive head coil with 1 circularly polarized transmit channel (Nova medical, Wilmington, MA, USA) and a tune up coil (1 channel birdcage coil).

3.1 B_0-mapping

3.1.1 Sequence development

There already exists sequences for making field maps on the Terra scanner, but they might contain effects leading to errors in the map, or have less freedom for e.g. choosing gradient timing and amplitudes. We wanted to have better understanding and control of the sequence design, and therefore developed the B_0-mapping sequence ourselves.

The example sequence

We started out with an example sequence included for the scanner. This sequence was based on a GRE sequence with one echo time. The sequence was slab selective and used a sinc pulse for excitation. A section of the sequence diagram for the example sequence is provided in figure F.1 with TE = 3.9 ms and TR = 10 ms. Phase encoding was done in the x- and y-direction, while z was the readout direction within each slab. The phase encoding governed by the G_y-gradient was implemented with a lower gradient amplitude and rise time than the G_x-gradient. This left the y-gradient on for a longer time period. The dephasing gradient in the read direction also had a lower amplitude and rise time than the G_x-gradient. The same was the case for the readout spoiler. The ramp times for the readout was specifically set to 600ms.

Implementation of second echo

The example sequence was extended from a single echo to a dual-echo. This was done by letting every odd numbered excitation fill the first k-space with echo time TE_1, and every even numbered excitation fill the second k-space with echo time TE_2. A simple sequence diagram of the arrangement is shown in figure 3.1. The reason for choosing

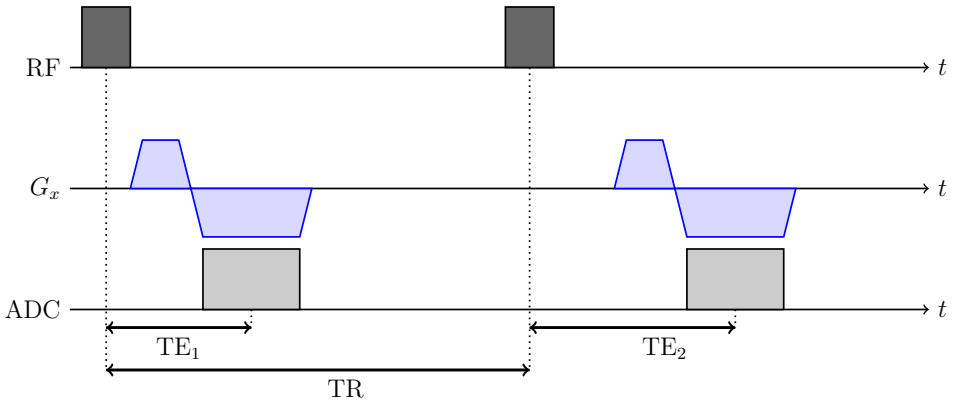

Figure 3.1: Dual-echo with a separate RF excitation for each echo.

an alternating filling of the two k-spaces instead of filling them one at the time, was to increase the chance that the same line in k-space was suffering from the same motion artifact. If the same lines are filled consecutively, they are more likely to be affected by the same motion. When the phase difference is taken between the images of the two echoes, the phase difference would be related to ΔB_0 rather than the difference in the motion artifact. The alternating filling method was therefore chosen.

Amplitudes and rise times

By increasing the gradient amplitudes and decreasing their ramp up time, according to equation (2.37), k-space can be filled in less time. This gives shorter scan times and reduce the chance of the image acquisition being affected by movement artifacts during in-vivo shimming. The maximum gradient amplitude and minimum rise time are limited by the scanners hardware and are given in the sequence code as parameters. These parameters can be scaled down in the user-controllable interface on the scanner console. When a new gradient pulse is added to the sequence, the limits for its maximum magnitude and minimum rise time are set and then it is prepared. The preparing process can be chosen to make the gradient pulse based on a specified duration, ramp up and ramp down times, amplitude or it can be prepared to be as short in time as possible. For all gradients their limits for maximum magnitude and minimum rise time were set to 80% of the maximum gradient moment and 120% of the minimum rise-time set in the scanner console. This was to be conservative on hardware usage. Then all of them, except the readout, was prepared to be as short as possible. For the readout gradient pulse, the amplitude is defined by the FOV, resolution and bandwidth. This change toward more rapid gradient changes is associated with increased eddy current contribution to the image[15]. A strategic placement of the gradients can minimize this contribution.

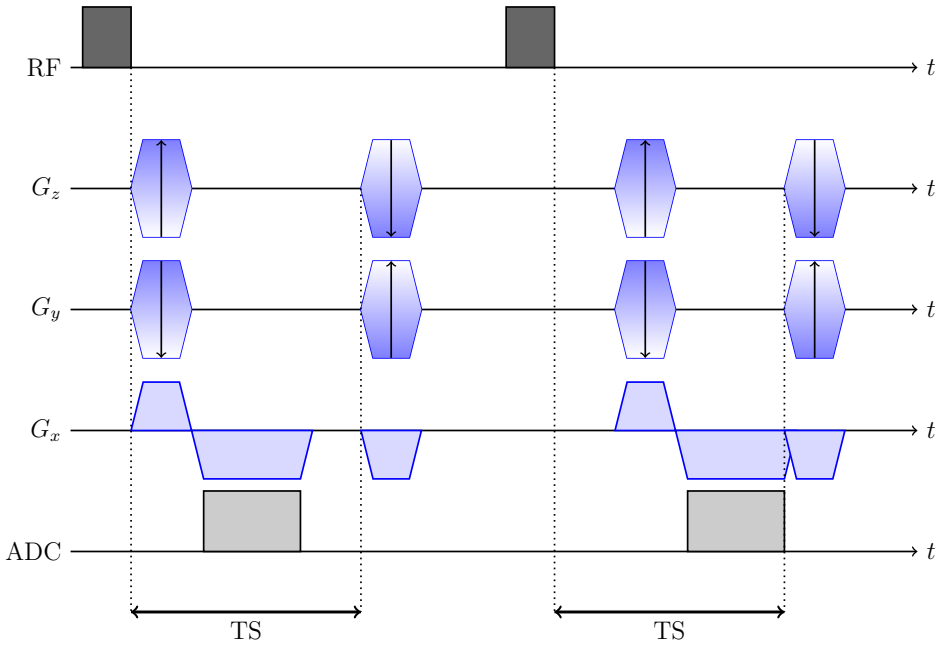

Figure 3.2: The phase encoding-, readout dephaser and readout gradients for both echos, all happens within the time intervall of TS. TS is the time between the second RF pulse and the end of the second sampling.

Gradient timing

With two echo times, the readout gradient will move between the dephasing gradient and the spoiler gradients. To make the two acquired images as similar as possible, the dephasing gradient for both echos was set to appear immediately before the readout. The same was applied for the two phase encoding lobes. This was to give the same effect of eddy currents to both readouts. When the phase difference is taken for the B_0-map, the effect from equal eddy currents will be removed.

The spoiler gradients for both echos was set to start at the same time interval, TS, after the RF. TS was equal the time between the second RF-excitation to the second sampling and is shown in figure 3.2. Placing the spoilers like this would give the same eddy current disturbance to the consecutive RF. It is possible to adjust the timing to give the same contribution of eddy currents to the consecutive readout instead, but it is not possible to do both simultaneously. The RF was chosen since it happens first and eddy currents decay with time according to equation (2.44). A section of the sequence after the first adjustments is displayed in figure F.2.

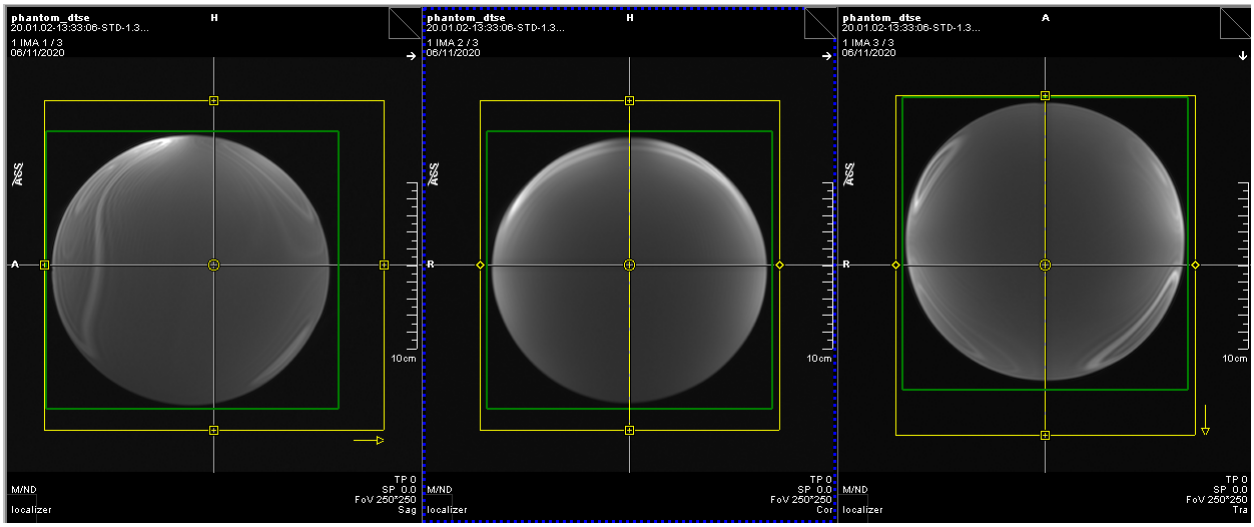

Figure 3.3: The alignment of the phantom volume inside the FOV; the yellow square. The green square is the shim volume used by the scanner.

3.1.2 MRI acquisition

Protocol

For all experiments conducted with our sequence, the flip angle was set to 8°, resolution to 3×3×3 mm^3, the image size to 60×66×68 (LR×HF×AP), ΔTE to 1.98 ms and the bandwidth/pixel was set to 1430 Hz/px. The readout was set to be in the feet-head direction, since oversampling would reduce the chance of getting wrap-around artifacts from signal occurring outside the FOV in in-vivo scans. The value of TE_1, TE_2 and TR was varied among experiments.

Phantom used for in-vitro scans

The phantom used for all in-vito scans was a spherical oil phantom with a diameter of 16 cm. It had a single resonance and no internal structures. The spatial alignment of the phantom inside the image "cuboid" is shown in figure 3.3.

3.1.3 Image processing and analysis

From the B_0-map, the off-resonances inside the phantom volume was collected. To exclude all contributions from voxels outside of the phantom volume, a magnitude map from the MR acquisition was used for threshold masking. The threshold was set such that the binary mask corresponded closely with the phantom volume. In addition, a binary erosion algorithm was applied to shrink the mask by two pixels in the radial direction to make sure the mask was inside the phantom volume. An example of image slice and mask is shown in figure 3.4. Both the B_0- and magnitude map was obtained

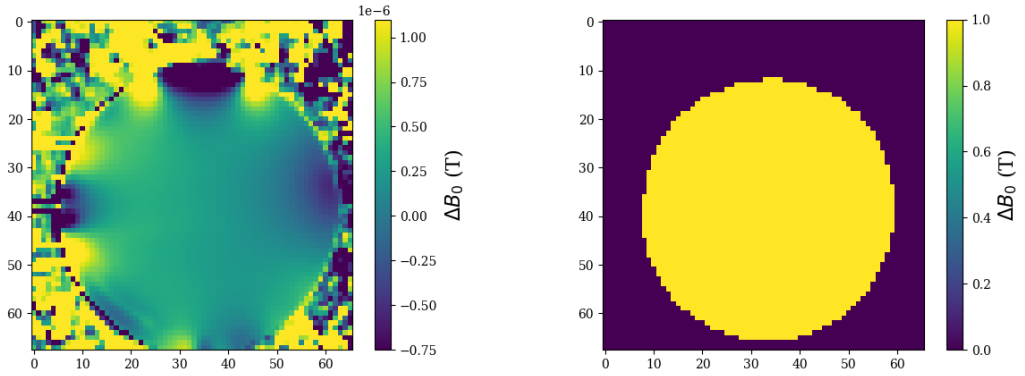

(a) **(b)**

Figure 3.4: A sagittal slice approximately in the middle of the left-right direction and the corresponding mask.

from the shim codes described in section 3.2.1. The mean value and standard deviation of the dataset was calculated and histogram plotted. The number of bins in the histogram was set to be 2% of the number of voxels inside the mask. In addition, a colormap of a sagittal and transverse slice was plotted. The chosen slices were approximately at the center of their respective axes. Calculations were carried out in python.

3.1.4 Difference maps

The contribution from eddy currents can be studied by repeating the ΔB_0-measurement with opposite gradient polarity[16]. The switching in polarity changes the direction of the induced eddy currents. By subtracting the two obtained B_0-maps, the field deviations originating from eddy currents will be doubled, while deviations originating from B_0-inhomogeneities will be removed.

In the experiments containing difference maps, the first B_0-mapping was conducted by setting the phase encoding direction from anterior to posterior (A$\gg$P) on the scanner console, while the second B_0-mapping had its phase encoding set to run from posterior to anterior (P$\gg$A). The two maps are referred to as the B_0^{ap}-map and B_0^{pa}-map respectively. Changing from (A$\gg$P) to (P$\gg$A) also changes the polarity of the readout gradients. All gradient polarity changes between the two B_0-maps are displayed in figure 3.5.

The ΔB_0-values of the the two obtained B_0-maps were subtracted voxel-vise. The B_0^{pa}-map had to be slightly shifted with respect to the B_0^{ap}-map to align them in all three dimensions. Shifted voxels on the edges would follow periodic boundary conditions and

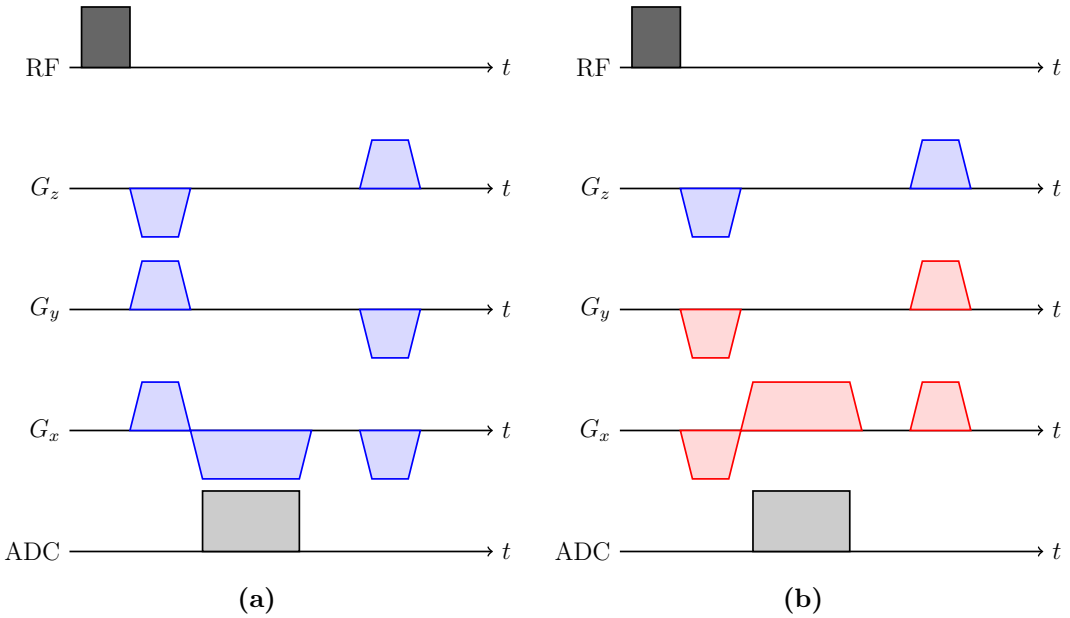

Figure 3.5: Change of gradient polarity. (a): Sequence diagram for the B_0^{ap}-map. (b): Sequence diagram for the B_0^{pa}-map.

reappear on the opposite side of the image. Sagittal, coronal and transverse slices were compared between the two maps to find the shift that gave the best alignment. The resultant image would contain the difference, ΔB^{diff}, between the B_0^{ap}- and B_0^{pa}-map:

$$\Delta B^{diff} = \Delta B_0^{ap} - \Delta B_0^{pa}$$

and was analyzed with histogram and colormaps as explained in section 3.1.3. The magnitude data from the B_0^{ap}-map acquisition were used for masking. A mask made from the magnitude data from the B_0^{pa}-map acquisition would give the same mask, only deviating with a few voxels.

3.1.5 B_0-map validation

To check whether the field map acquired by our sequence gave reasonable results or not, it was compared to a B_0-map acquired by a field map sequence provided by the vendor. Both the 32 channel coil and the tune up coil was used for comparison. In addition to this, a FID signal was sampled to compare the full with at half maximum (FWHM) of the resonance peak and the histogram from the off-resonances inside the mask. For both experiments, TE_1=2.12 ms and TE_2= 4.10 ms for our sequence.

Field-map from Siemens

The field-map sequence from Siemens used ΔTE= 1.02 ms, flip angle of 72° and bandwidth of 260 Hz/px. The resolution and image size was set to match with our sequence.

Histograms and slices were compared. For our own sequence, TR was set to 20 ms. The shim settings were the same for both sequences.

FWHM of histogram and FID

As an extra validation of the ΔB_0-map, the FWHM between the histogram obtained from the field-map from this scan was compared to the FWHM of the FID of the sample. Since the phantom only consists of a single resonance, only one peak will be apparent in the NMR spectra. The FID measurement was done with 0.35 ms rectangular pulse, TE = 0.50 ms, flip angle of 90°, 2 averages and the bandwidth was set to 4000 Hz. TR was set to 40 ms for our own B_0-map sequence, and the 32 channel coil was used.

3.1.6 TR experiments

Increasing TR gives the eddy currents longer time to decay, but will also increase the overall scan time. Studying the eddy current contribution in the resultant ΔB_0-map for different TR's can give deeper insight when evaluating the compromise between eddy currents and scan time. For each TR, the sequence was run twice with opposite gradient polarity such that a ΔB^{diff}-map could be formed. A histogram of the eddy map inside the threshold mask was plotted in addition to colormaps of a sagittal and transverse slice. To get an overview of the eddy current contribution for different TR's, the mean value of the ΔB^{diff}-map inside the threshold mask, $\langle \Delta B^{diff} \rangle$, was plotted as a function of TR.

Four experiments were conducted for different TR values. The changes done to the sequence design, experimental setup and protocol is listed below.

1. 32 channel coil. TR = {7, 10, 15, 20, 25, 30, 35, 40} ms. Sinc pulse. TE_1 =2.12 ms, TE_2 = 4.10 ms. The gradient mode on the scanner console was set to "Fast".

   For the next three experiments, the following changes were done in the sequence code: Changed sinc pulse to rectangular pulse. Limit for maximum magnitude was increased from 80% to 85% of the maximum gradient moment. All gradient max amplitudes and minimum gradient rise times were in addition multiplied with a scaling factor that could be adjusted on the scanner console. These two factors were 0.78 for the gradient max amplitude and 1.55 for the rise times. In addition to this, the gradient mode was switched from "Fast" to "Whisper". A separate scaling was also done to the minimum rise times of all gradients in the read direction. This scaling factor is stated below for the specific experiment. The gradient max amplitude of the read spoiler was set to equal the gradient max amplitude of readout gradient.

2. 32 channel coil. TR = {7, 10, 15, 20, 25, 30, 35, 40} ms. Rise time of all gradients in the read direction was multiplied with a factor 2.39. TE_1 =2.00 ms, TE_2 = 3.98

ms. Part of the sequence diagram is shown in figure F.3.

3. 32 channel coil. TR = {7.6, 10, 15, 20, 25, 30} ms. Rise time of all gradients in the read direction was multiplied with a factor 4.23. TE_1 =3.00 ms, TE_2 =4.98 ms. Sequence diagram is shown in figure F.4.

4. Tune up coil. TR = {7.6, 10, 12, 15, 17, 20} ms. Rise time of all gradients in the read direction was multiplied with a factor 4.23. TE_1 =3.00 ms, TE_2 = 4.98 ms.

3.2 Shim procedure and calibration

3.2.1 Shim codes

To calculate the B_0-map and shim currents, MATLAB codes written by M. Poole, D. Brenners and D. Tse was availed. The raw data is fourier transformed to get the magnitude maps and the B_0-map. When optimizing the shim currents with respect to a certain volume, the user can specify the mask containing this volume. The SH-functions for unit current were calculated inside the mask (matrix $\mathbf{T}$) and multiplied with the calibration matrix $\mathbf{W}$ to form the shim field matrix $\mathbf{A}$. To find the shim currents $\mathbf{I}$ that minimized $\|\mathbf{b_0} - \mathbf{AI}\|$, the Moore-Penrose pseudoinverse[19] of $\mathbf{A}$ is used. From the information about the shim currents applied during the B_0-mapping, $\mathbf{I_{old}}$, the new current $\mathbf{I_{new}}$ was calculated. The output of the code is the ΔB_0 before shimming and the predicted value after shimming ΔB_0^{shim}, the three current vectors, $\mathbf{T}$ and $\mathbf{b_0}$. In addition, the B_0-map and histogram of the ΔB_0-values inside the mask could be plotted before and after shimming. A schematic overview of the code is shown in figure 3.6.

3.2.2 Calibration of the shim coils

For the shim coil calibration, all experiments were done on the same oil phantom, coil and protocol used in TR-experiment 4. TR was set to 10 ms. The reason for using the tune up coil for calibration is because the 32 channel coil stores more data than necessary for the calibration process and is also slightly lifted from isocenter. In addition, there was an artifact in the phantom when using the 32 channel coil. The artifact can be seen in figure 3.3.

The shim field produced by each coil was varied by adjusting the shim current between 7 different settings. The middle data point represented the current giving the best shimmed field by the scanner. A field map had to be acquired for the 7 shim settings for all shim coils, meaning the B_0-mapping sequence had to be run 84 times in total. When all 84 field maps were acquired, the data was analyzed coil-wise to find the calibration matrix elements.

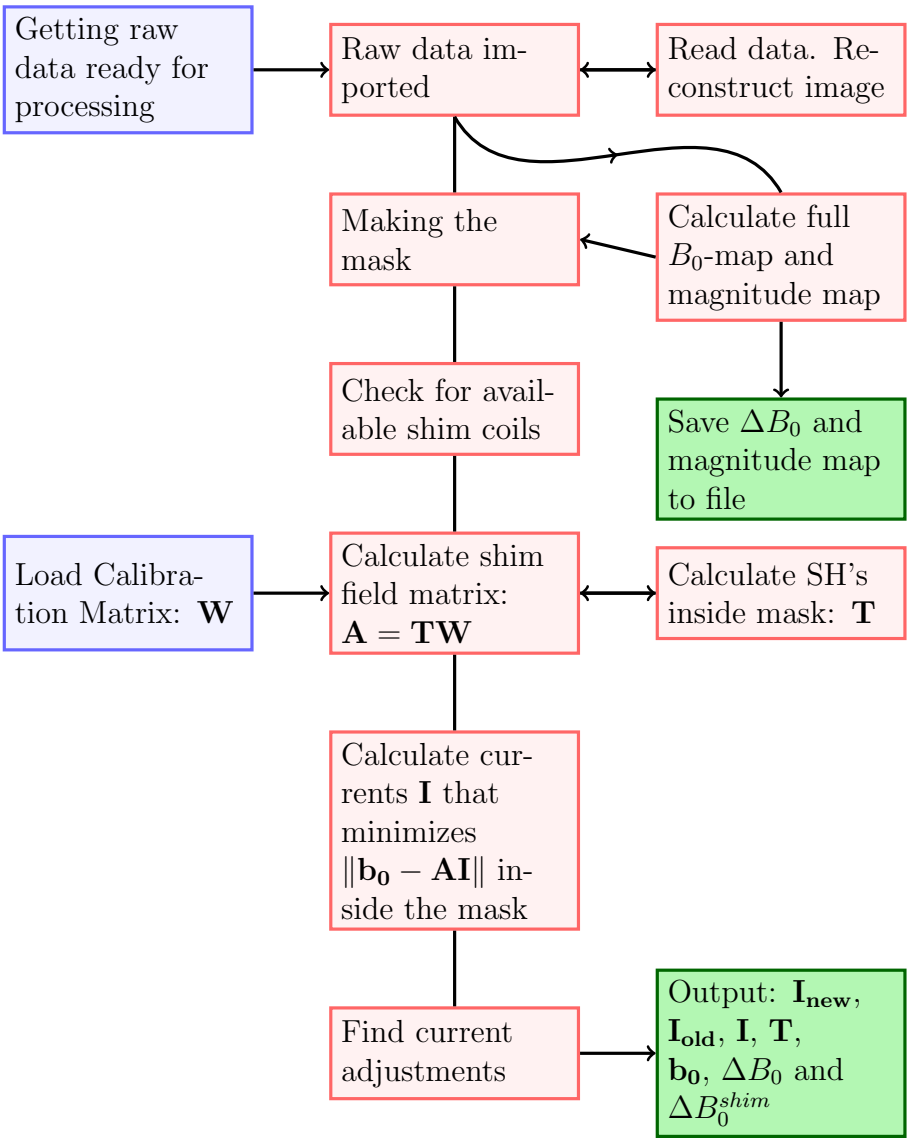

Figure 3.6: Flow chart of the shim codes used for image processing of the raw data and optimization of shim currents. Blue and green colored boxes represents input and output respectively.

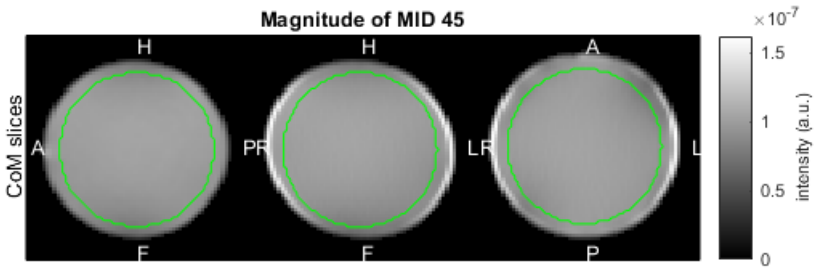

Figure 3.7: The masking of the phantom.

The same mask was applied to all 7 field-maps and included voxels to approximately 1 cm from the edge of the phantom. The mask is shown in figure 3.7. The weighting factors $\mathbf{w}$ of the SH functions were calculated to minimize $\|\mathbf{b_0} - \mathbf{Tw}\|$ inside the mask. The calculations were done using the Moore-Penrose pseudoinverse[19] of $\mathbf{T}$. Theoretical SH functions up to 4th order were used, meaning 25 SH functions were represented in matrix $\mathbf{T}$.

When the weighting factors $\mathbf{w^{(1)}}$, ..., $\mathbf{w^{(7)}}$ for coil X were calculated, the elements $w_i^{(1)}, \cdots w_i^{(7)}$ were iterated through. $w_i^{(1)}, \cdots w_i^{(7)}$ are the different weighing factors for the pure SH in column i of $\mathbf{T}$ at different current settings to coil X. These 7 weighting factors were plotted as a function of the current input, and linear regression was done to this plot. The *coefficient of determination*, R^2, was used to determine if the linear fit was good or poor. If the linear fit had $R^2 > 0.9$ the calibration term $W_{i,X}$ was set to match the slope of the linear fit. Zero otherwise. Two of the linear fits for coil Z^2 is displayed in figure 3.8.

Calibration code

All raw data from the same coil were iterated through. For each iteration, the code in section 3.2.1 was applied to get the coil current and the B_0-map and SH-functions inside the mask. This was repeated 7 times until the weighting factors $\mathbf{w^{(1)}}$, ..., $\mathbf{w^{(7)}}$ for the M measurements were calculated. Then, the 25 elements in the $\mathbf{w}$'s were iterated through and a linear regression was done to $w_i^{(1)}$, ..., $w_i^{(7)}$ as a function of the coil current input $\forall i \in [1, 25]$. The calculated R^2 value from the regression was in the end used to determine if the calibration matrix element was set to equal the slope of the linear regression line or to zero. A schematic description of the codes is carried out in figure 3.9. The calculations were done in MATLAB.

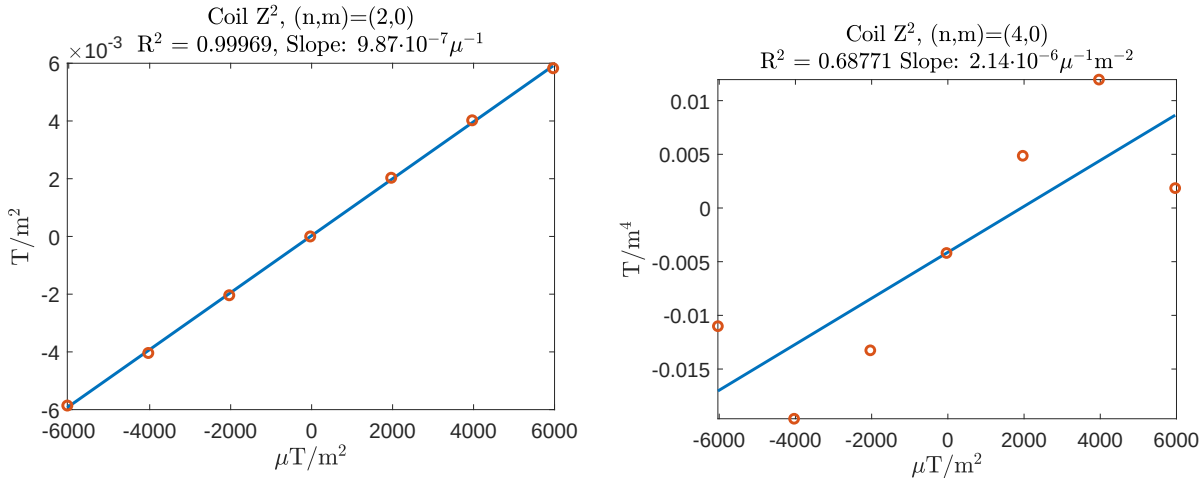

(a) Self-term **(b)** Cross-term

Figure 3.8: Two of the linear fittings for the Z^2 coil. The red points are the weighting of the pure spherical harmonic function of order n and degree m, plotted as a function of the current input to coil Z^2. The blue line is the linear fit to these values. Figure (a) displays the self term of Z^2 and has a high R^2 value. The slope of the line in figure (b) is not used in the calibration matrix due to R^2 being less than 0.9.

3.2.3 Test of calibration matrix

The calibration matrix was tested on one of the data files for the calibration experiment to see if it could successfully reset the value of the coil to the one of the pre-shim.

3.3 Shim method comparison

B_0-maps of the head of 37 volunteers was measured using a QSM-sequence with two similar protocols. We will refer to them as the "tra"- and "sag" - protocol. The main differences between the two protocols were the slab orientation and the size of the FOV. In advance of the measurements, one of the following shim methods was applied: the newly developed shim, the default shimming method provided by the scanner or an iterative shim. The iterative shimming involved running the standard shim several times until the field looked sufficiently good. The radiographer handling the scanner for the particular scan decided the number of iterations. In total, 19 of the volunteers were shimmed with the new shim, 19 with the standard shim and 7 with the iterative shim. This gave a total of 45 B_0-maps, meaning some of the volunteers were scanned with different methods to provide several within-subject comparison. From the 45 B_0-maps, histograms, mean value, standard deviation and FWHM of ΔB_0 inside the brain mask was provided for analysis. QSM field maps, brain masks and statistics were all measured

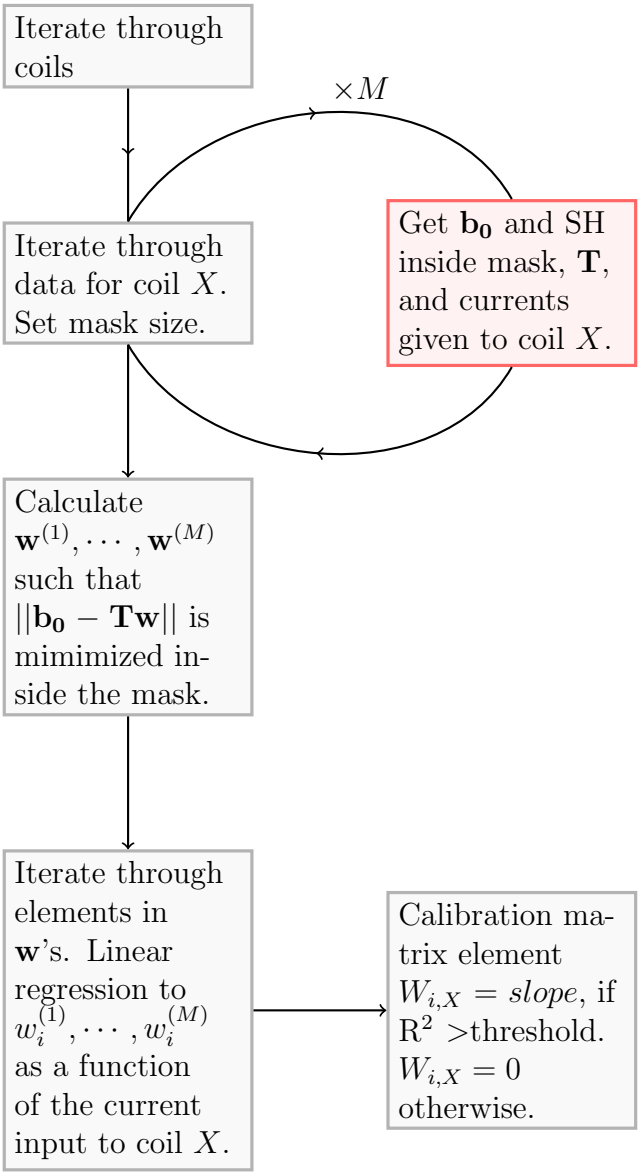

Figure 3.9: Schematic overview of the workflow for calculating the calibration matrix element $W_{i,X}$ for coil X at M different shim settings. The red square represents the shim codes.

and calculated at St. Olavs hospital. Informed consent was obtained from all volunteers.

3.3.1 Statistical analysis

To investigate which shim that gave the best result, the Wilcoxon rank-sum test was applied on the FWHM and the standard deviation (sdd) of the different ΔB_0 inside the brain mask. A bad shim would give a wider B_0-distribution and hence give a bigger FWHM and sdd. Since the test assumes independent samples, volunteers appearing in both of the tested datasets would be removed from the largest one. In addition, if a volunteer was tested twice with the same shim method, but with different QSM protocols, one of the sessions were removed, since the small change in protocol was assumed to have a minor influence on the measured B_0-map. The kept session was the one that would give the highest chance of keeping the null-hypothesis. Our null- and alternative hypothesis for the test were as follows:

- H_0: $\tilde{\mu}_1 = \tilde{\mu}_2$
- H_1: $\tilde{\mu}_1 < \tilde{\mu}_2$

with $\tilde{\mu}$ being the median of the dataset. The significance level α was set to 0.05 for both tests. Since the alternative hypotheses H_1 suggest a higher value for the median, both of the tests were one-tailed. The calculations done for the statistical analysis were done in Microsoft Excel and IBM SPSS Statistics 27.

Comparing with the same QSM protocol

In case the applied QSM-protocol affected the quality of the obtained B_0-map after shimming, an additional test was done between the new shim and the standard shim. The majority of the B_0-maps obtained after the standard shim was applied were made by the sag protocol, while the majority of B_0-maps obtained after the new shim were made by the tra-protocol. To make sure there was no bias in the choice of protocol, an extra test was carried out to only compare sessions where the same protocol was used.

4 Results

In this section, the results from the B_0-map validation and TR-optimization are presented. The calculated calibration matrix and the predicted shim on one of the extreme current settings from the shim calibration is shown, and also a test of the whole shim process. At the end, the shim comparison and statistical analysis is presented.

Image directions

In the images presented in this chapter, the patient directions are shown with arrows labeled with left (L), right (R), head (H), foot (F), anterior (A) or posterior (P).

4.1 B_0-mapping

4.1.1 Validation of field map

Field maps from both sequences

The four B_0-maps of the spherical oil phantom obtained with the newly developed sequence (new) and Siemens' field map sequence (Siemens) are all displayed in figure 4.1. Each row is a different experiment, while each column represent a different slice. Slices on the left are sagittal, while the ones on the right are transverse. Field maps obtained with the 32 channel coil is marked with 32ch, while field maps obtained with the tune up coil is marked with TU. The ΔB_0-distribution for all four field maps inside the phantom volume is given in figure 4.2.

FWHM of histogram and resonance peak

A graphical comparison between the resonance peak from the FID and the histogram of the ΔB_0 distribution inside the phantom obtained with the new sequence with TR=40 ms is shown in figure 4.3. The FWHM for the FID and the field map histogram was found to be 7.0 Hz and 6.6 Hz respectively.

4.1.2 TR-experiment

An overview of the results from the TR-experiment is shown in figure 4.4 and 4.5. Figure 4.4 shows the mean value of the difference map $\langle \Delta B^{diff} \rangle$ as a function of the

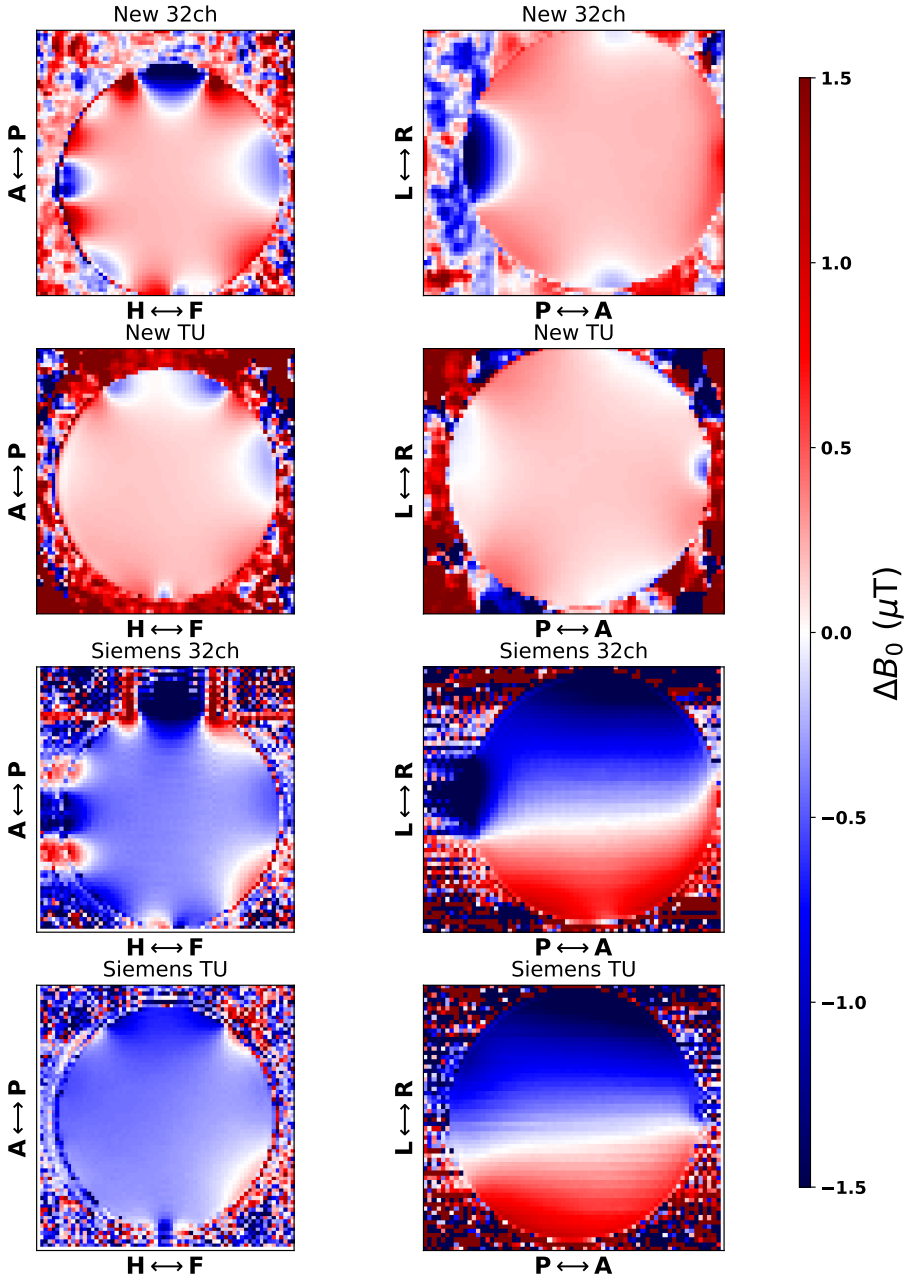

Figure 4.1: Slices of the B_0-map done with both the new sequence and the vendor provided sequence. From top to bottom: New sequence with 32 channel coil (32ch), new sequence with tune up coil (TU), Siemens sequence with 32 channel coil and Siemens sequence with tune up coil. Sagittal slices are displayed on the left, transverse on the right.

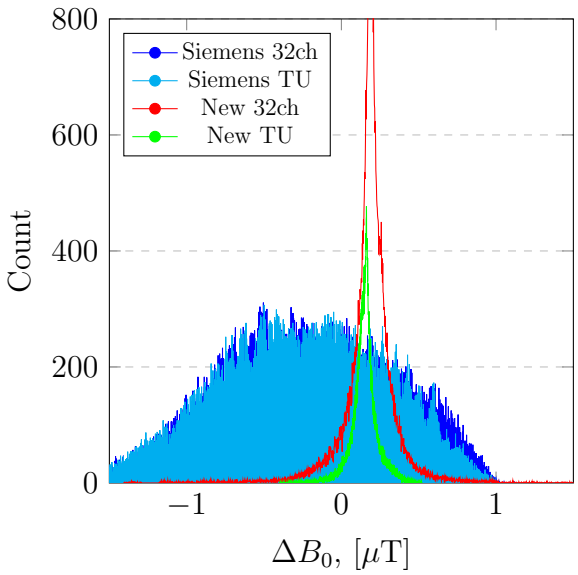

Figure 4.2: Histograms of the ΔB_0-distribution for the two field mappings done with two different coils.

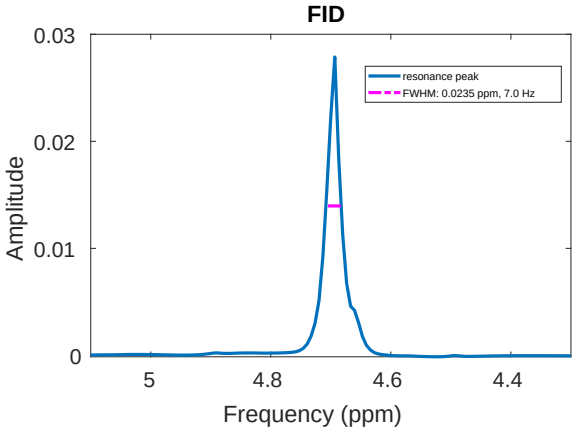

(a) Resonance peak from the free induction decay measured from the phantom. The FWHM is 7.0 Hz.

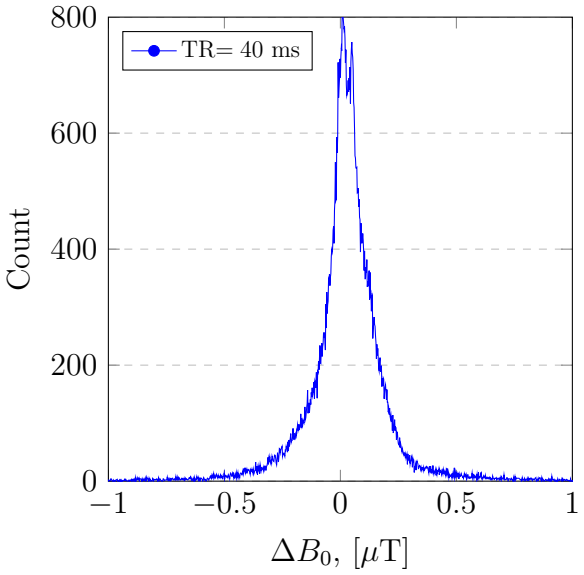

(b) ΔB_0 distribution inside the phantom measured with the new field map sequence with TR=40 ms. The FWHM is found to be 6.6 Hz.

Figure 4.3: A graphical comparison of the resonance peak from the free induction decay (a) and the ΔB_0-distribution (b) inside the spherical phantom.

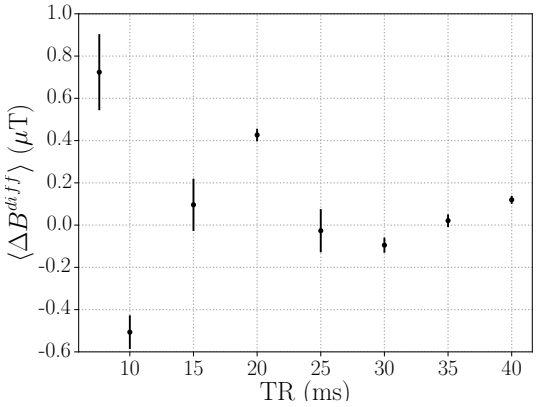

(a) First TR-experiment. 32 Channel coil.

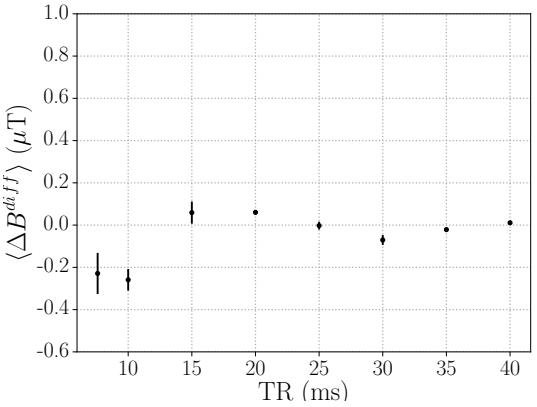

(b) Second TR-experiment. 32 Channel coil.

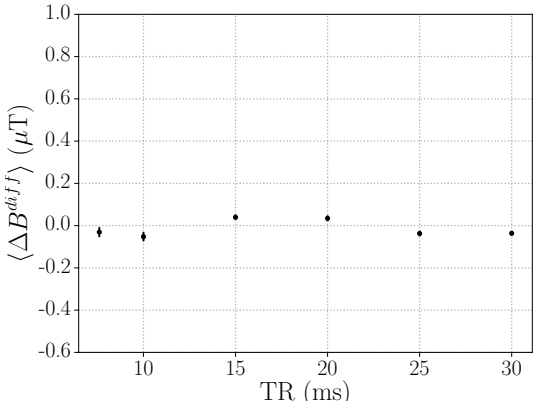

(c) Third TR-experiment. 32 Channel coil.

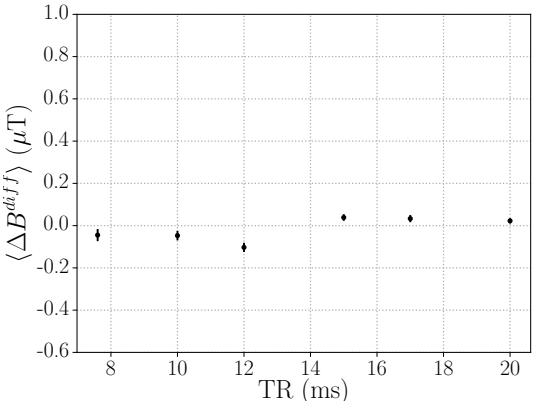

(d) Fourth TR-experiment. Tune up coil.

Figure 4.4: Plots of the mean value $\langle \Delta B^{diff} \rangle$ as a function of the repetition time TR. The bars shows one standard deviation to each side. Both $\langle B^{diff} \rangle$ and the standard deviation was calculated with respect to the ΔB^{diff}-values inside the mask.

repetition time TR for all four experiments. The total length of the bars in the plot is two times the standard deviation of the ΔB^{diff} inside the mask. All numerical values for $\langle \Delta B^{diff} \rangle$, standard deviation and TR's from the four experiments are provided in table H.1. Figure 4.5 shows histograms of ΔB^{diff} inside the phantom-mask for the four experiments. Sagittal and transverse slices from the first TR-experiment are shown in figure 4.6 and 4.7 respectively. The repetition time is displayed above each image in milliseconds. In addition to this, a plot of how the ΔB^{diff}-map changes across the different spatial directions are provided in figure 4.8. Image slices and other plots from the remaining three experiments are provided in appendix H.

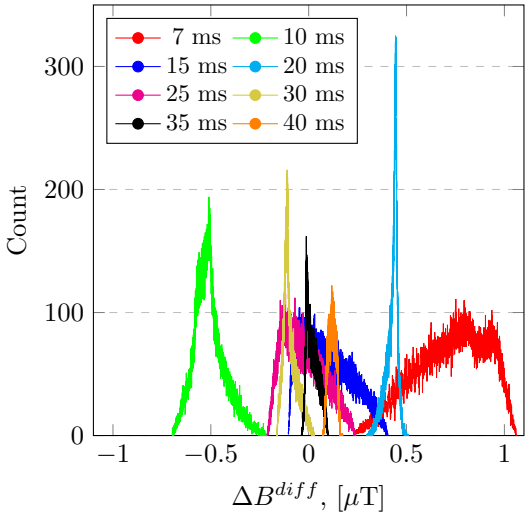

(a) First TR-experiment. 32 Channel coil.

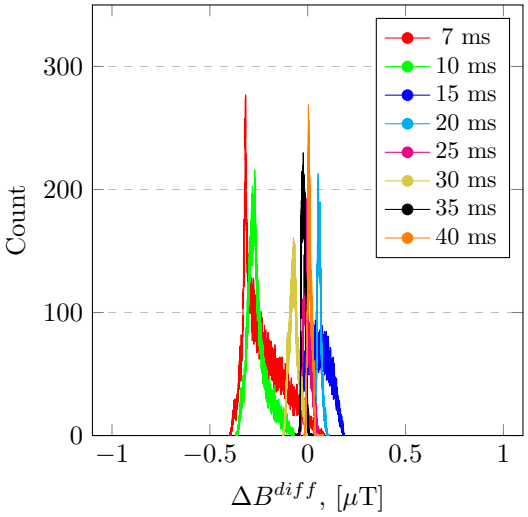

(b) Second TR-experiment. 32 Channel coil.

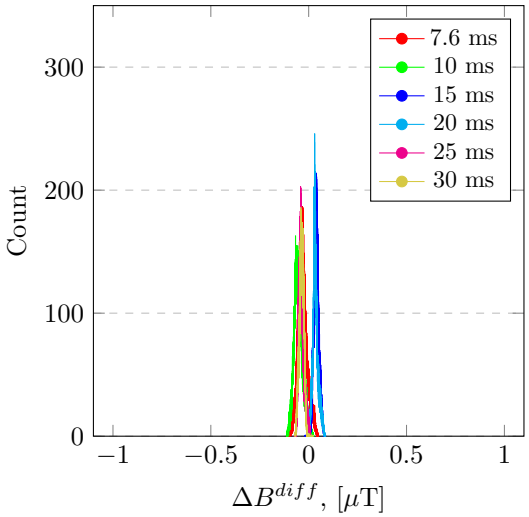

(c) Third TR-experiment. 32 Channel coil.

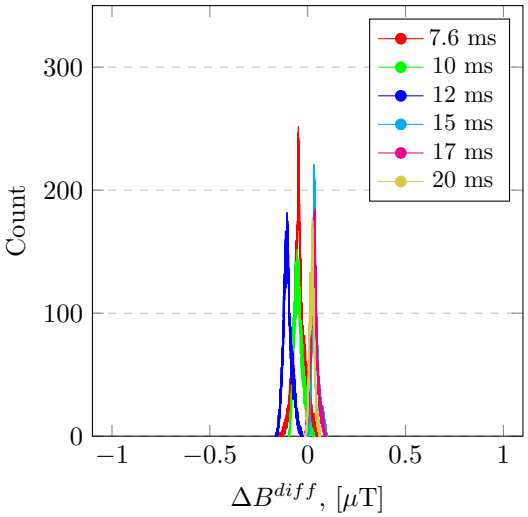

(d) Fourth TR-experiment. Tune up coil.

Figure 4.5: Histogram plots of ΔB^{diff} inside the phantom mask for the four TR-experiments.

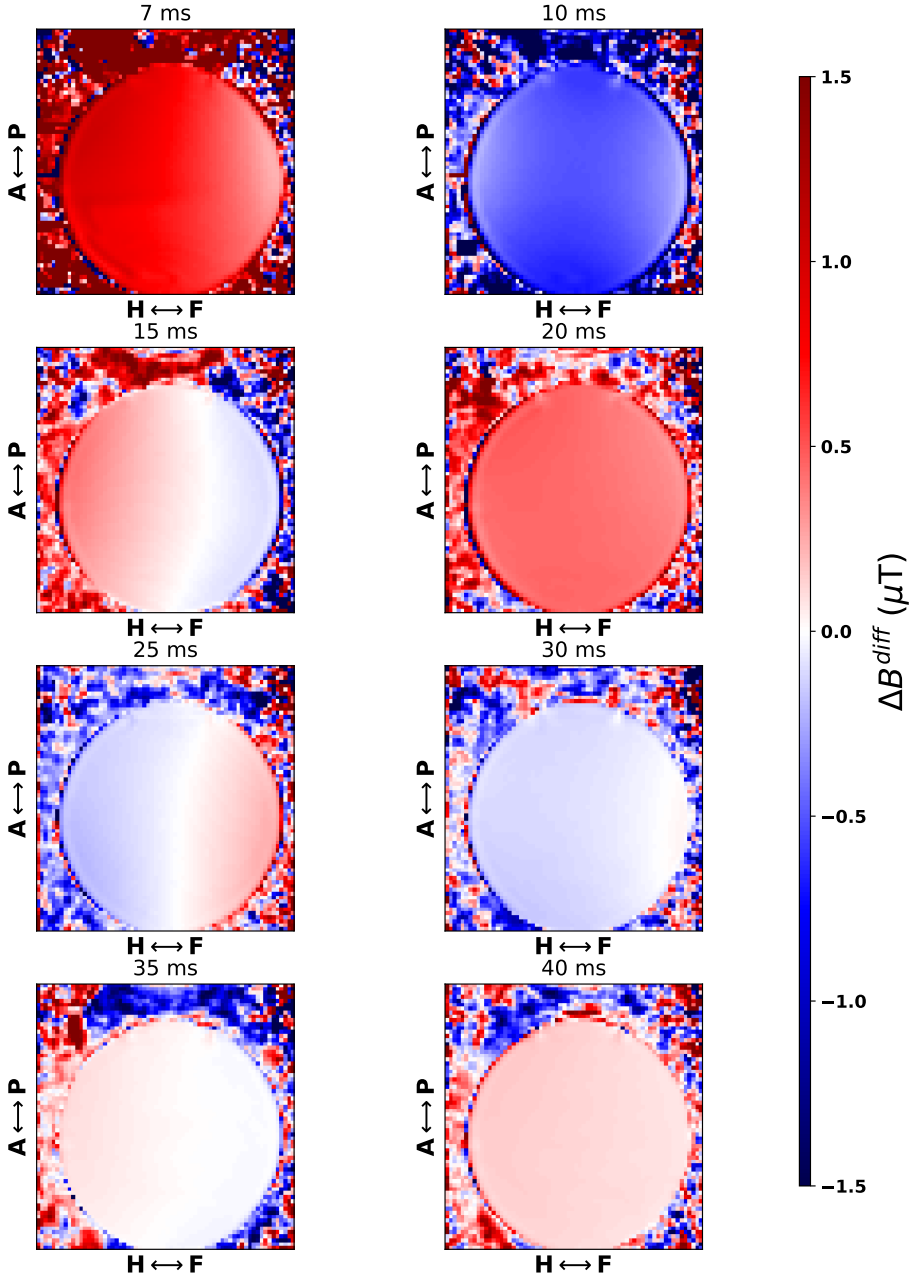

Figure 4.6: Sagittal slices of the difference map ΔB^{diff} from the first TR-experiment. The repetition time for a given slice is displayed above it.

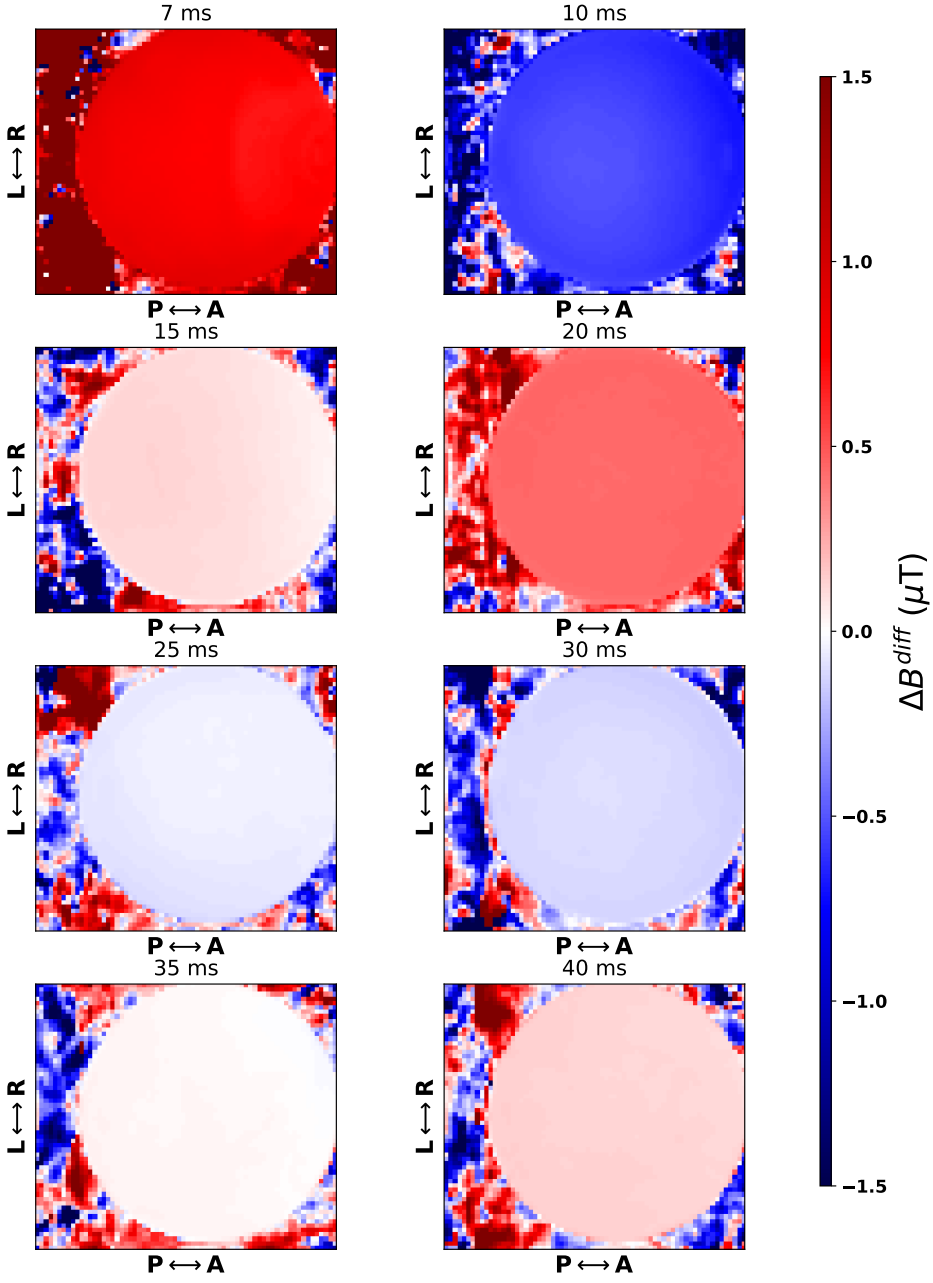

Figure 4.7: Transverse slices of the difference map ΔB^{diff} from the first TR-experiment. The repetition time for a given slice is displayed above it.

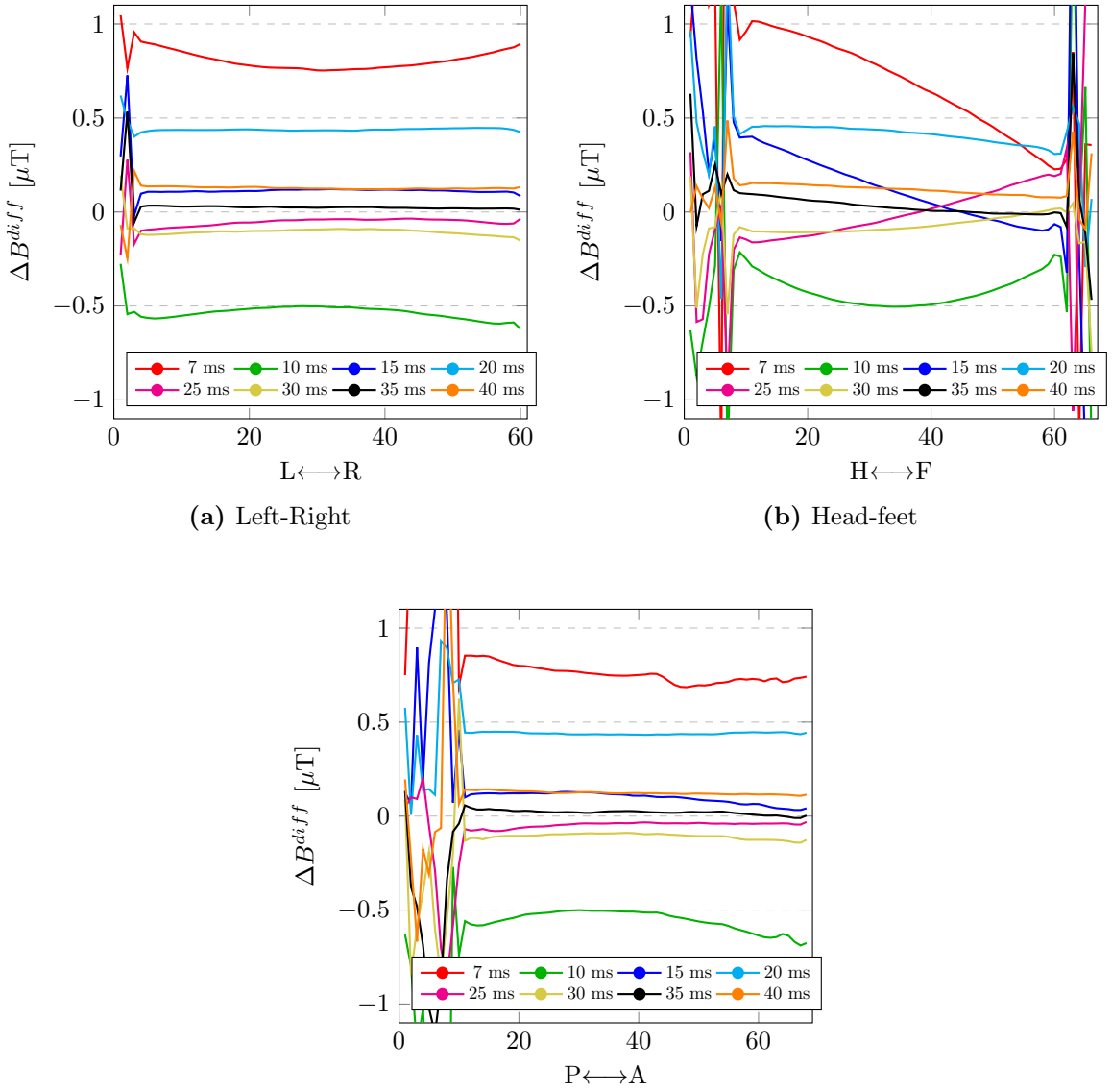

(a) Left-Right

(b) Head-feet

(c) Posterior-anterior

Figure 4.8: Change of ΔB^{diff} across the center of the image for the first TR-experiment.

4.2 Shim coil calibration

The shim coil calibration resulted in the calibration matrix given in figure 4.9b, while the in-house calibration matrix calculated at St. Olavs hospital is shown in figure 4.9a. The numbering on the vertical axis corresponds to the SH-function listed in table E.1, and the numbering on the horizontal axis corresponds to the coil given in table E.2.

Test of calibration matrix

In the data file chosen, the current of the shim coil X had been changed from 4.2 μT/m to -602.0 μT/m for the calibration experiment. Running the shim codes with the new calibration matrix calculated in this project, gave the results in figure 4.10a and 4.10b. The currents in figure 4.10a are listed in three columns. The left column displays $\mathbf{I_{old}}$, the middle column $\mathbf{I}$, and the right column, $\mathbf{I_{new}}$.

Test of shim process

The test of the calibration matrix calculated at St. Olavs Hospital is shown in figure 4.11. Figure 4.11b shows the ΔB_0-distribution before the shim and the distribution predicted after the shim when the currents listed in figure 4.11a are applied to the scanner. The actual field measured after shimming is shown in figure 4.12. This was the shim applied on the volunteer in experiment a_1 for the shim comparison part listed below.

4.3 Shim method comparison

Figure 4.13, 4.14 and 4.15 gives an overview of the high resolution B_0-maps obtained from the QSM-sequence. The maps are displayed as sagittal slices, where figure 4.13 shows the 19 sessions shimmed with the newly developed shim, figure 4.14, 19 sessions with the standard shim, and figure 4.15 the 7 sessions shimmed using the standard shim iteratively. The different sessions are labeled with a_i, b_i and c_i as indicated in the figures. The mean, standard deviation and FWHM of the B_0-data from the different sessions are presented in table I.1, I.2 and I.3. In addition, a histogram showing the ΔB_0 distribution inside the brain mask is shown in figure 4.16 for each session. Distributions from the same shim method is plotted on top of each other.

Same volunteer

A side by side comparison of the standard shim and the new shim is provided in figure 4.17 for session a_1 and c_{19}. B_0-maps obtained after the new shim is displayed on the left side, while the maps obtained after the standard shim is on the right side. The position of the head is indicated with arrows in the images. A similar comparison is shown in

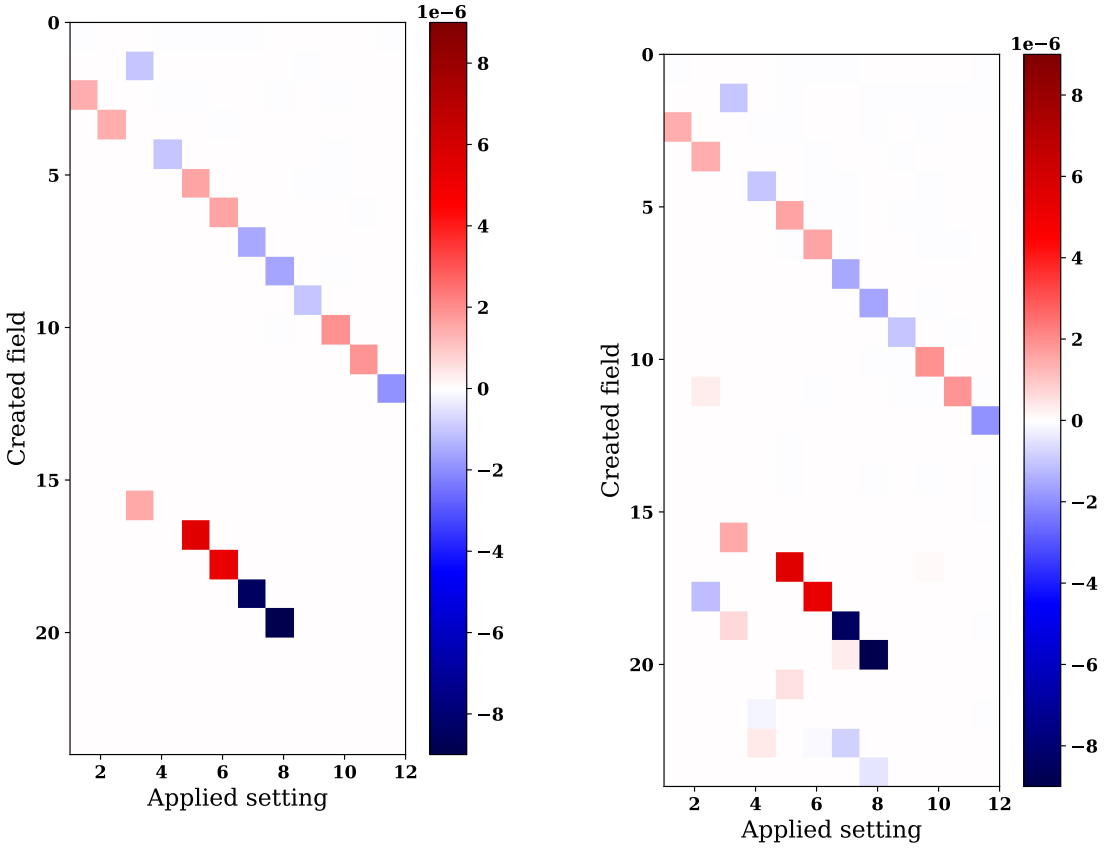

(a) Calibration matrix calculated at St. Olavs Hospital

(b) Matrix calculated in this project.

Figure 4.9: The calibration matrix for 4th order pure spherical harmonics. The vertical axis shows the weighting of each pure spherical harmonic function that most accurately represent the field generated by the coil on the horizontal axis.

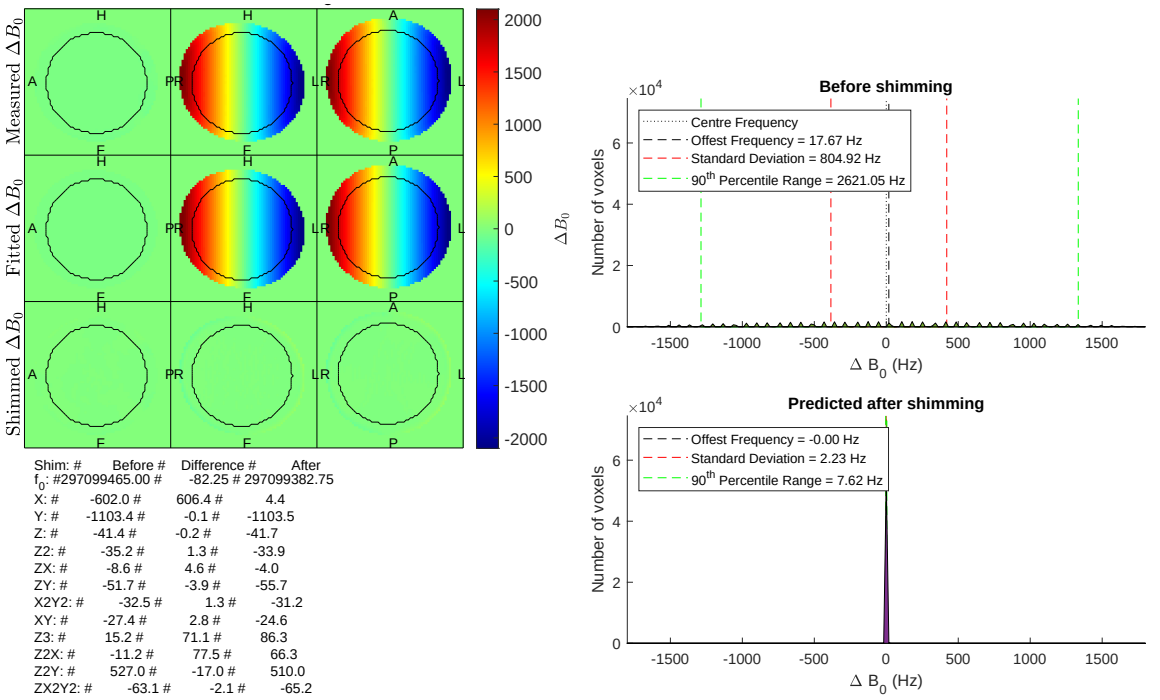

(a) B_0-offsets inside the phantom and currents before and after the shimming with the new calibration matrix.

(b) Histogram of the B_0-offsets measured before and predicted after shimming.

Figure 4.10: The B_0-offsets before and after shimming with the new calibration matrix.

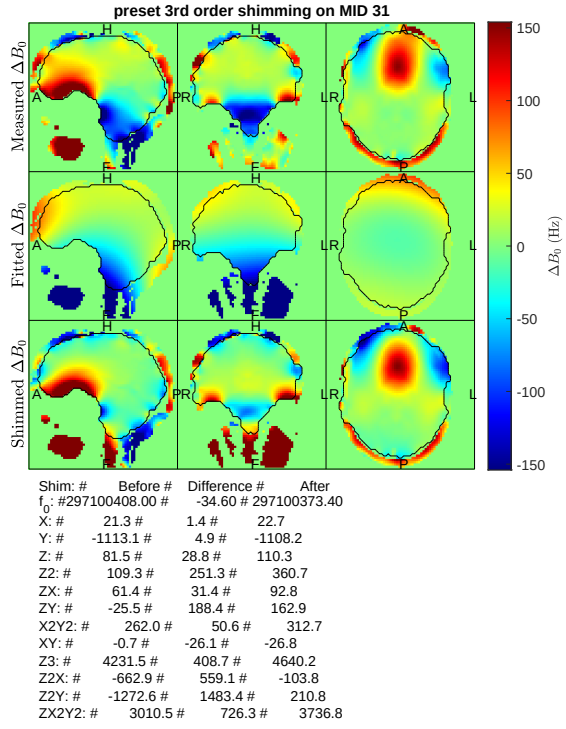

(a) The calculated currents that would optimize the shim.

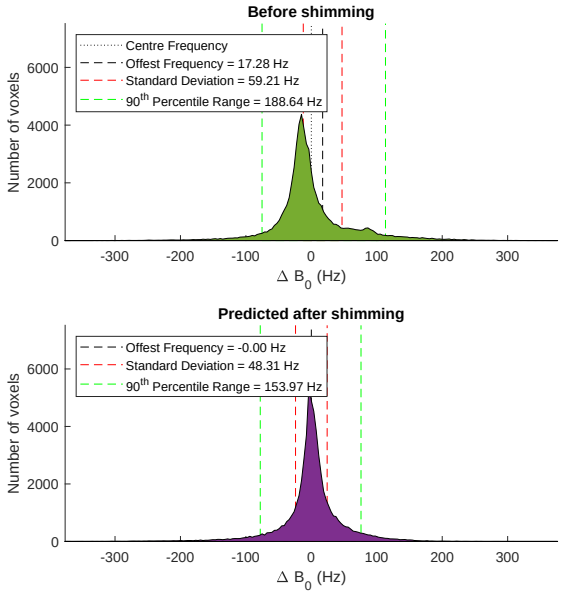

(b) Histogram of the B_0-offsets measured before shimming and predicted after shimming.

Figure 4.11: A test of the calibration matrix calculated at St. Olavs hospital. Figure (a) gives the predicted shim currents and (b) shows the B_0-distribution measured before shimming and predicted after shimming.

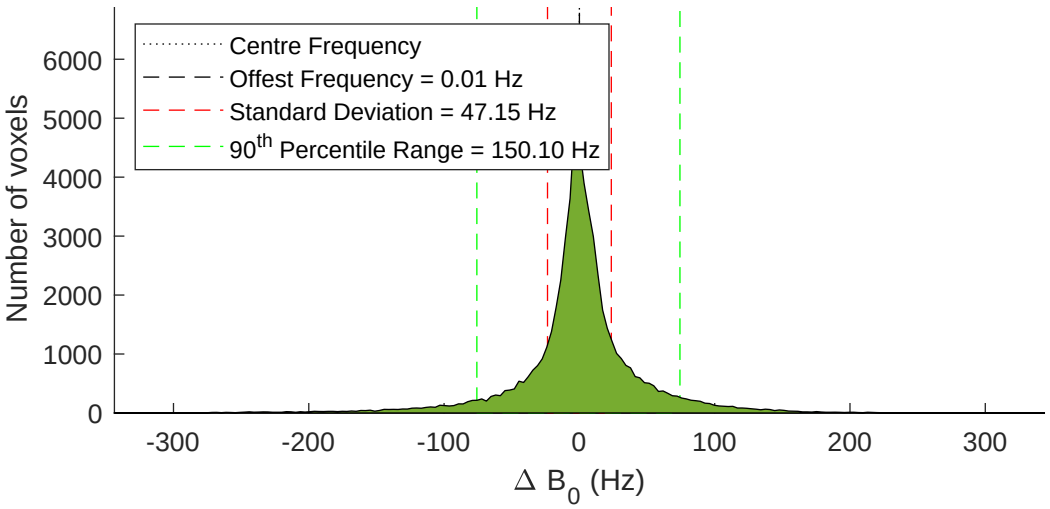

Figure 4.12: The B_0-distribution inside the brain measured after shimming.

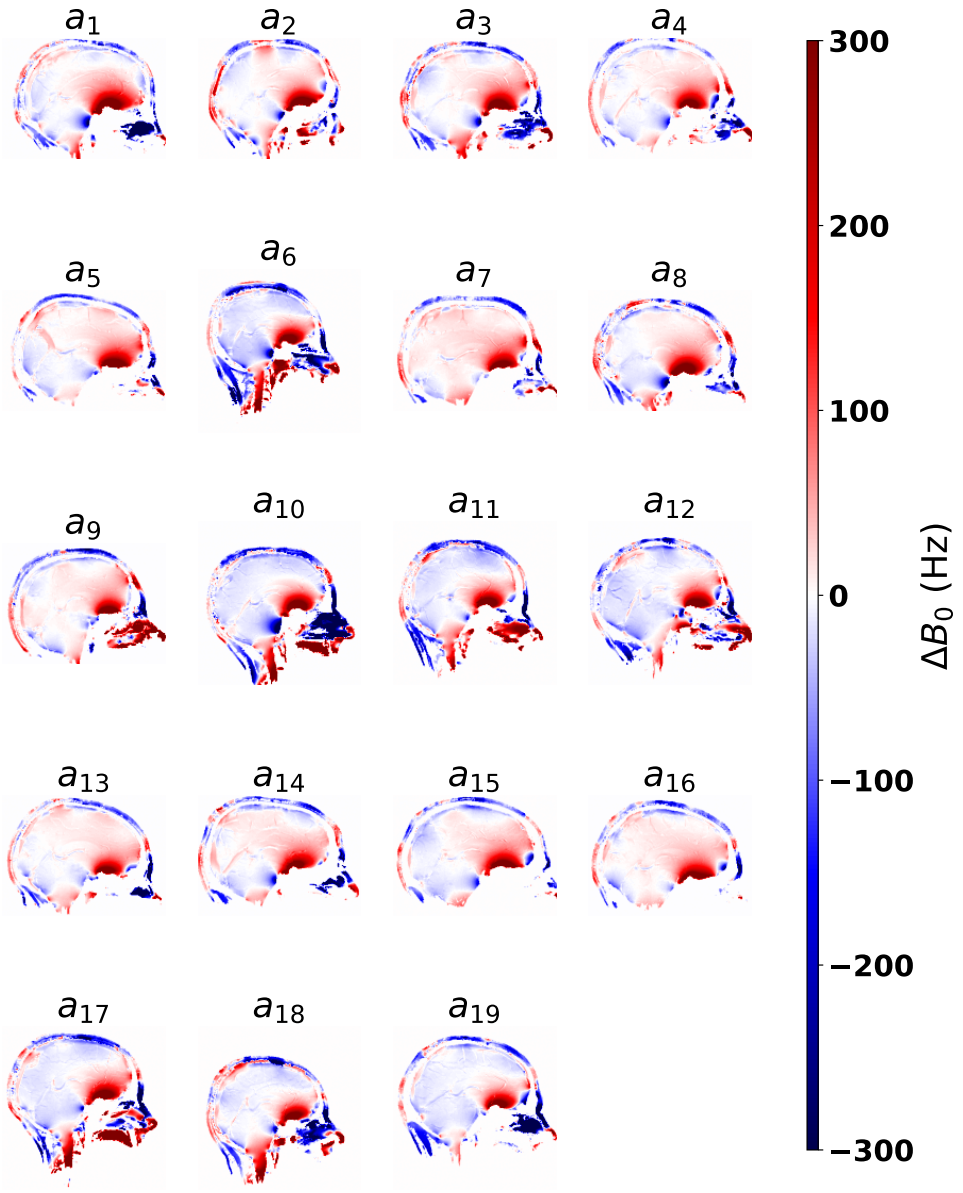

Figure 4.13: All high resolution B_0-maps obtained from the QSM-sequence after applying the newly developed shim.

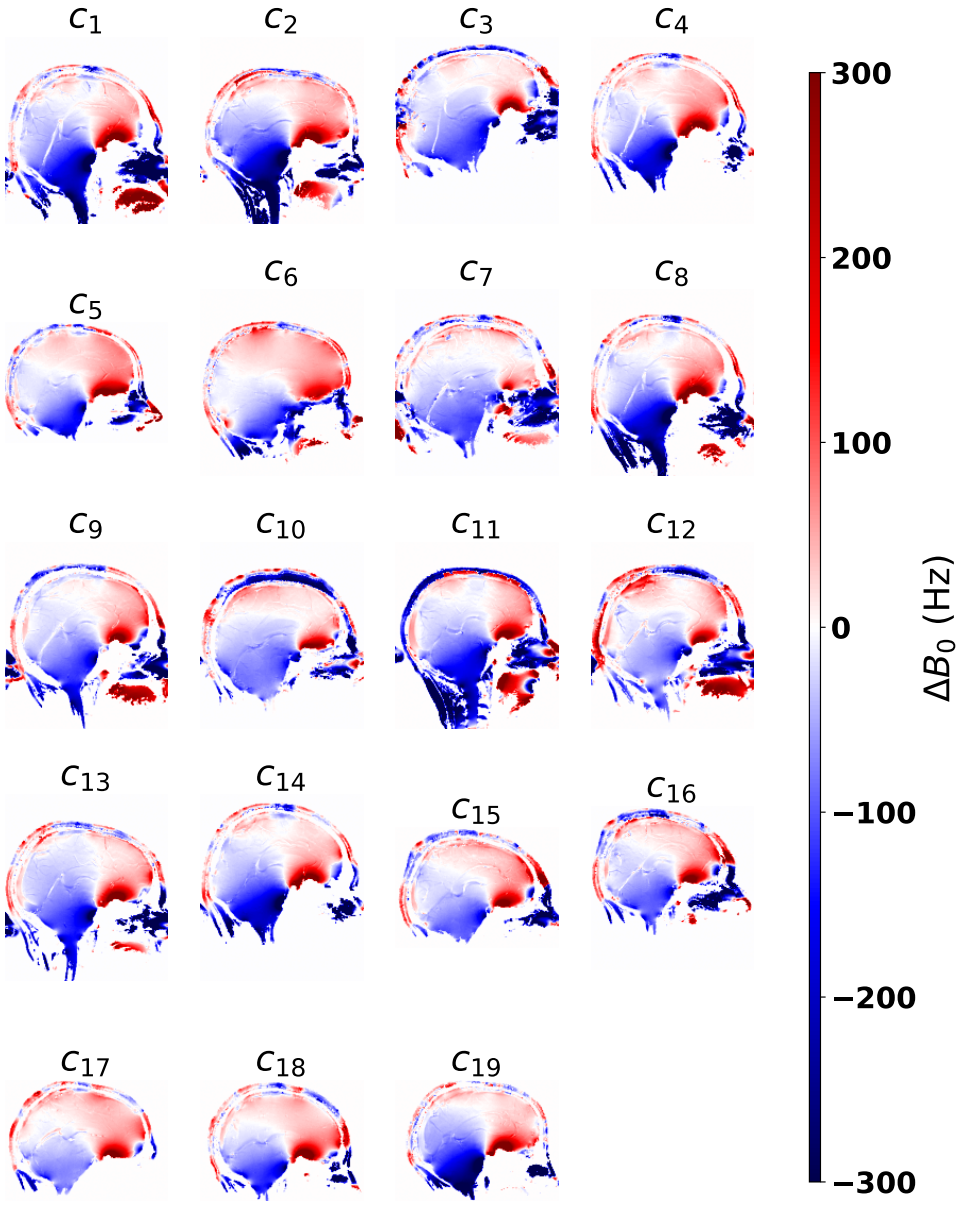

Figure 4.14: All high resolution B_0-maps obtained from the QSM-sequence after applying the standard shim.

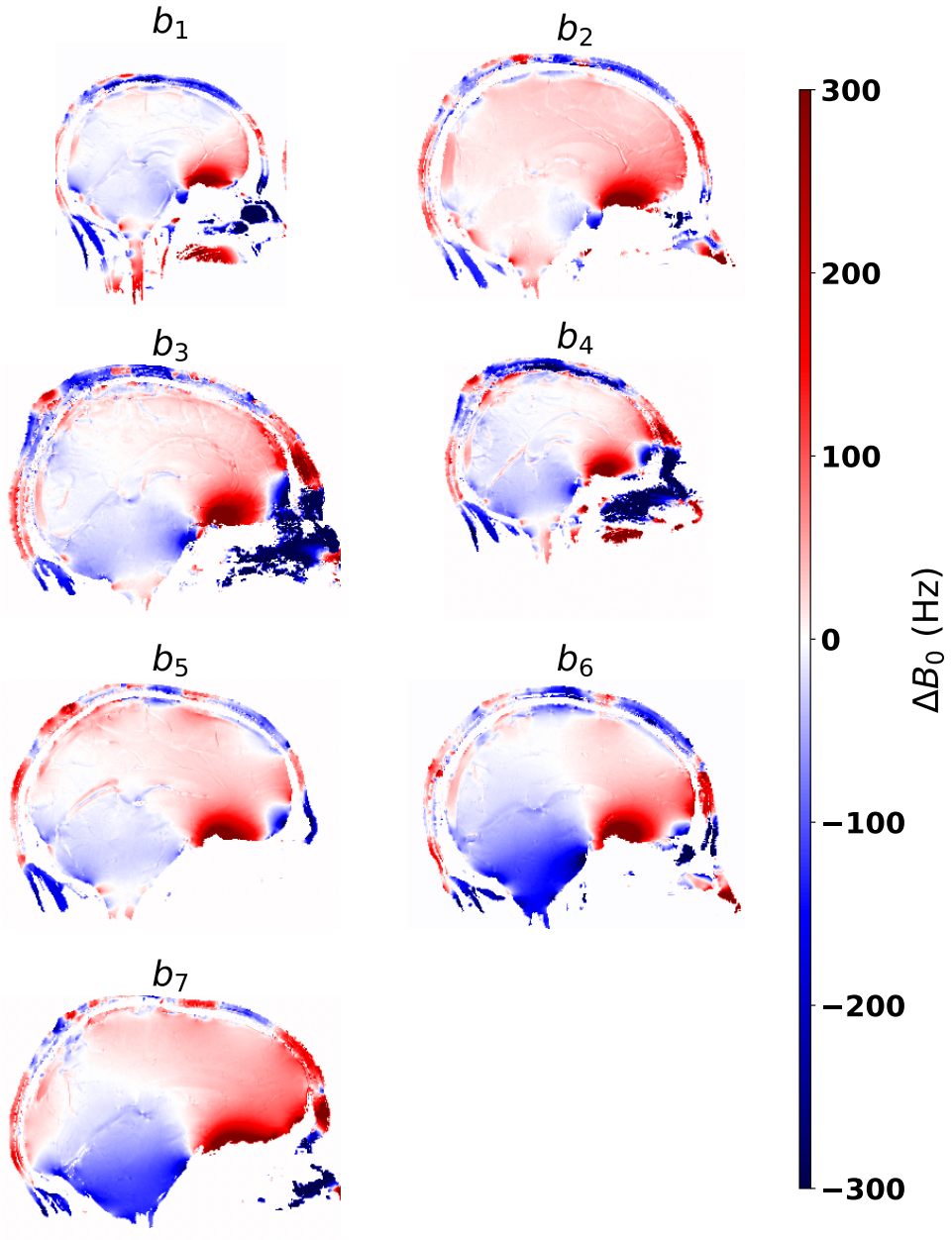

Figure 4.15: All high resolution B_0-maps obtained from the QSM-sequence after applying the standard shim iteratively.

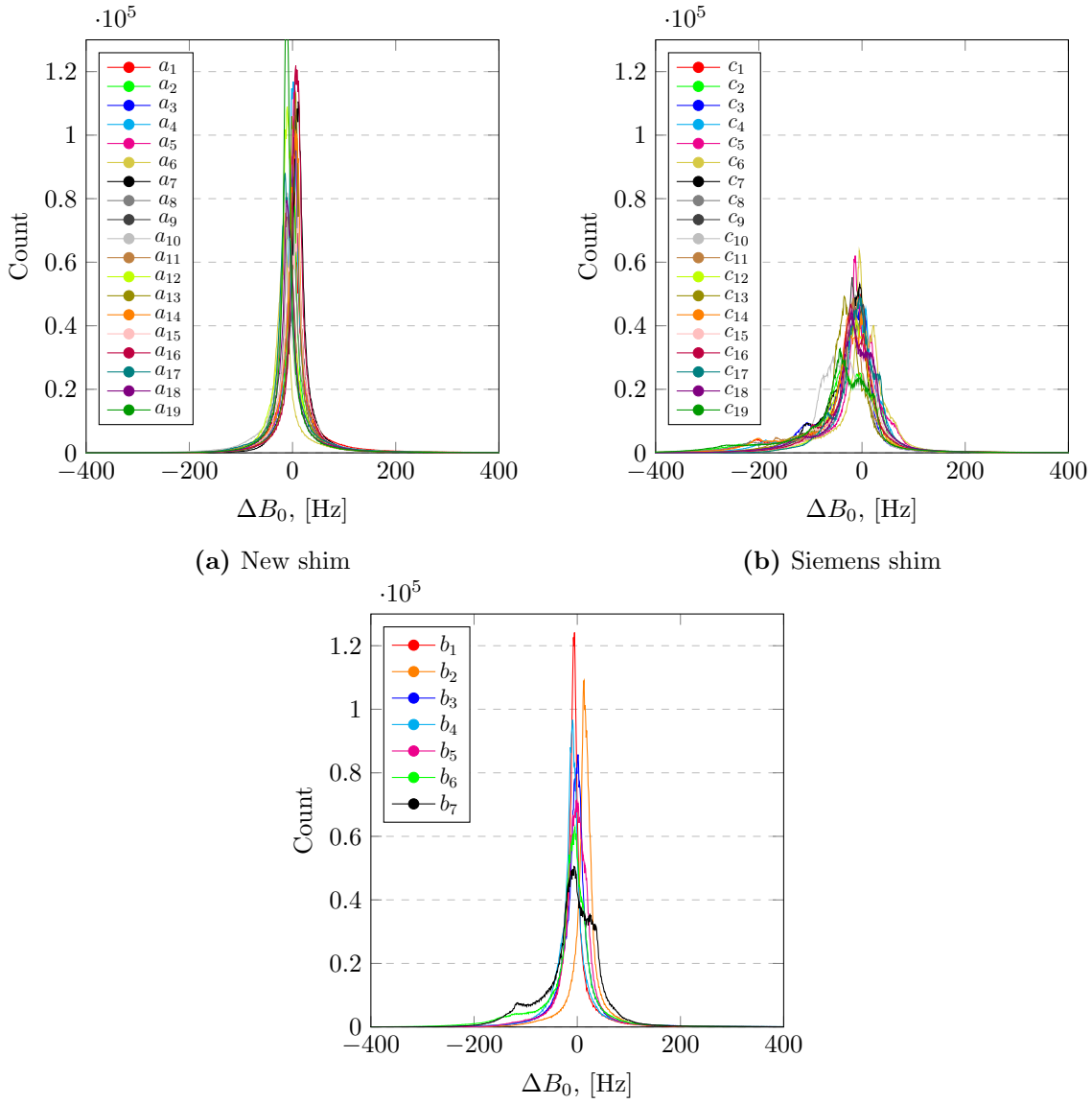

(a) New shim

(b) Siemens shim

(c) Iterative shim

Figure 4.16: Histograms of the ΔB_0 distribution in the QSM-maps after applying different shim methods. The distribution was only counted inside the brain mask.

figure 4.18 for session b_6 and c_{18} between the iterative shim on the left and the standard shim on the right. In both figure 4.17 and 4.18 the side by side comparison is done on the same volunteer. In table I.1, I.2 and I.3, same volunteers are marked with the same symbol ($\star\square\triangle\clubsuit\nabla\diamond$) in front of the numbering (No).

Box plot

In figure 4.19a and 4.19b a box and whisker plot is shown for the FWHM and standard deviation respecively. The standard shim is shown on the right, the new shim method in the middle and the iterative shim on the left. The blue box indicates the interquartile range and the horizontal black line inside the box is the median. The ends of the whiskers are the maximum and minumum values that are still within 1.5 times the interquartile (IQ) away from the 1^{st} and 3^{rd} quartile (Q1 and Q3):

$$\begin{aligned} \textit{Max whisker} &: \text{Highest value within } Q3 + 1.5IQ \\ \textit{Min whisker} &: \text{Lowest value within } Q1 - 1.5IQ \end{aligned}$$

Values outside this range are the outliers marked with a circle. Outliers more than 3IQ away from Q1 and Q3 are categorized as extremes and marked with a star. Figure 4.19a has some outliers and one extreme value that are all marked with a number. The session corresponding to the number (No) can be found in table I.1, I.2 and I.3.

4.3.1 Statistical analysis

The 6 results from the Wilcoxon rank-sum test, are displayed in table 4.1. In this table, the first column indicates the two shim methods compared, while the second column indicates whether the median of the FWHM or the standard deviation is tested. n_1 and n_2 are the sizes of the test groups and w_1 and w_2 are the sum of the ranks. If the u_1 value in the table falls below u-critical, the null hypothesis is rejected. The following sessions were removed from the analysis to maintain unpaired samples:

- New/Siemens: a_1, c_6 and c_{16}
- New/iterative: b_2 and b_3
- iterative/Siemens: b_1, b_4, c_6, c_{15}, c_{16}, c_{17} and c_{18}

The additional tests, only comparing sessions with the same QSM protocol, are listed in table 4.2.

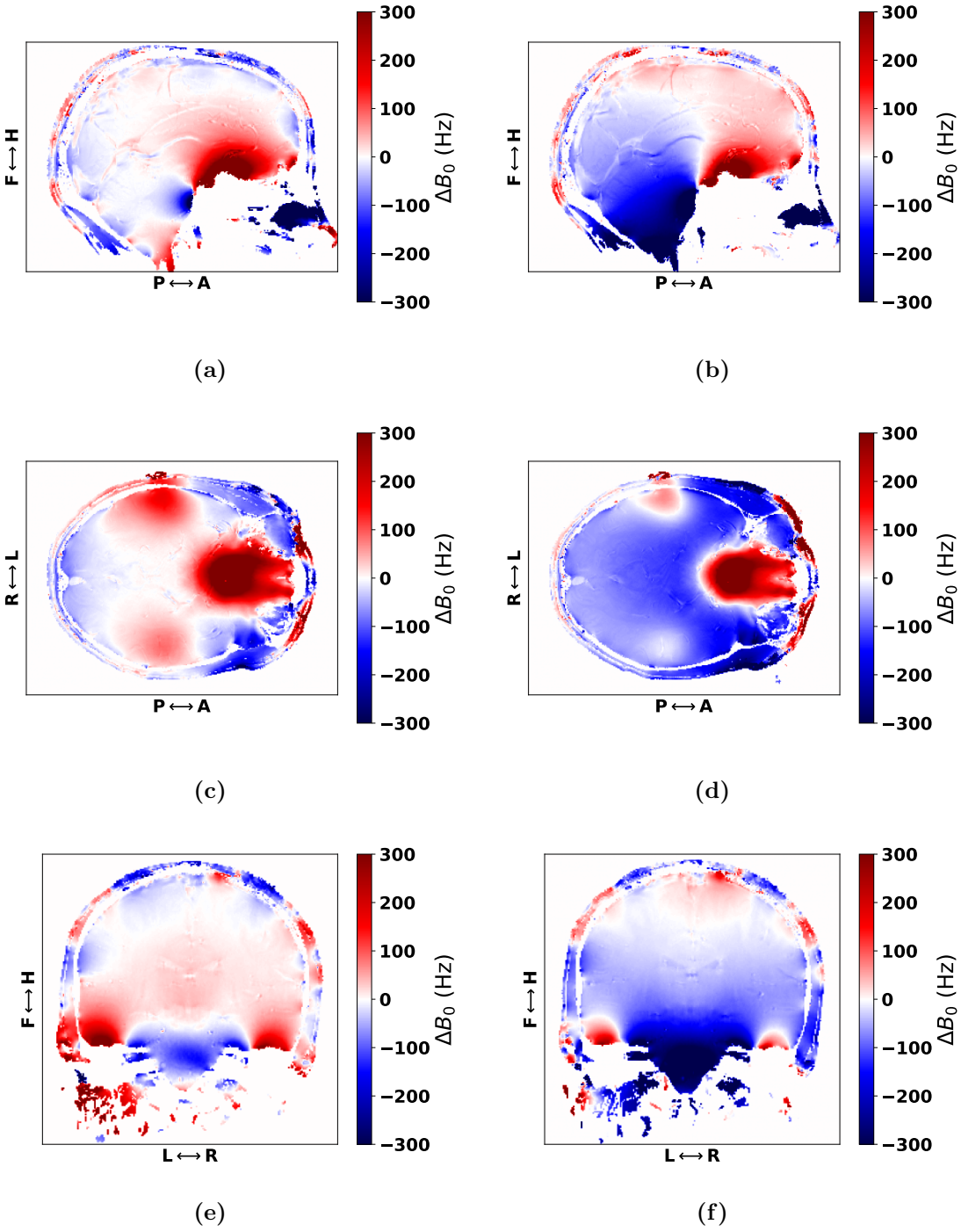

Figure 4.17: Side by side comparison of the obtained B_0-maps after applying the new shim (a,c,e) and the standard shim (b,d,f) on the same volunteer. This is from session a_{19} and c_{19} respectively.

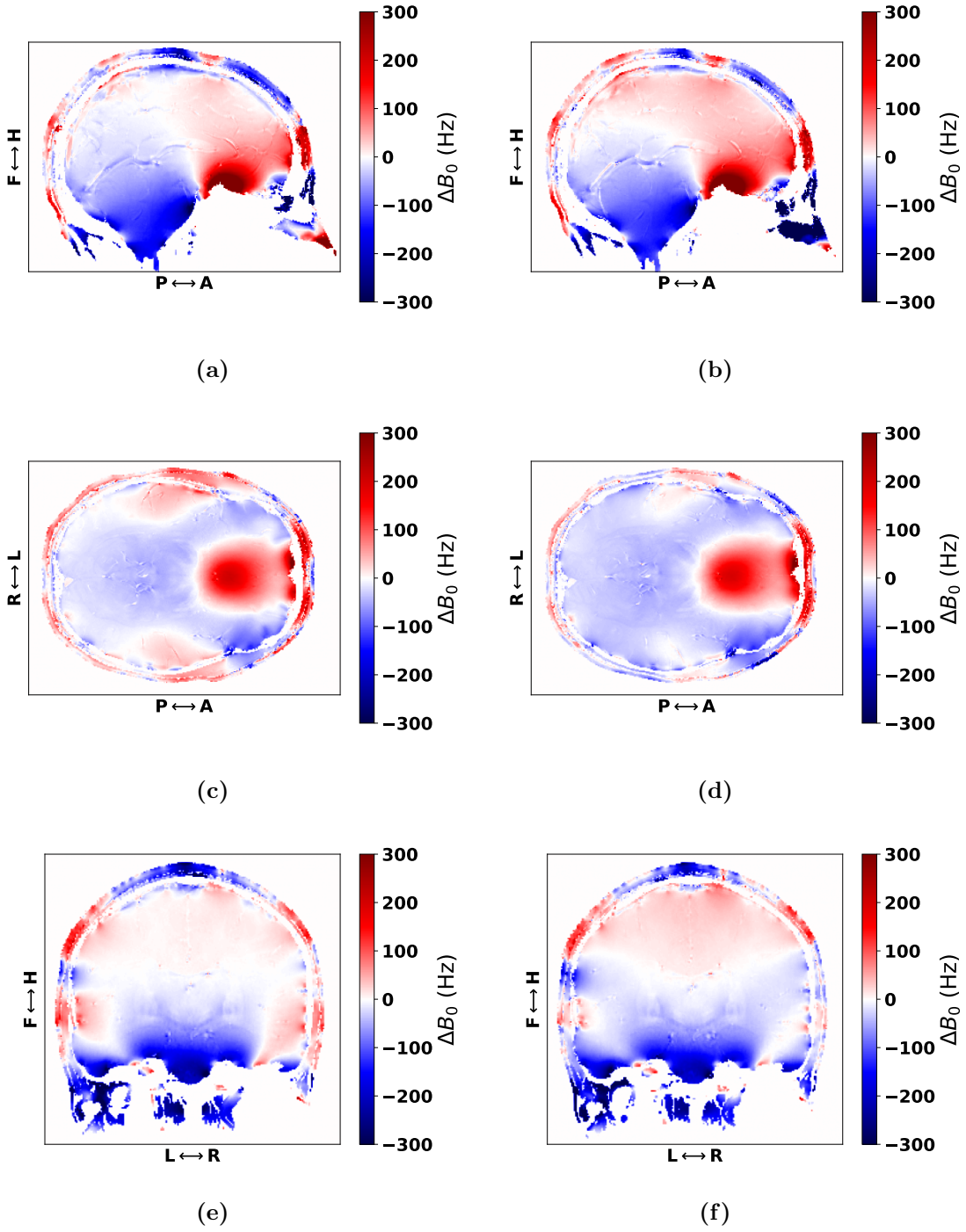

Figure 4.18: Side by side comparison of the obtained ΔB_0-maps after applying the iterative shim (a,c,e) and the standard shim (b,d,f) on the same volunteer. This is from session b_6 and c_{18} respectively.

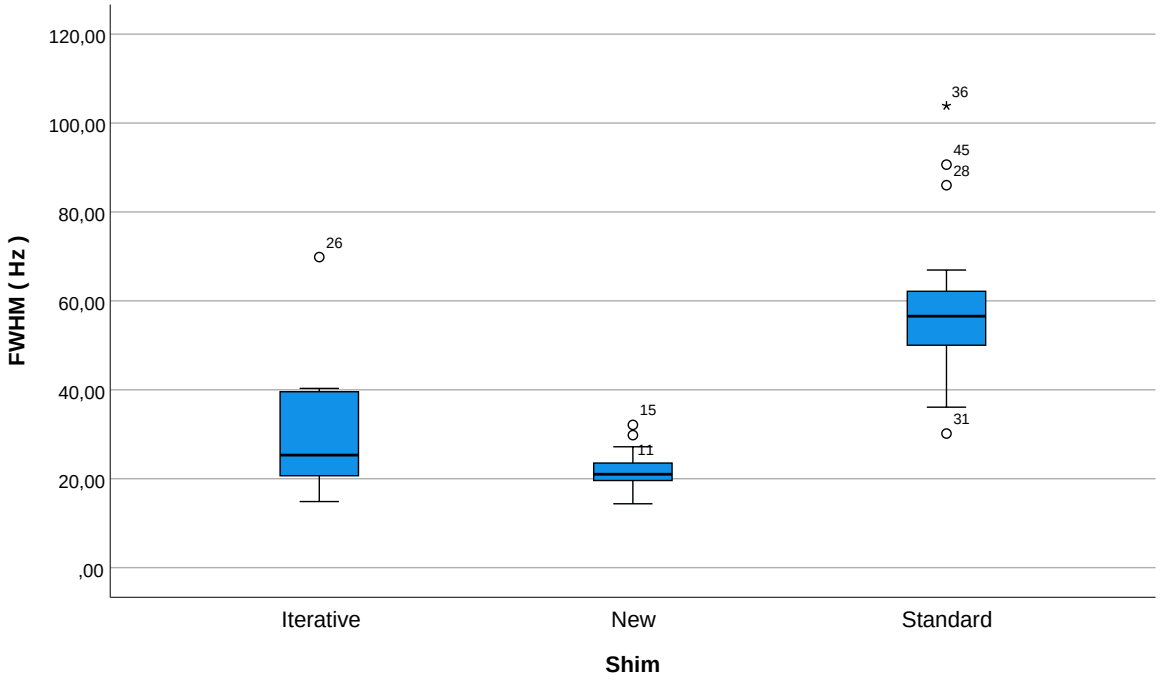

(a) Distribution of the FWHM for the three shim methods.

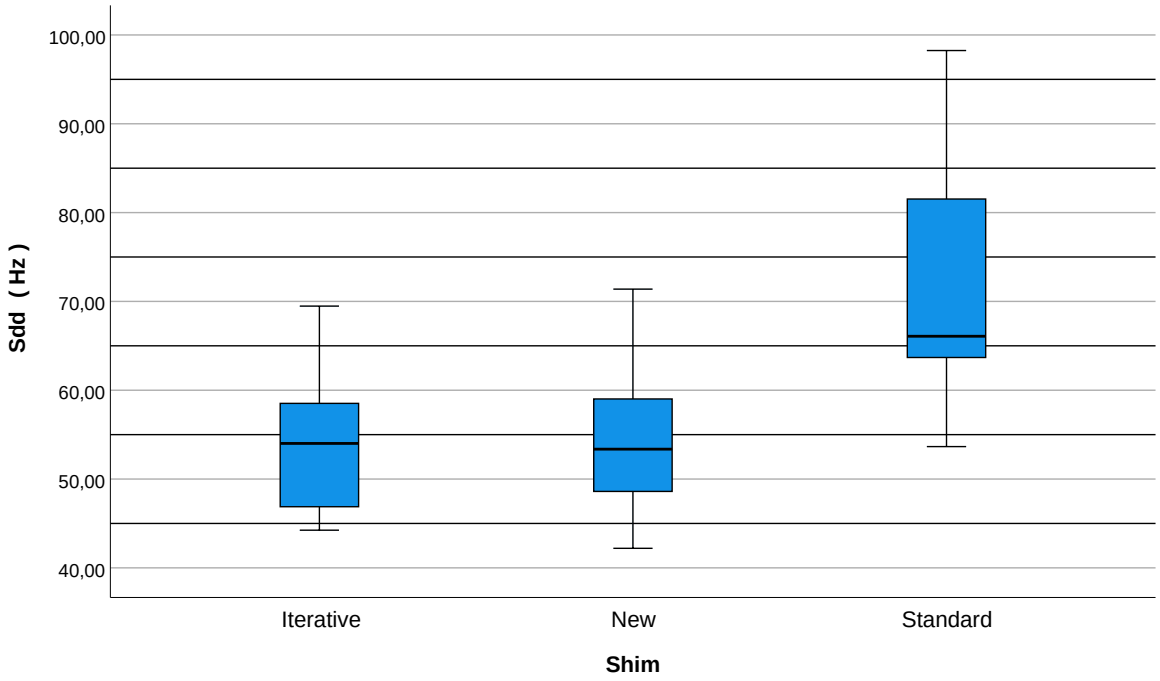

(b) Distribution of the standard deviation for the three shim methods.

Figure 4.19: The figure shows a box and whisker plot of the FWHM's (a) and standard deviation's (b) from the B_0-maps obtained after the different shimming methods.

Wilcoxon rank-sum test							
$\tilde{\mu_1}/\tilde{\mu_2}$	Variation	n_1	n_2	w_1	w_2	u_1	u-critical
New/Siemens	FWHM	18	17	172	458	1	102
	Sdd			199	431	28	
New/iterative	FWHM	19	5	217	83	27	23
	Sdd			233	67	43	
iterative/Siemens	FWHM	5	14	30	160	15	16
	Sdd			25	165	10	

Table 4.1: Results from the one-tailed Wilcoxon rank-sum test at $\alpha = 0.05$. n_1 and n_2 are the number of samples, w_1 and w_2 are the rank sums.

Wilcoxon rank-sum test, protocol								
$\tilde{\mu_1}/\tilde{\mu_2}$	protocol	Variation	n_1	n_2	w_1	w_2	u_1	u-critical
New/Siemens	sag	FWHM	7	14	28	203	0	26
		Sdd			44	187	16	
New/Siemens	tra	FWHM	11	5	67	69	1	12
		Sdd			68	68	2	

Table 4.2: One-tailed Wilcoxon rank-sum test at $\alpha = 0.05$ for the two different QSM protocols separately. n_1 and n_2 are the number of samples, w_1 and w_2 are the rank sums.

5 Discussion

5.1 B_0-mapping

5.1.1 Sequence development

Alternative implementation of second echo

The second echo was implemented like shown in figure 3.1, with a separate excitation pulse for each echo. Two alternative methods for implementing the second echo was also considered. Both of these methods were based on conducting two readouts for the same excitation pulse, with the only difference that the second readout could have two different polarities. Having both readouts within the same repetition time would give shorter scan times since the phase encoding gradients only have to be applied once for each line in the two k-spaces. Choosing the option of having opposite gradient polarity would give more freedom to the choice of ΔTE time since the second readout can start almost immediately after the first one as shown in figure 5.1a. Being able to reduce the ΔTE time also reduce the chance of getting phase wrapping from phase differences that evolve beyond the $[-\pi, \pi]$ range [16]. This change in gradient polarity would fill the same line in the two k-spaces in opposite directions. Accumulating phase due to local B_0 inhomogeneities will be unaffected by the gradient polarity, while phase difference from eddy currents will get opposite sign and hence give twice the contribution in the phase difference image [16]. This eddy component can be removed, but requires more post processing work. One way to assure more similar contribution from eddy currents is to use the same gradient polarity for both readouts. This requires a dephasing gradient

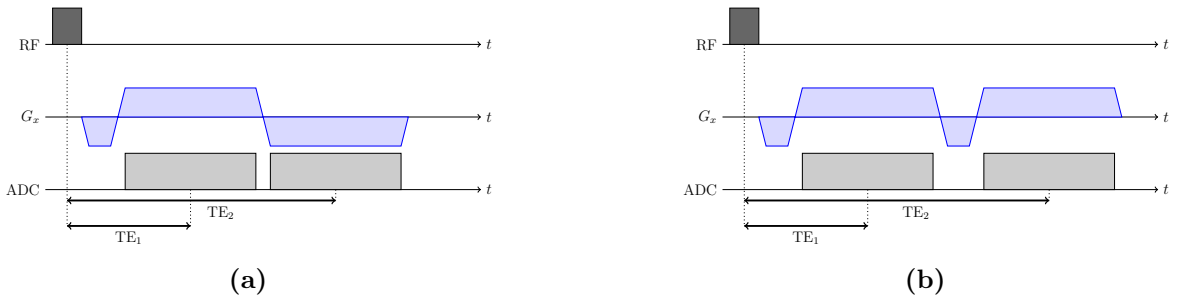

Figure 5.1: Alternative implementation of second echo (a): Bipolar readout gradient. (b): Monopolar readout gradient

between the readouts (figure 5.1b), and would therefore put some limitations to the time difference ΔTE, making the sequence less flexible. Choosing the implementation with one excitation for each echo would give the opportunity to adjust ΔTE arbitrary small with the cost of a slightly longer scan time. In addition, the conditions for the two readouts are more identical with respect to generated eddy currents.

5.1.2 B_0-map validation

In figure 4.1 a gradient is observed in the left-right direction of the vendor provided field map measured with both coils. The gradient decreases from approximately 0.8 μT on the left side of the phantom, to approximately -1.6 μT on the right side of the phantom, leaving a variation of 2.4 μT. Except from some variations on the edges of the phantom, the field is much more homogeneous in the sagittal slices. In our own B_0-mapping there is no gradient in any direction, and both sagittal and transverse slices for both coils are not varying more than 0.1 μT across the phantom, except for some higher variations along the edges.

In figure 4.2, we can see that the gradient in the vendor provided field mapping is also apparent in the histograms showing the B_0-variation inside the phantom mask. The variation makes the width of the two Siemens-histograms much wider than the ones from the new field map. As shown in table G.1, the standard deviation is therefore much higher for the vendor mapping. Regarding the new mapping, the histogram for the 32 channel coil is bigger and wider than the one for the tune up coil. The size difference is due to 4366 more voxels being counted in the 32 channel coil case. Over the 56 slices where the phantom is apparent, this means about 78 voxels extra per slice, which is due to small differences in the threshold mask made for the two different maps. The difference in standard deviation is due to the bigger field variations along the edges of the phantom for the 32 channel coil. This difference is also apparent in the vendor field mapping as seen in the two sagittal slices in figure 4.1. The reason for a smaller difference in standard deviation between the two coils for the vendor maps, can be explained by the gradient influencing the ΔB_0-distribution in the two maps more equally.

The gradient in the vendor field map is highly suspicious, since the B_0-field is expected to be passively shimmed. Therefore, it can not be used as a validation method of our own B_0-map. The comparison between the resonance peak and the ΔB_0 histogram in figure 4.3, can still be used. We would expect the width of the two histograms to be approximately equal as they both depend on the B_0-variations. The FWHM of 7.0 Hz for the resonance peak is very close to the the FWHM of 6.6 Hz for the ΔB_0 histogram and therefore works as a validation of our B_0-map sequence.

The comparison between the two field maps demonstrates one reason for developing our own sequence instead of using one provided by the vendor. If this vendor provided

mapping was used as a part of the shimming process without the gradient being discovered, there would be a systematic error in the shim currents for shim coils compensating for B_0-inhomogeneities in the left-right direction (mainly the Y-coil). The origin of the gradient was not investigated any further.

5.1.3 TR-optimization

First experiment

In figure 4.4a, the value of $\langle \Delta B^{diff} \rangle$ follows a trend resemble a damped oscillation over the course of the increasing TR-values. This means the B_0-field fluctuates during the pulse sequence, and gives an offset in the B_0-map. A DC-offset is not a problem, as it can be corrected for in the shim process by adjusting the excitation frequencies. On the other hand, changes in the spread of B^{diff} tells us that there is a systematic error in the B_0-map originating from something else than the underlying B_0-inhomogeneities. For the first TR-experiment, the standard deviation of the B^{diff}-map when TR=7 ms is almost 10 times bigger than the standard deviation for TR=40 ms. Hence, having a longer TR would eliminate some of the errors in a B_0-map. Even though an increase in TR would be expected to give smaller standard deviations, this is not always the case. For TR=7, 10, 15 and 25 ms, the standard deviations are all bigger than 0.08 μT, while for TR=20, 30, 35 and 40 ms, they are less than 0.04 μT. This can be seen in both the bars in figure 4.4a and in table H.1. This spread of the ΔB^{diff} distribution is reflected in the histograms in figure 4.5a were the histograms for TR=7, 10, 15 and 25 ms are wider compared to the histograms for TR=20, 30, 35 and 40 ms which are more narrow and sharp. The cause of the spread is apparent in the sagittal slices displayed in figure 4.6. Unlike the transverse slices in figure 4.7, where the distribution of ΔB^{diff} varies with less than 0.2 μT in any direction, there is a variation of the field in the head-foot direction in the sagittal slices. In the sagittal slice for TR=7, 15 and 25 ms, there is a gradient in the field from one side to another. This can be seen clearly in figure 4.8b. For TR=7 and 15 ms, the gradient increases from feet to head, with a steady change across the slice of about 0.6 μT and 0.4 μT respectively. The steady change in TR=25 ms is also about 0.4 μT, but the gradient goes in the opposite direction, from head to feet. For the TR = 10 ms slice, there is also a change in the field, but instead of having a steady drop across the slice, it drops with approximately 0.2 μT from one side to the middle and then increases with 0.2 μT to the other side. The variations across the head-feet direction is also apparent in for TR=20, 30, 35 and 40 ms slices, but not to the same degree as the other ones. In the left-right and posterior-anterior direction shown in figure 4.8a and 4.8c respectively, it can be seen that ΔB^{diff} does not change that much across the slice for any of the TR values longer than 10 ms. Only for TR=7 and 10 ms, the distribution varies a bit, but not much more than 0.2 μT.

Second, third and fourth experiment

In the second TR-experiment, the value of $\langle \Delta B^{diff} \rangle$ deviates less from zero (figure 4.4b and H.3). Also the ΔB^{diff} differences inside the phantom mask varies less, as displayed in the histogram plot in figure 4.5b and in figure 4.4b. The histograms are narrower and the bars are shorter. The largest deviations are found in the lowest TR-values, 7, 10 and 15 ms, where the standard deviations are all more than 5 times bigger than the standard deviation for TR=40 ms. In figure H.3 it can be seen that the variation is still mainly in the head-foot direction, even though the variation in the left-right and posterior-anterior direction for TR=7 and 10 ms is still a bit off to the right and anterior direction respectively. In the difference map ΔB^{diff}, we would expect the variations to be close to zero across the slice when eddy currents are not present.

After an additional increase in the rise times for the gradients in the read out direction, experiment 3 and 4 show earlier minimization of the standard deviation of ΔB^{diff}. A small oscillatory behaviour is still present in the $\langle \Delta B^{diff} \rangle$(TR)-plot 4.4c and 4.4d, but the width of the histograms in figure 4.5c and 4.5d are more similar to each other. For both of the two last experiments, only the standard deviation for TR=7.6 ms is more than two times bigger than the standard deviation of the longest TR tested (30 ms and 20 ms respectively). In both the sagittal and transverse slices (figures H.4, H.7, H.5 and H.5) the overall ΔB^{diff}-distribution in the phantom seems much more homogeneous. Also in the figures H.6b and H.9b, the value and variations of ΔB^{diff} are much more coincided in the head-feet direction compared to the previous two experiments.

Damped oscillatory field responses

Damped oscillatory offsets in the B_0-field have been observed in at least two other studies. MRS experiments conducted by Ryner et al. described the existence of oscillatory eddy currents [20]. They saw how the B_0-field changed following the pulsing of a gradient. In a later study by Wu et al., magnetic field fluctuations were found to have a close relationship with the acoustic noise caused by gradient pulses [21]. Ryner et al. discussed whether vibrations of the cryostat could be the cause of the oscillatory effect. Induced eddy currents in the cryostat could have caused the shift in B_0 if the cryostat vibrated due to sound wave transmission. This hypothesis was rejected as the oscillatory effect was seen immediately after the the gradient pulsing, and the transmission would be limited by the speed of sound. Wu et al. on the other hand, believed that the mechanical resonances of the gradient coil was the cause of the damped oscillatory field responses.

Effect of sequence changes

The TR measurements in this project could only provide an indication on how to minimising the bias in the B_0-maps. They were not designed as a study on eddy currents on

the system. More research is needed to uncover the origin of the offsets and variations in the B^{diff}-map. The field deviations across the slice varied the most along the head-feet (z) direction. Reduction in slew rate of all gradients and the additional increase in rise times of the read out gradients helped on reducing offset and the spread of ΔB^{diff}. The change from experiment 2 to 3 gives a strong indication that the rise time/slew rate of the readout gradients was related to the variations in the head-feet direction in the ΔB^{diff}-maps.

Between experiment 1 and 2, the RF-pulse was changed from a sinc pulse to a rectangular pulse. Together with the slew rate modifications, this reduced the offset and spread of ΔB^{diff} as seen in figure 4.8 and H.3. How the two changes affected the difference map separately can not be studied since they were implemented together. Despite this fact, the rectangular pulse is much shorter and allowed for shorter total scan time and testing of shorter repetition times. In addition, we got rid of the slab selective gradient, having one less gradient to consider.

After the last increase in the rise time of the readout gradients, the variations in ΔB^{diff} across the phantom are small. In figure H.6 and H.9 we see that there are minimal changes between the variations across the phantom for increasing TR. Hence, a shorter TR can be picked without decreasing the quality of the B_0-map. TR was set to 10 ms for future experiments. This was to be conservative and not use the absolute shortest TR possible. Using 10 ms instead of 7.6 ms would only increase the shim time with about 10 seconds.

5.2 Shim calibration

The calibration matrix in figure 4.9b has two diagonals going from northwest to southeast with some additional terms in the downer left corner. The upper most diagonal is the collection of self-terms of the different coils. Coil 4 on the x-axis has a term for SH no. 4 on the y-axis, coil 5 has a term for SH no. 5, etc. This pattern continues up to the 12th coil. The self-terms of the X, Y and Z coil, are off this diagonal. The reason for this is because the pure X, Y and Z SH functions in the $\mathbf{T}$-matrix have a different order than the currents going to the respective coils in the current vector $\mathbf{I}$.

Incorrect placement or rotation of the shim coils relative to the gradient isocenter leads to generation of lower order SH terms when running a higher order SH coil [13]. This does not seem to be the case for this scanner, as none of the elements along the uppermost diagonal in this calibration matrix has any elements above it.

The calibration matrix is not symmetric as demonstrated in [16] and [13], but has SH-functions up to 4th order to represent the coil-field instead of stopping at the fourth 3rd

order SH. As seen in the calibration matrix 4.9b, the cross-terms on the second diagonal are all appearing after the 12th SH-function. When calculating the currents to each coil, coils with elements on the second diagonal will have their field being represented by a more complex shape compared to only using the self-term. This will influence the optimized shim current and hence take into account the "impurity" of the coil to give a more accurate shim. If a symmetric calibration matrix was chosen like in [16], these cross-terms would not have been used. As an example, the Z-coil (at $x = 3$) in the calibration matrix as mainly two SH-functions representing its field; the self-term Z (at $y = 1$) and the cross-term Z^4 (at $y = 16$). A mixture of the two could potentially give a more accurate representation of the coil-field than when only the self-term is used. The calibration matrix was also calculated with a minimum norm least-squares algorithm that minimized both $||\mathbf{b_0} - \mathbf{b_0^{SH}}||$ and the value of $\mathbf{w}$, but this gave the exact same results as the Moore-Penrose pseudoinverse.

Different shim matrices

The two shim matrices in figure 4.9 are mainly similar, but have a few differences. Matrix 4.9a only has the two diagonals, while matrix 4.9b has some additional terms southwest of the lowest diagonal. If the threshold value of R^2 is set to a higher value, increasing it from 0.9 to 0.995, all these additional terms not included, and the two calibration matrices are identical. In other words, the calibration matrix from St. Olavs have been calculated with a higher requirement for correlation between the linear regression line and the plotted points to including terms. Juchem et al. seems to be using a R^2 value between 0.95 and 0.98 as the threshold when calibrating the $X^2 - Y^2$-coil in [16]. They also recommend using six or more shim settings for reliable regression analysis, which is why we used seven for our calibration. Figure 3.8b shows how the applied setting to the Z^2-coil changes the contribution of SH Z^4 in the shim field. If only five points were used, the value of R^2 would be 0.9965, and an additional term would be included in the calibration matrix. For future use of the calibration code, we will recommend to use a higher threshold value for R^2 than 0.9.

Test of calibration matrix

Figure 4.10a shows that the new calibration matrix successfully resets the extreme current setting of -602.0 μT/m to 4.4 μT/m. The other shim currents are also altered, but this is expected. In figure 4.10b, ΔB_0 before shimming has a very broad distribution with a standard deviation of 804.9 Hz, while the predicted ΔB_0 after shimming has a narrow distribution with a standard deviation of 2.2 Hz. This strongly indicates that the calibration is successful.

Test of shim process

There is excellent agreement between the predicted B_0-distribution in figure 4.11b and the measured B_0-distribution in figure 4.12 after applying the calculated currents from the shim codes. The standard deviation decrease with 1.2 Hz and the 90^{th} percentile range with 3.9 Hz for the measured map. This difference is small, and demonstrates that the whole shim process works; B_0-mapping, current calculations and the calibration.

5.3 Shim method comparison

Histograms and sagittal brainplots

The histogram plots in figure 4.16 strongly indicates that B_0-maps measured after applying the new shim gives more homogeneous ΔB_0-distributions than the standard shim. All histograms in figure 4.16a are narrow, while the histograms in figure 4.16b have an overall wider distribution.

The histograms from applying the iterative shimming method (figure 4.16c) have a mixture between narrow and wider histograms. E.g., session b_2 has a narrow histogram, while session b_7 has a wide one. The main reason for this is due to the human factor affecting the results. The radiographer handling the scanner at that particular day will be in charge of the number of iterations done by the standard shim, making the shim method less systematic.

When looking at figure 4.13, 4.14 and 4.15, it is obvious that all shims fail at correcting high B_0-offset inferior in the frontal lobe. This is not very surprising since one of the largest magnetic susceptibility differences in the brain occur in this area between brain tissue and air from the nasal passage [4]. Higher order shim coils producing more complex field shapes would be necessary in order to correct for that. One big difference between the different B_0-maps is the offset between the inferior temporal lobe/cerebellum and the rest of the brain. In the standard shim, this downer area has a strong negative offset (dark blue), while the for the new shim it is not apparent. Session b_5, b_6 and b_7 gave the worst B_0-maps after the iterative shim was carried out. In b_6 and b_7, the inferior temporal lobe/cerebellum has the negative offset. For session b_5 on the other hand, the offset does not look that big, suggesting that the offset in the temporal lobe/cerbellum is not the only thing reflecting the quality of the shim.

Same volunteer

Apart from the differences in the temporal lobe offset in the sagittal plane, there are also some differences seen in the transverse and coronal plane between the new and standard shim. Both shim methods fail to eliminate the offset in the anterior part of

the transverse slice (red spot) in figure 4.17c and 4.17d. In addition, the parts of the temporal lobe laying close to the auditory passages have a high offset for both shims, but maybe slightly higher for the new shim, indicated by figure 4.17e and 4.17f. Still, a big fraction of the remaining parts of the brain are colored white for the new shim and blue for the standard shim, giving a much higher gradient between the anterior frontal lobe/audatory passages and the rest of the brain when using the standard shim.

In figure 4.18, no huge differences are seen between the iterative and the standard shim, except a slightly higher B_0-offset for the standard shim in the superior part of the brain. This is not unexpected since session b_6 had a wide B_0-distribution, suggesting that not that many iterations of the standard shim were performed.

Boxplot, FWHM and standard deviation

The median value of the FWHM is quite close between the iterative and the new shim, while the median for the standard shim is bigger. When it comes to spread in FWHM, the iterative and the standard shim seems to have more equal sized boxes, while the new shim has more narrow box and whiskers (figure 4.19a). For the standard deviation (figure 4.19b), on the other hand, the median value is still smallest and closest between the iterative and the new shim, but the spread is not notably smaller for the new shim. The spread is biggest for the standard shim and almost identical between the iterative and the new shim.

The bigger variation in standard deviation compared to FWHM could be explained by sdd being more sensitive to extreme values. The red area in the frontal lobes in figure 4.13 might be the cause of this. The size of this red spot would be affected by the volunteers anatomy and could therefore mean that the standard deviation is more influenced by an anatomy change than the FWHM. The FWHM is not altered by some extreme values that make the histogram more heavy-tailed, and might be a better measurement on the quality of the shim, since high-level B_0-homogeneity is difficult to reach, for instance by the nasal cavity in the frontal lobe[16].

5.3.1 Statistical analysis

The Wilcoxon rank-sum test presented in table 4.1 states that the median of both the FWHM and the standard deviation is statistically significantly bigger when using the standard shim vs. the iterative or new shim. Comparison of the iterative shim against the new shim on the other hand, does not give a small enough u_1 value to reject the null-hypothesis. Despite this fact, it is hard to recommend the use of the iterative shim due to being less systematic. Since the shim quality depends on the number of iterations, this method will not be reproducible across scanner operators.

Another statistical test was considered to be used for comparing the mean of the FWHM and the standard deviation. Welch's t-test, or unequal variances t-test, compares the mean value of two independent datasets[18]. The unknown variances of the datasets are assumed to be different and therefore have to be estimated. The size of the two datasets does not have to be equal, but needs to be normally distributed. To use Welch' t-test we need to assume that both the FWHM and sdd from all three shim methods are normally distributed. This is a bold assumption since the sample sizes are all far less than 30, which is usually the guideline for when the central limit theorem applies [18]. If the sample size is less than 30, the central limit theorem can still apply if the underlying distribution is not too far from a normal distribution [18], but for this particular case, we do not have enough information to know if this is the case. One possibility for using the Welch's t-test when non-normality is evident, is to rank the data before doing the test [22]. A ranked Welch's t-test was not conducted in this thesis. Fagerland [23] suggest using the Wilcoxon rank-sum test when the sample size is small.

Comparison between similar protocols

The two tests between the new shim and the standard shim when comparing for the two different QSM protocols separately, are displayed in table 4.2. Since the sample sizes are reduced, the value of u-critical is much smaller, requiring a smaller rank-sum for the new shim to reject the null-hypothesis. Still, the test clearly states that the new shim gives better results than the standard shim, independent of the used protocol.

5.4 Further work

We have seen that the newly developed shim is statistically significantly better than the standard implemented method, without uncovering where the weaknesses in the method come from. By investigating the B_0-mapping, current optimization and calibration of the standard shim separately, the weaknesses can be found. Since we know these three steps work in the new shim method, they can be replaced one at the time by the step in the standard shim method. For example, could our B_0-shim be tested on the vendor's B_0-map to see how the shim is affected.

In the TR-optimization part of the project, the variations in the difference map ΔB^{diff} was mainly found in the head feet direction of the phantom. The experiment could be redone with x and y as the readout direction, using for instance 6 TR-values, with 3 different gradient rise times. The resulting difference maps could give an indication of whether the readout direction has any influence on the variations. We would still expect to see some variation in the ΔB^{diff}-field in the head feet direction if the cylindrical symmetry of the scanner is the cause.

The calibration of the shim coil system was done by finding the combination of 4th order solid spherical harmonics function that best represented the different coil fields. A new study could e.g. test the use of 5th and 6th order SH functions in the calibration matrix to see if it gives a better shim.

We saw in the comparison part of the thesis that the QSM B_0-map was affected by the applied shim method. A new study should be carried out to investigate the effect of B_0-inhomogeneity on the calculated QSM value.

6 Conclusion

In this master project, the aim was to develop a new shim method that could generate good shim values that were reproducible across volunteers and scanner operators. This was done by implementing a dual-echo gradient recalled echo sequence with two separate excitation pulses where the purpose was to make the conditions for the two readouts as similar as possible. The repetition time between the readouts was optimized to minimize the spread in a difference map between two ΔB_0-maps sampled with opposite gradient polarity. A calibration of the shim coil system was successfully carried out by representing each of the coil fields with 4th order solid spherical harmonic functions. The new shim method was compared with the standard vendor-implemented shim method by testing it on two unpaired groups of volunteers and performing a Wilcoxon rank-sum test on the spread in the resulting B_0-map.

Offsets and variations in the difference map were successfully minimized by adjusting the slew rate of the gradients, which allowed for usage of shorter repetition times. The obtained calibration matrix for the shim coils gave good results, both when tested on phantom and volunteer. When comparing the spread of ΔB_0 after applying the new shim method and the standard implemented method, the statistical test strongly suggests that the new shim method is better. We conclude this thesis by stating that we have successfully improved the shim method on the 7 T Magnetom Terra scanner at NTNU.

7 Bibliography

[1] William T. Clarke et al. "Multi-site harmonization of 7 tesla MRI neuroimaging protocols". In: *NeuroImage* 206.November 2019 (2020), p. 116335. ISSN: 10959572. DOI: 10.1016/j.neuroimage.2019.116335. URL: https://doi.org/10.1016/j.neuroimage.2019.116335.

[2] Christoph Juchem et al. "Dynamic shimming of the human brain at 7 T". In: *Concepts in Magnetic Resonance Part B: Magnetic Resonance Engineering* (2010). ISSN: 15525031. DOI: 10.1002/cmr.b.20169.

[3] Karl Landheer and Christoph Juchem. "RESEARCH ARTICLE FAMASITO : FASTMAP Shim Tool towards user-friendly single- step B 0 homogenization". In: January 2020 (2021), pp. 1–13. DOI: 10.1002/nbm.4486.

[4] Christoph Juchem and Robin A. de Graaf. "B0 magnetic field homogeneity and shimming for in vivo magnetic resonance spectroscopy". In: *Analytical Biochemistry* 529 (2017), pp. 17–29. ISSN: 10960309. DOI: 10.1016/j.ab.2016.06.003.

[5] Michael Hock et al. "B0 shimming of the human heart at 7T". In: *Magnetic Resonance in Medicine* 85.1 (2021), pp. 182–196. ISSN: 15222594. DOI: 10.1002/mrm.28423.

[6] Robert W. Brown et al. *Magnetic resonance imaging physical principles and sequence design*. Wiley-Liss, 2014.

[7] Robin A. de Graaf. *in vivo NMR Spectroscopy, Principles and Techniques*. second. John Wiley & Sons Ltd, 2007.

[8] Stephen Blundell. *Magnetism in Condensed Matter*. Oxford university press, 2001.

[9] Dominik Weishaupt, Victor D. Köchli, and Borut Marincek. *How does MRI work? An Introduction to the Physics and Function of Magnetic Resonance Imaging*. second. Springer, 2008.

[10] David J. Griffiths. *Introduction to Electrodyniamics*. fourth. Chap 6. Pearson, 2013.

[11] F. Bloch. "Nuclear induction". In: *Physical Review* 70.7-8 (1946), pp. 460–474. ISSN: 0031899X. DOI: 10.1103/PhysRev.70.460.

[12] Donald W. McRobbie et al. *MRI from Picture to Proton*. third. Cambridge university press, 2017.

[13] Robin A. de Graaf and Christoph Junchem. *Magnetic Resonance Technology: Hardware and System Component Design*. The Royal Society of Chemistry, 2016.

[14] M. A. Bernstein, K. F. King, and X. J. Zhou. *Handbook of MRI Pulse Sequences*. Elsevier Academic Press, 2004.

[15] Mary A. McLean et al. "Characterization and correction of center-frequency effects in X-nuclear eddy current compensations on a clinical MR system". In: *Magnetic Resonance in Medicine* June (2020), pp. 1–7. ISSN: 15222594. DOI: 10.1002/mrm.28607.

[16] Christoph Juchem et al. "B0 shimming for in vivo magnetic resonance spectroscopy: Experts' consensus recommendations". In: *NMR in Biomedicine* December 2019 (2020), pp. 1–20. ISSN: 10991492. DOI: 10.1002/nbm.4350. URL: https://doi.org/10.1002/nbm.4350.

[17] Pascal P.R. Ruetten, Jonathan H. Gillard, and Martin J. Graves. "Review article: Introduction to quantitative susceptibility mapping and susceptibility weighted imaging". In: *British Journal of Radiology* 92.1101 (2019). ISSN: 1748880X. DOI: 10.1259/bjr.20181016.

[18] Ronald E. Walpole et al. *Probability & Statistics for Engineers & Scientists*. Eighth. Pearson Education, Inc, 2007.

[19] Inc. The MathWorks. *Moore-Penrose pseudoinverse*. 2021. URL: https://se.mathworks.com/help/matlab/ref/pinv.html#mw_ffa95973-29a2-48a1-adb0-5a4214e0d9cf.

[20] LN Ryner, P Stroman, and To Wessel. "Effect of oscillatory eddy currents on MR spectroscopy". In: *Proceedings of the ISMRM* (1998), p. 100. URL: http://cds.ismrm.org/ismrm-1998/PDF7/p1903.pdf.

[21] Alan Barnett. "Gradient-induced acoustic and magnetic field fluctuations in a 4T whole-body MR imager". In: *Magnetic Resonance in Medicine* 46.2 (2001), p. 207. ISSN: 07403194. DOI: 10.1002/mrm.1179.

[22] Graeme D. Ruxton. "The unequal variance t-test is an underused alternative to Student's t-test and the Mann-Whitney U test". In: *Behavioral Ecology* 17.4 (2006), pp. 688–690. ISSN: 10452249. DOI: 10.1093/beheco/ark016.

[23] Morten W. Fagerland. "T-tests, non-parametric tests, and large studiesa paradox of statistical practice?" In: *BMC Medical Research Methodology* 12 (2012). ISSN: 14712288. DOI: 10.1186/1471-2288-12-78.

Appendix A

Rotating frame of reference

This derivation is based on material taken from [6].
A primed coordinate system, the *rotating frame of reference*, rotates around $\mathbf{\Omega}$ counter-clockwise with angular velocity $|\mathbf{\Omega}|$. $\mathbf{\Omega}$ is a fixed vector in the fixed coordinate system, *the lab frame*, parallel with the z-axis. For a vector $\mathbf{X}$, fixed in the rotating frame, the rate of change with respect to the lab frame is

$$\frac{\mathrm{d}\mathbf{X}}{\mathrm{d}t} = \mathbf{\Omega} \times \mathbf{X} \tag{A.1}$$

A vector $\mathbf{V}$ that is not fixed in the primed frame either, will have some time dependency in both frames. In the lab frame

$$\mathbf{V}(t) = V_x(t)\hat{\mathbf{x}} + V_y(t)\hat{\mathbf{y}} + V_z(t)\hat{\mathbf{z}} \tag{A.2}$$

while in the primed frame

$$\mathbf{V}'(t) = V_{x'}(t)\hat{\mathbf{x}}' + V_{y'}(t)\hat{\mathbf{y}}' + V_{z'}(t)\hat{\mathbf{z}}' \tag{A.3}$$

$\mathbf{V}(t) = \mathbf{V}'(t)$ since the two expressions are referring to the same vector. Their derivative should then also be the same.

$$\frac{\mathrm{d}\mathbf{V}}{\mathrm{d}t} = \frac{\mathrm{d}V_x}{\mathrm{d}t}\hat{\mathbf{x}} + \frac{\mathrm{d}V_y}{\mathrm{d}t}\hat{\mathbf{y}} + \frac{\mathrm{d}V_z}{\mathrm{d}t}\hat{\mathbf{z}} \tag{A.4}$$

The derivative is taken with respect to the lab frame, and therefore the primed axes will be time dependent. The derivative of $\mathbf{V}'$ with respect to the lab frame is

$$\frac{\mathrm{d}\mathbf{V}'}{\mathrm{d}t} = \left(\frac{\mathrm{d}\mathbf{V}}{\mathrm{d}t}\right)' + V_{x'}(t)\frac{\mathrm{d}\hat{\mathbf{x}}'}{\mathrm{d}t} + V_{y'}(t)\frac{\mathrm{d}\hat{\mathbf{y}}'}{\mathrm{d}t} + V_{z'}(t)\frac{\mathrm{d}\hat{\mathbf{z}}'}{\mathrm{d}t} \tag{A.5}$$

where

$$\left(\frac{\mathrm{d}\mathbf{V}}{\mathrm{d}t}\right)' = \frac{\mathrm{d}V_{x'}}{\mathrm{d}t}\hat{\mathbf{x}}' + \frac{\mathrm{d}V_{y'}}{\mathrm{d}t}\hat{\mathbf{y}}' + \frac{\mathrm{d}V_{z'}}{\mathrm{d}t}\hat{\mathbf{z}}'$$

is the time derivative of $\mathbf{V}'(t)$ with respect to the primed frame. The remaining part of equation (A.5) can be rewritten with help from equation (A.1):

$$V_{x'}(t)\frac{\mathrm{d}\hat{\mathbf{x}}'}{\mathrm{d}t} + V_{y'}(t)\frac{\mathrm{d}\hat{\mathbf{y}}'}{\mathrm{d}t} + V_{z'}(t)\frac{\mathrm{d}\hat{\mathbf{z}}'}{\mathrm{d}t}$$

$$= V_{x'}(t)\boldsymbol{\Omega} \times \hat{\mathbf{x}}' + V_{y'}(t)\boldsymbol{\Omega} \times \hat{\mathbf{y}}' + V_{z'}(t)\boldsymbol{\Omega} \times \hat{\mathbf{z}}'$$

$$= \boldsymbol{\Omega} \times \mathbf{V}' = \boldsymbol{\Omega} \times \mathbf{V} \tag{A.6}$$

We now use the fact that the two derivatives must be equal by combining (A.4), (A.5) and use the result from (A.6) to find the relationship between the two derivatives.

$$\frac{\mathrm{d}\mathbf{V}}{\mathrm{d}t} = \left(\frac{\mathrm{d}\mathbf{V}}{\mathrm{d}t}\right)' + \boldsymbol{\Omega} \times \mathbf{V} \tag{A.7}$$

A magnetic moment $\boldsymbol{\mu}$ in a magnetic field $\mathbf{B} = B_0\hat{\mathbf{z}}$ will in the rotating reference system follow equation (A.7):

$$\frac{\mathrm{d}\boldsymbol{\mu}}{\mathrm{d}t} = \left(\frac{\mathrm{d}\boldsymbol{\mu}}{\mathrm{d}t}\right)' + \boldsymbol{\Omega} \times \boldsymbol{\mu} \tag{A.8}$$

We already know that

$$\frac{\mathrm{d}\boldsymbol{\mu}}{\mathrm{d}t} = \gamma\boldsymbol{\mu} \times \mathbf{B}$$

and can use this to find the rate of change in the primed frame

$$\left(\frac{\mathrm{d}\boldsymbol{\mu}}{\mathrm{d}t}\right)' = \frac{\mathrm{d}\boldsymbol{\mu}}{\mathrm{d}t} - \boldsymbol{\Omega} \times \boldsymbol{\mu}$$

$$= \gamma\boldsymbol{\mu} \times \mathbf{B} + \boldsymbol{\mu} \times \boldsymbol{\Omega} = \gamma\boldsymbol{\mu} \times \left(\mathbf{B} + \frac{\boldsymbol{\Omega}}{\gamma}\right)$$

$$\left(\frac{\mathrm{d}\boldsymbol{\mu}}{\mathrm{d}t}\right)' = \gamma\boldsymbol{\mu} \times \mathbf{B}_{eff} \tag{A.9}$$

where $\mathbf{B}_{eff} = \mathbf{B} + \frac{\boldsymbol{\Omega}}{\gamma}$.

Appendix B

Equilibrium magnetization

This derivation is based on material taken from [6].
The probability of finding a system in a state with energy ϵ while in contact with a heat reservoir with temperature T is given by

$$P(\epsilon) = \frac{e^{-\epsilon/kT}}{Z} \tag{B.1}$$

where Z is the partition function, the sum over all possible energy states

$$Z = \sum_i e^{-E_i/kT}$$

and k is the Boltzmann constant. For this case, the system is a single spin in thermal contact with N other spins with temperature T. The number N is assumed to be very large and confined within a volume V where all N spins are assumed to have the same phase. The spins in V are then called an *isochromat*. The average value of the longitudinal magnetization $\langle M_z \rangle$ can be calculated through the average value of the z-component of the magnetic moment, $\langle \mu_z \rangle$:

$$M_0 = \langle M_z \rangle = \frac{N}{V} \langle \mu_z \rangle$$

$$M_0 = \frac{N}{V} \sum_{m=-s}^{s} P(\epsilon(m)) \mu_z(m) \tag{B.2}$$

Where ϵ and μ_z can be shown to be

$$\epsilon = -m\hbar\omega_0 \qquad \mu_z = m\gamma\hbar \tag{B.3}$$

Defining $\rho_0 = \frac{N}{V}$ to be the density of spins per unit volume, and using (B.1) the equilibrium magnetization is then

$$M_0 = \rho_0 \frac{\sum_{m=-s}^{s} m\gamma\hbar e^{m\hbar\omega_0/kT}}{\sum_{m=-s}^{s} e^{m\hbar\omega_0/kT}} \tag{B.4}$$

For operational frequencies in MRI used at room temperature, the value of $\hbar\omega_0/kT$ is very small and the exponential can be approximated with a Taylor expansion:

$$e^{mu} \approx 1 + mu \qquad \text{when} \qquad u \ll 1$$

$$M_0 = \rho_0\gamma\hbar\frac{\sum_{m=-s}^{s} m(1+mu)}{\sum_{m=-s}^{s}(1+mu)} \tag{B.5}$$

here, $u = \hbar\omega_0/kT$. The sum in the numerator can be calculated as

$$\sum_{m=-s}^{s} m(1+mu) = \sum_{m=-s}^{s} m + m^2u = \sum_{m=-s}^{s} m^2u = u\frac{s(2s+1)(s+1)}{3} \tag{B.6}$$

where in the last step, a summation formula for m^2 in integer steps is used[1]. Note that since the sum is taken from $-s$ to s, all odd numbered powers of m sum to zero. The expression of the denumerator is:

$$\sum_{m=-s}^{s} (1+mu) = \sum_{m=-s}^{s} 1 = 2s+1 \tag{B.7}$$

Inserting the two sums back into equation (B.5) gives

$$M_0 = \rho\gamma\hbar\frac{us\cancel{(2s+1)}(s+1)}{3\cancel{(2s+1)}} = \frac{\rho_0\gamma\hbar^2\omega_0}{3kT}s(s+1) \tag{B.8}$$

The final expression is obtained by using $\omega_0 = \gamma B_0$ and the spin value for protons, $s = 1/2$:

$$M_0 = \frac{1}{4}\rho_0\frac{\gamma^2\hbar^2}{kT}B_0 \tag{B.9}$$

[1] $\sum_{m=-s}^{s} m^2 = \frac{s(2s+1)(s+1)}{3}$

Appendix C

Signal from gradient echo

This derivation is based on material taken from [14].
The longitudinal magnetization decreases from M_{z0} to M_{z1} according to

$$M_{z1} = M_{z0}\cos(\alpha) \tag{C.1}$$

after an excitation of flip angle α. The Bloch equation for longitudinal relaxation (2.20) gives the time dependence of $M_z(t)$

$$M_z(t) = M_{z1}e^{-\mathrm{TR}/T_1} + M_0(1 - e^{-\mathrm{TR}/T_1})$$

$$M_z(t) = M_{z0}\cos(\alpha)e^{-\mathrm{TR}/T_1} + M_0(1 - e^{-\mathrm{TR}/T_1}).$$

When the steady state of the magnetization is reached, $M_z(t) = M_{z0}$ and the analytical value of M_{z0} can be calculated:

$$M_{z0} = M_{z0}\cos(\alpha)e^{-\mathrm{TR}/T_1} + M_0(1 - e^{-\mathrm{TR}/T_1})$$

$$M_{z0}(1 - \cos(\alpha)e^{-\mathrm{TR}/T_1}) = M_0(1 - e^{-\mathrm{TR}/T_1})$$

$$M_{z0} = M_0\frac{(1 - e^{-\mathrm{TR}/T_1})}{(1 - \cos(\alpha)e^{-\mathrm{TR}/T_1})}$$

The signal from a spoiled GRE sequence is caused by a rephasing of the FID at time TE and is proportional to $M_{z0}\sin(\alpha)e^{-\mathrm{TE}/T_2^*}$. Inserting the value of M_{z0} gives the signal

$$S_{\mathrm{GRE}} \propto M_0\frac{(1 - e^{-\mathrm{TR}/T_1})}{(1 - \cos(\alpha)e^{-\mathrm{TR}/T_1})}\sin(\alpha)e^{-\mathrm{TE}/T_2^*} \tag{C.2}$$

At position $\mathbf{r}$, a time t after a RF flip angle of α, the signal is proportional to

$$S_{\mathrm{GRE}}(\mathbf{r}, t, \alpha) \propto M_0(\mathbf{r})F_{\mathrm{GRE}}(\mathbf{r}, t, \alpha) \tag{C.3}$$

where

$$F_{\mathrm{GRE}}(\mathbf{r}, t, \alpha) = \frac{(1 - e^{-\mathrm{TR}/T_1(\mathbf{r})})}{(1 - \cos(\alpha)e^{-\mathrm{TR}/T_1(\mathbf{r})})}\sin(\alpha)e^{-t/T_2^*(\mathbf{r})} \tag{C.4}$$

is the relaxation factor for the GRE sequence. Here it is assumed that the longitudinal magnetization has reached a steady state for this TR.

Appendix D

Magnetic field in free space

It can be shown that the magnetic field in free space obeys Laplace's equation by combining the two Maxwell equations for magnetic fields

$$\nabla \cdot \mathbf{B} = 0 \tag{D.1}$$

$$\nabla \times \mathbf{B} = 1/\mu(\mathbf{J} + \epsilon \partial \mathbf{E}/\partial t) \tag{D.2}$$

where $\mathbf{B}$ is the magnetic flux density, $\mathbf{J}$ is a current and $\partial \mathbf{E}/\partial t$ is a time-changing electric field. ϵ and μ are permeability constants.
Inside the MRI scanner, there are no changing electric fields or currents, hence equation (D.2) turns into

$$\nabla \times \mathbf{B} = 0 \tag{D.3}$$

Written out, (D.1) and (D.3) yields

$$\nabla \cdot \mathbf{B} = \frac{\partial B_x}{\partial x} + \frac{\partial B_y}{\partial y} + \frac{\partial B_z}{\partial z} = 0 \tag{D.4}$$

$$\nabla \times \mathbf{B} = \left[\frac{\partial B_z}{\partial y} - \frac{\partial B_y}{\partial z}, \frac{\partial B_x}{\partial z} - \frac{\partial B_z}{\partial x}, \frac{\partial B_y}{\partial x} - \frac{\partial B_x}{\partial y} \right] = \mathbf{0} \tag{D.5}$$

Taking the partial derivative with respect to x of equation (D.4) gives

$$\frac{\partial}{\partial x}(\nabla \cdot \mathbf{B}) = \frac{\partial^2 B_x}{\partial x^2} + \frac{\partial^2 B_y}{\partial x \partial y} + \frac{\partial^2 B_z}{\partial x \partial z} = 0 \tag{D.6}$$

We know from (D.5) that $\partial B_z/\partial x = \partial B_x/\partial z$ and $\partial B_y/\partial x = \partial B_x/\partial y$ and hence is

$$\frac{\partial^2 B_z}{\partial z \partial x} = \frac{\partial^2 B_x}{\partial z^2} \quad \text{and} \quad \frac{\partial^2 B_y}{\partial y \partial x} = \frac{\partial^2 B_x}{\partial y^2} \tag{D.7}$$

when taken the partial derivative with respect to z and y on each side respectively. Last step is to insert (D.7) into (D.6)

$$\frac{\partial^2 B_x}{\partial x^2} + \frac{\partial^2 B_x}{\partial y^2} + \frac{\partial^2 B_x}{\partial z^2} = 0$$

$$\nabla^2 B_x = 0 \tag{D.8}$$

which is Laplace's equation. $\nabla^2 B_y = 0$ and $\nabla^2 B_z = 0$ can be shown in an analogous way.

Appendix E

Axes of the calibration matrix

Table E.1: Spherical harmonics of order n and degree m and their numbering on the y-axis in the calibration matrix.

Numbering	n	m	Common name [13]
0	0	0	Z^0
1	1	0	Z
2	1	1	X
3	1	-1	Y
4	2	0	Z^2
5	2	1	ZX
6	2	-1	ZY
7	2	2	X^2-Y^2
8	2	-2	XY
9	3	0	Z^3
10	3	1	Z^2X
11	3	-1	Z^2Y
12	3	2	$Z(X^2-Y^2)$
13	3	-2	ZXY
14	3	3	X^3
15	3	-3	Y^3
16	4	0	Z^4
17	4	1	Z^3X
18	4	-1	Z^3Y
19	4	2	Z^2C^2
20	4	-2	Z^2S^2
21	4	3	ZC^3
22	4	-3	ZS^3
23	4	4	X^4
24	4	-4	Y^4

Table E.2: The coil representing spherical harmonics of order n and degree m and their numbering on x-axis in calibration matrix.

Numbering	n	m	Common name	Coil ID
1	1	1	X	A11
2	1	-1	Y	B11
3	1	0	Z	A10
4	2	0	Z^2	A20
5	2	1	ZX	A21
6	2	-1	ZY	B21
7	2	2	X^2-Y^2	A22
8	2	-2	XY	B22
9	3	0	Z^3	A30
10	3	1	Z^2X	A31
11	3	-1	Z^2Y	B31
12	3	2	$Z(X^2-Y^2)$	A32

Appendix F

Sequence Development

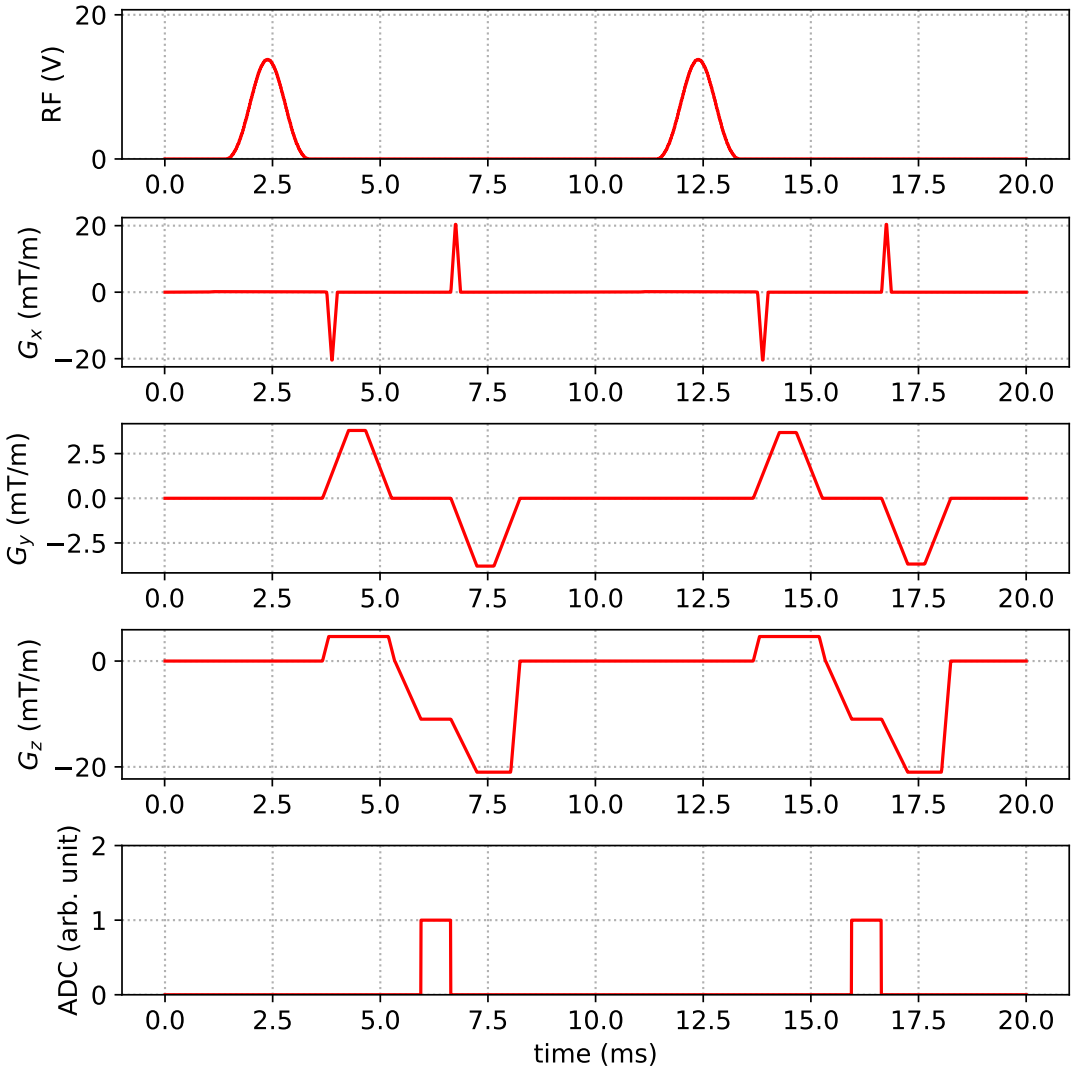

Figure F.1: A section of the example sequence before adjustments. TE=3.9 ms and TR=10 ms.

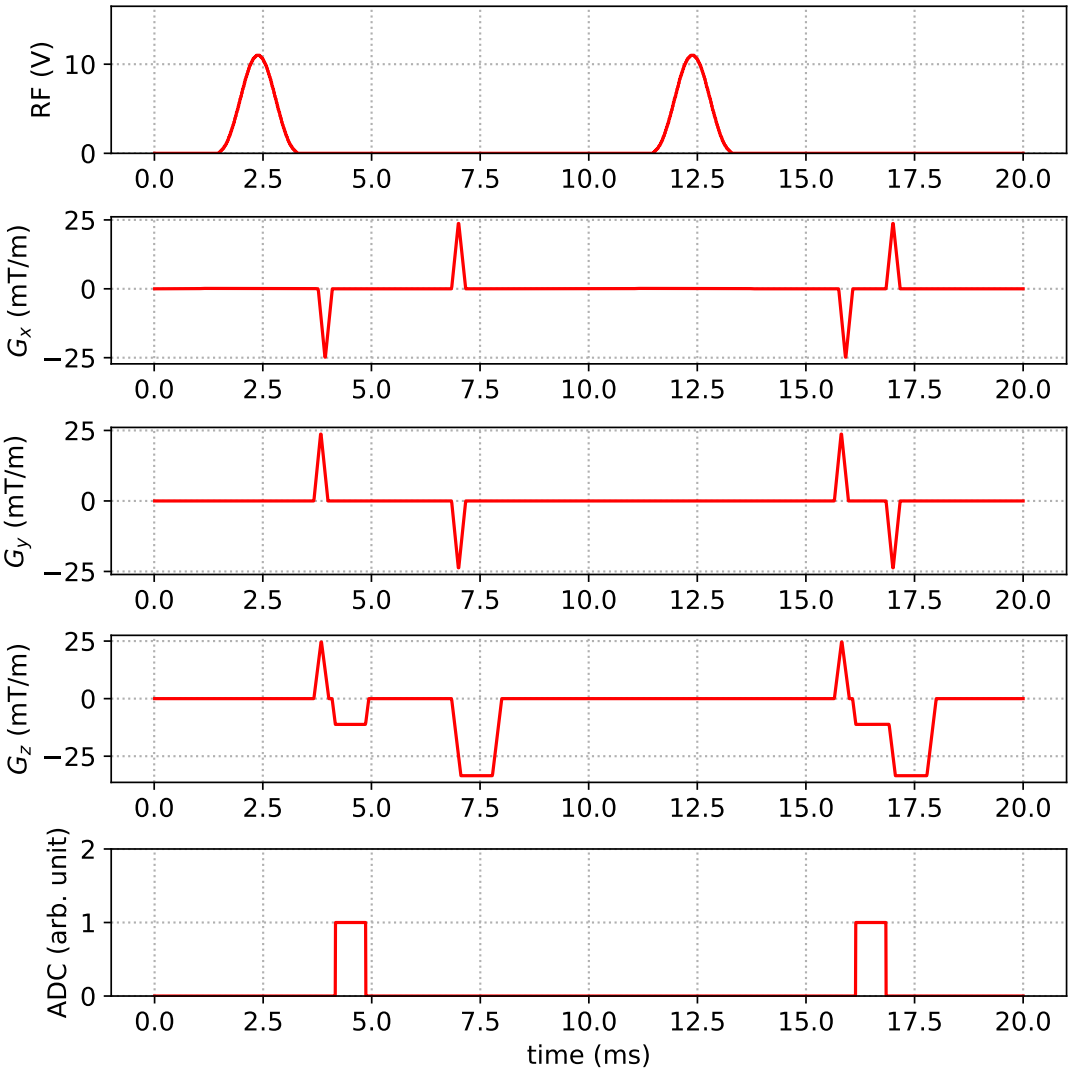

Figure F.2: A section of the sequence after the first adjustments. TR=10 ms, TE_1=2.12 ms and TE_2=4.10 ms.

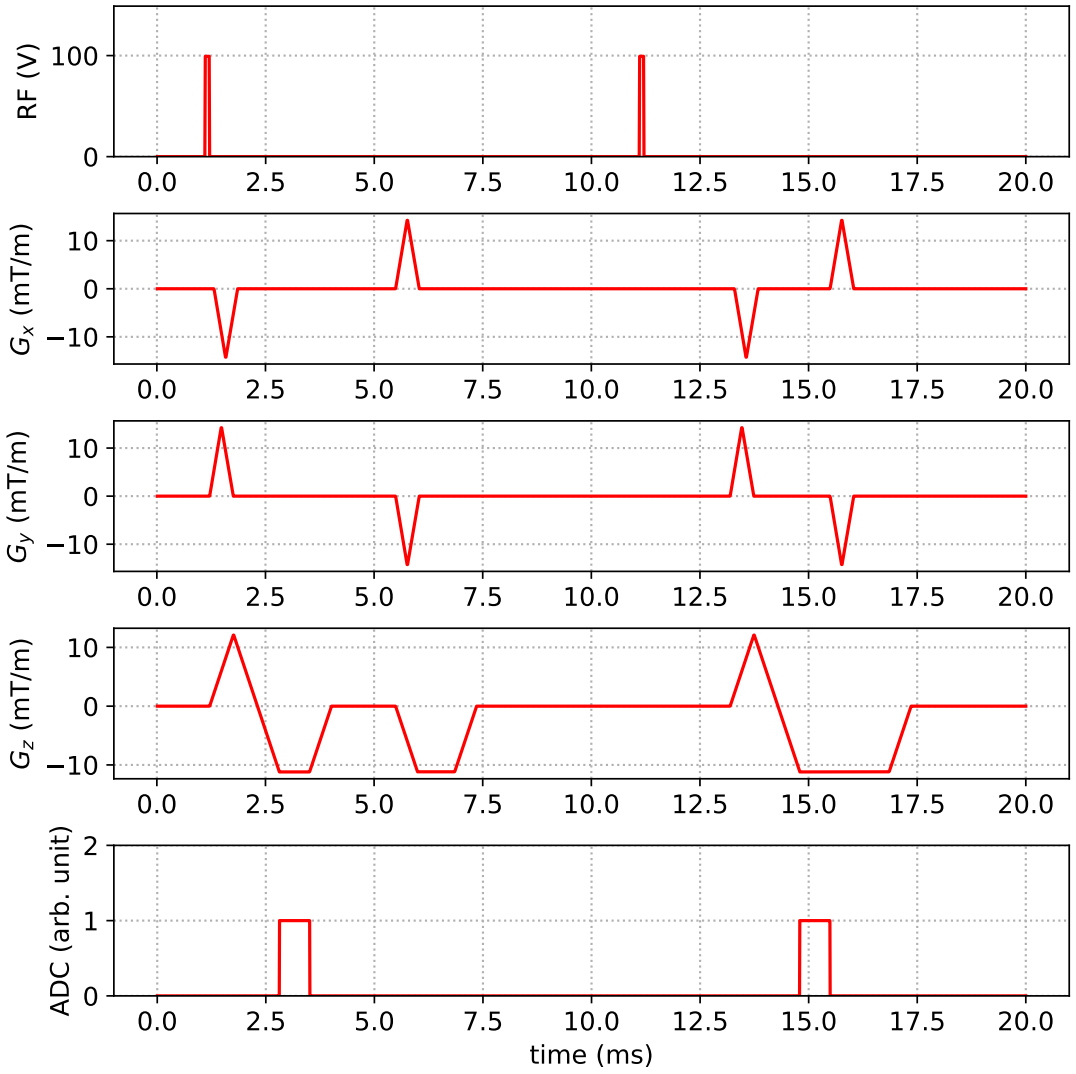

Figure F.3: A section of the sequence after increasing the rise times and decreasing the amplitudes of all gradients. The sinc pulse was also changed to a rectangular pulse. The gradient max amplitude of the read spoiler and readout gradient is now equal. TR=10 ms, TE_1=2.00 ms and TE_2=3.98 ms.

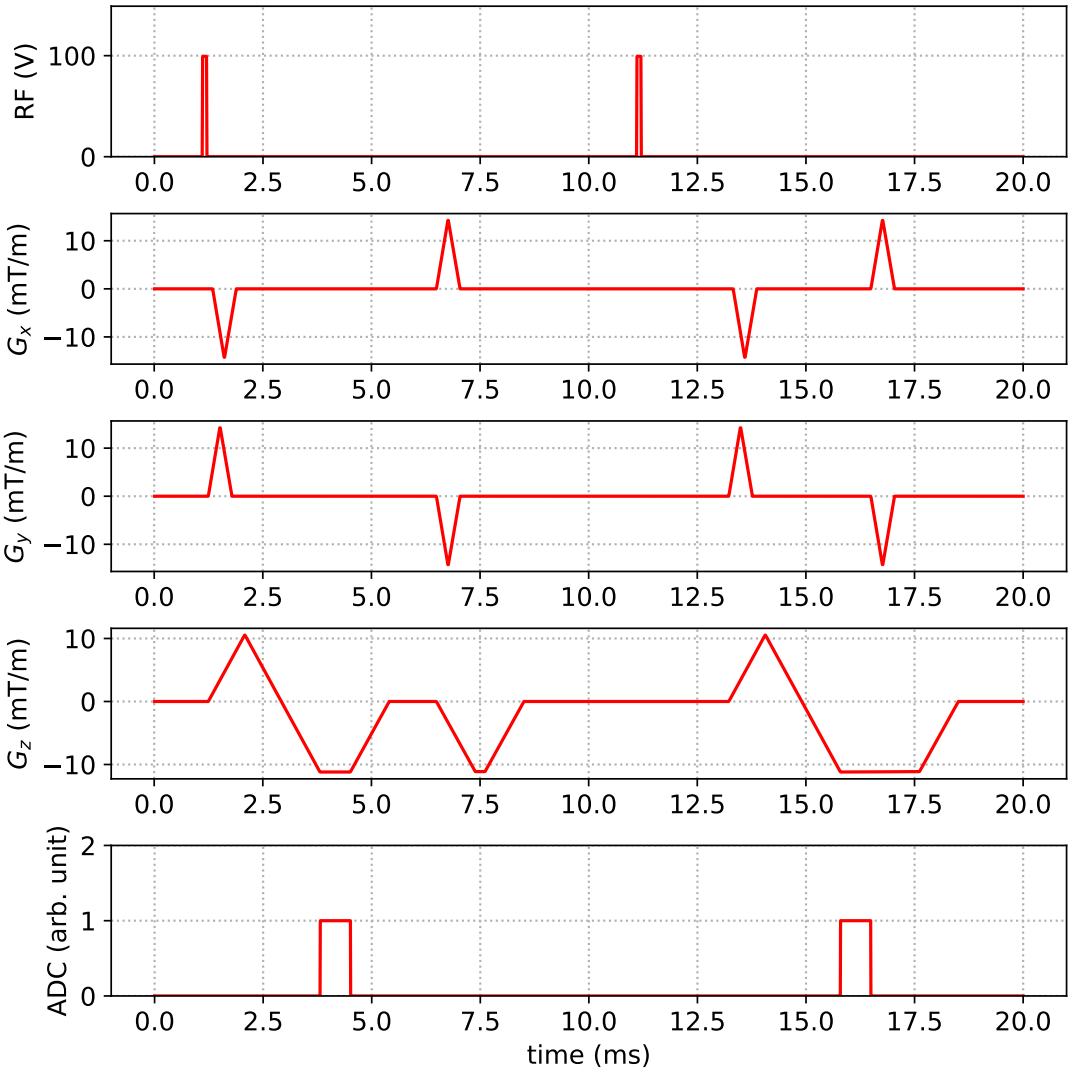

Figure F.4: A section of the final B_0-mapping sequence. An additional increase in rise times for gradients in the readout direction is done. TR=10 ms, TE_1=3.00 ms and TE_2=4.98 ms.

Appendix G

Data from B_0-validation

Table G.1: Statistical data from field map comparison. Mean and standard deviation (Sdd) are from the ΔB_0 inside the phantom mask. The last column shows the number of voxels inside this mask.

Sequence	Coil	Mean (μT)	Sdd (μT)	No. of voxels
New	32ch	0,18	0,18	82171
New	TU	0,15	0,08	77805
Siemens	32ch	-0,23	0,56	74511
Siemens	TU	-0,26	0,54	72373

Appendix H

Data from TR-experiments

Table H.1: Statistical data from the four TR-experiments. $\langle \Delta B^{diff} \rangle$ and Sdd is the mean and standard deviation of ΔB^{diff} inside the mask.

Experiment	TR (ms)	$\langle \Delta B^{diff} \rangle$ (μT)	Sdd (μT)
1	7	0,72	0,18
1	10	-0,51	0,08
1	15	0,10	0,12
1	20	0,43	0,03
1	25	-0,03	0,10
1	30	-0,09	0,04
1	35	0,02	0,03
1	40	0,12	0,02
2	7	-0,23	0,10
2	10	-0,26	0,05
2	15	0,05	0,05
2	20	0,06	0,01
2	25	0,00	0,01
2	30	-0,07	0,02
2	35	-0,02	0,01
2	40	0,01	0,01
3	7,6	-0,03	0,02
3	10	-0,05	0,02
3	15	0,04	0,01
3	20	0,03	0,01
3	25	-0,04	0,01
3	30	-0,03	0,01
4	7,6	-0,04	0,03
4	10	-0,05	0,02
4	12	-0,10	0,02
4	15	0,04	0,02
4	17	0,03	0,02
4	20	0,02	0,01

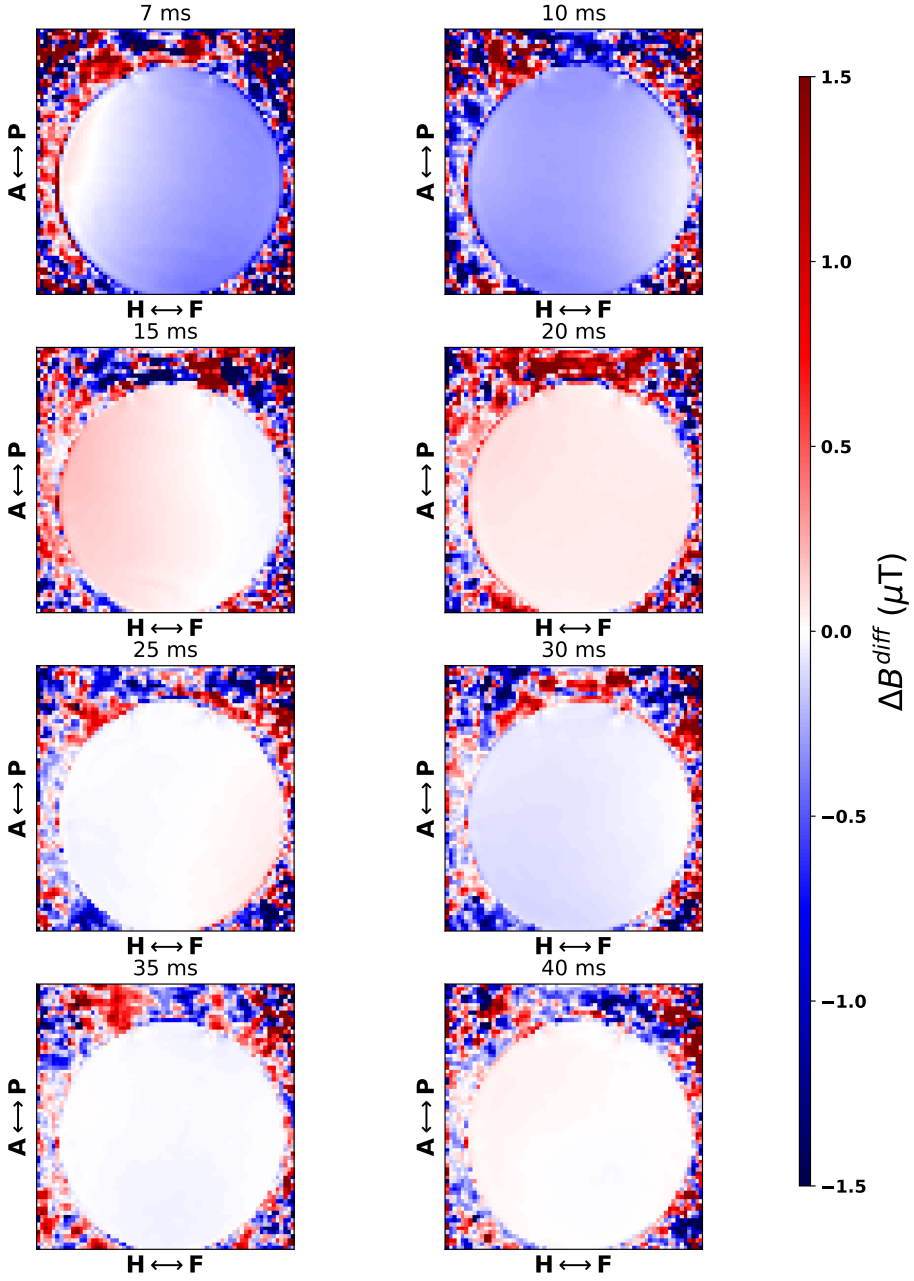

Figure H.1: Sagittal slices of the difference map ΔB^{diff} from the second TR-experiment. The repetition time for a given slice is displayed above it.

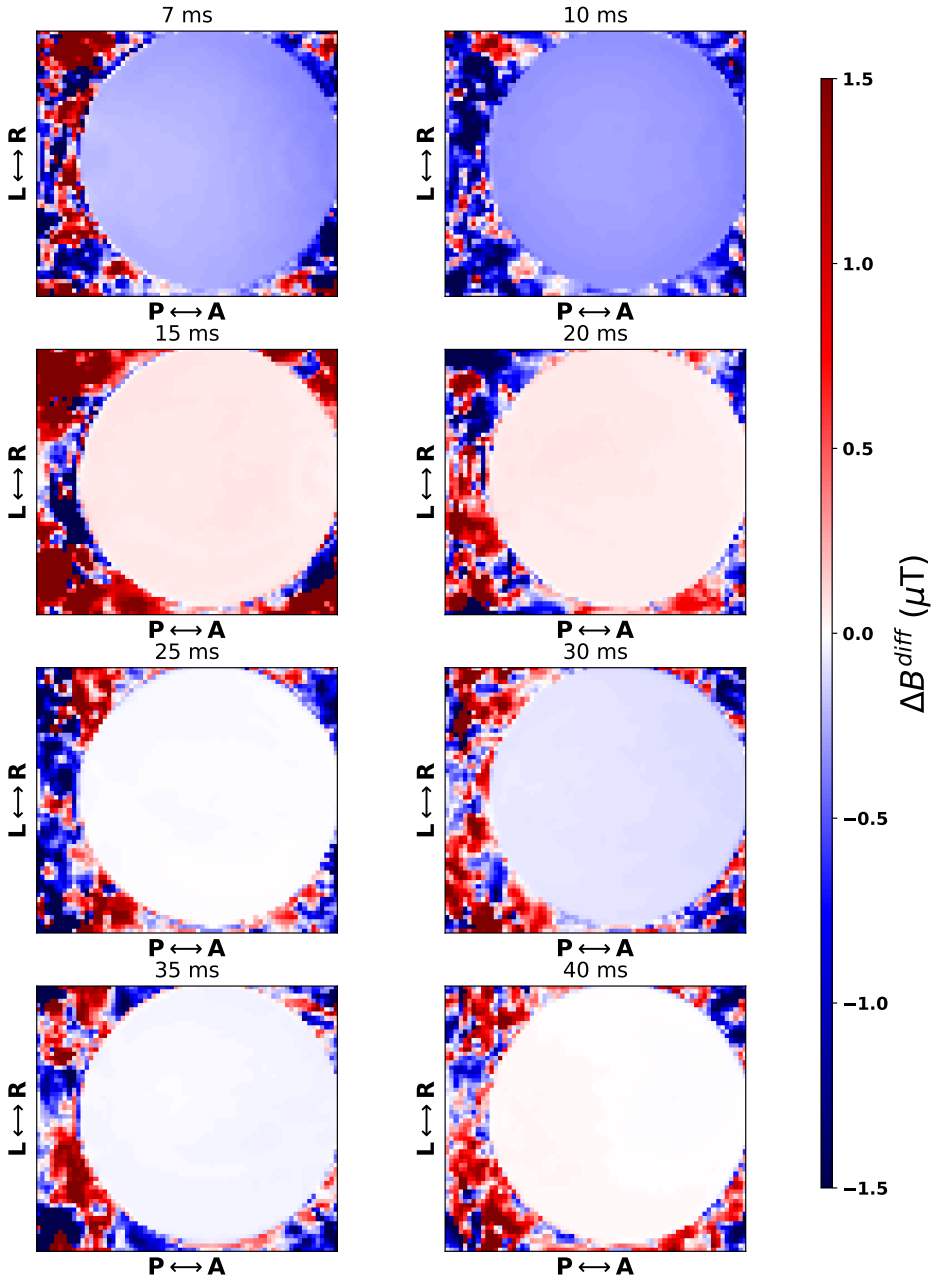

Figure H.2: Transverse slices of the difference map ΔB^{diff} from the second TR-experiment. The repetition time for a given slice is displayed above it.

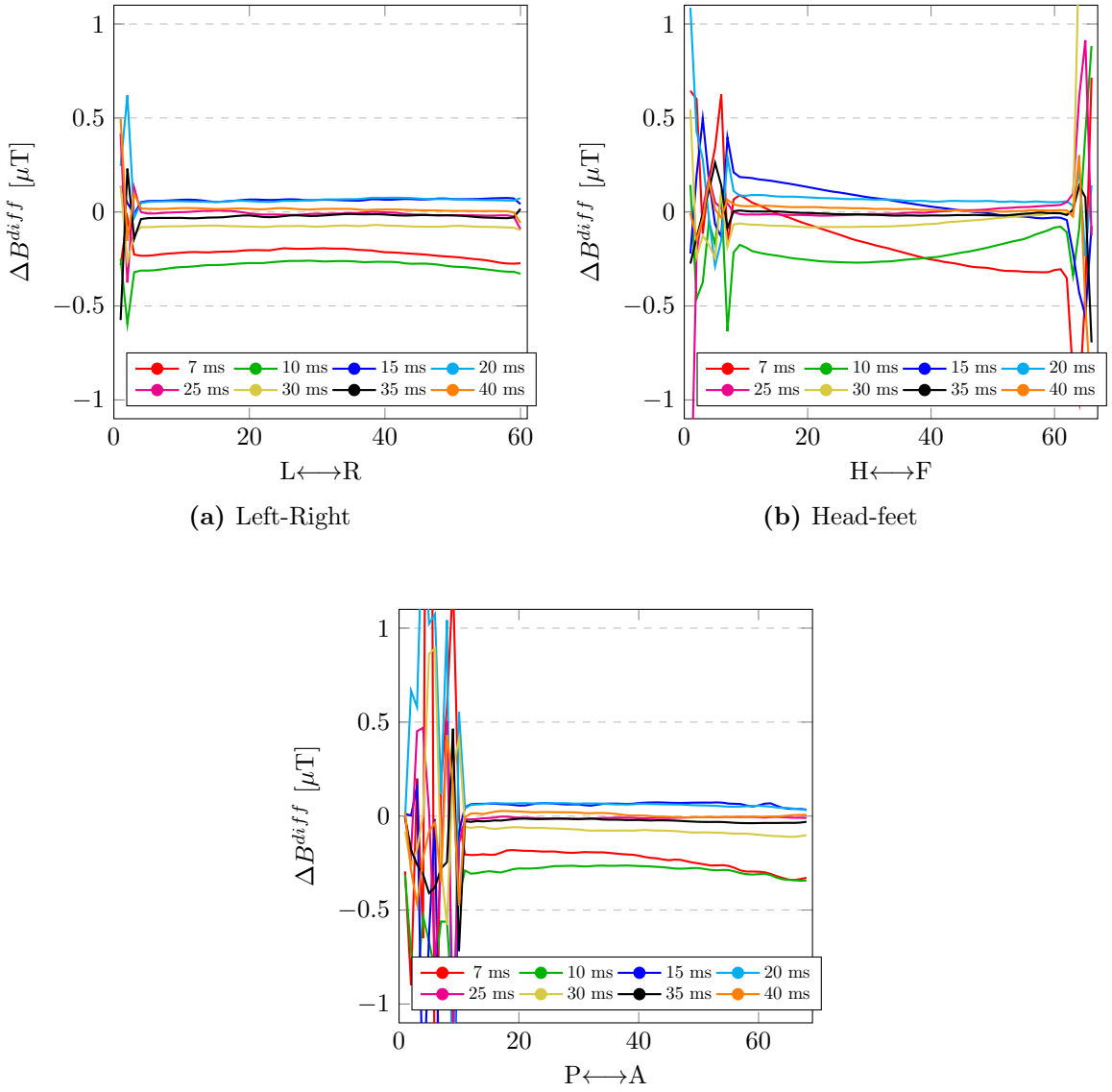

(a) Left-Right

(b) Head-feet

(c) Posterior-anterior

Figure H.3: Change of ΔB^{diff} across the center of the image for the second TR-experiment.

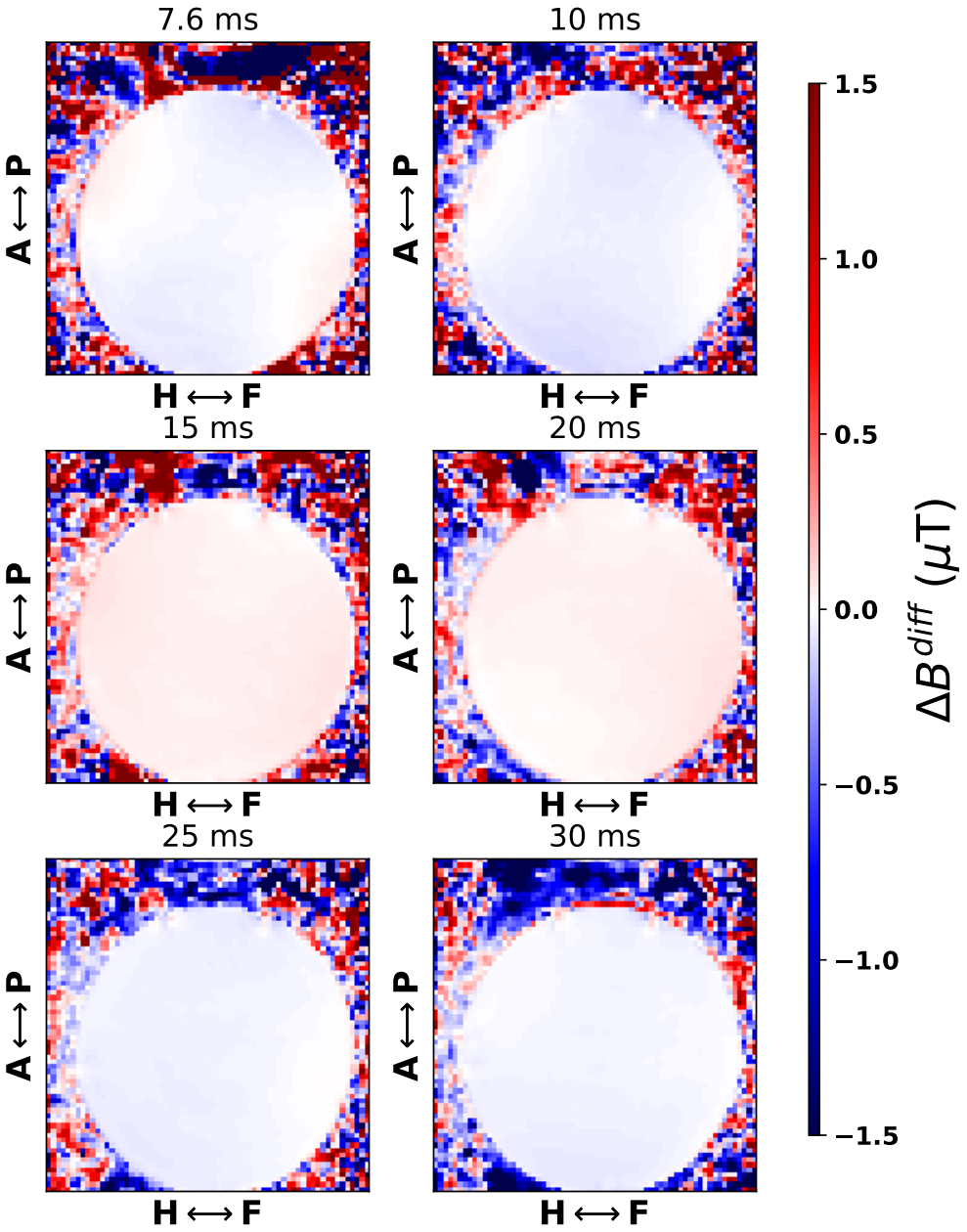

Figure H.4: Sagittal slices of the difference map ΔB^{diff} from the third TR-experiment. The repetition time for a given slice is displayed above it.

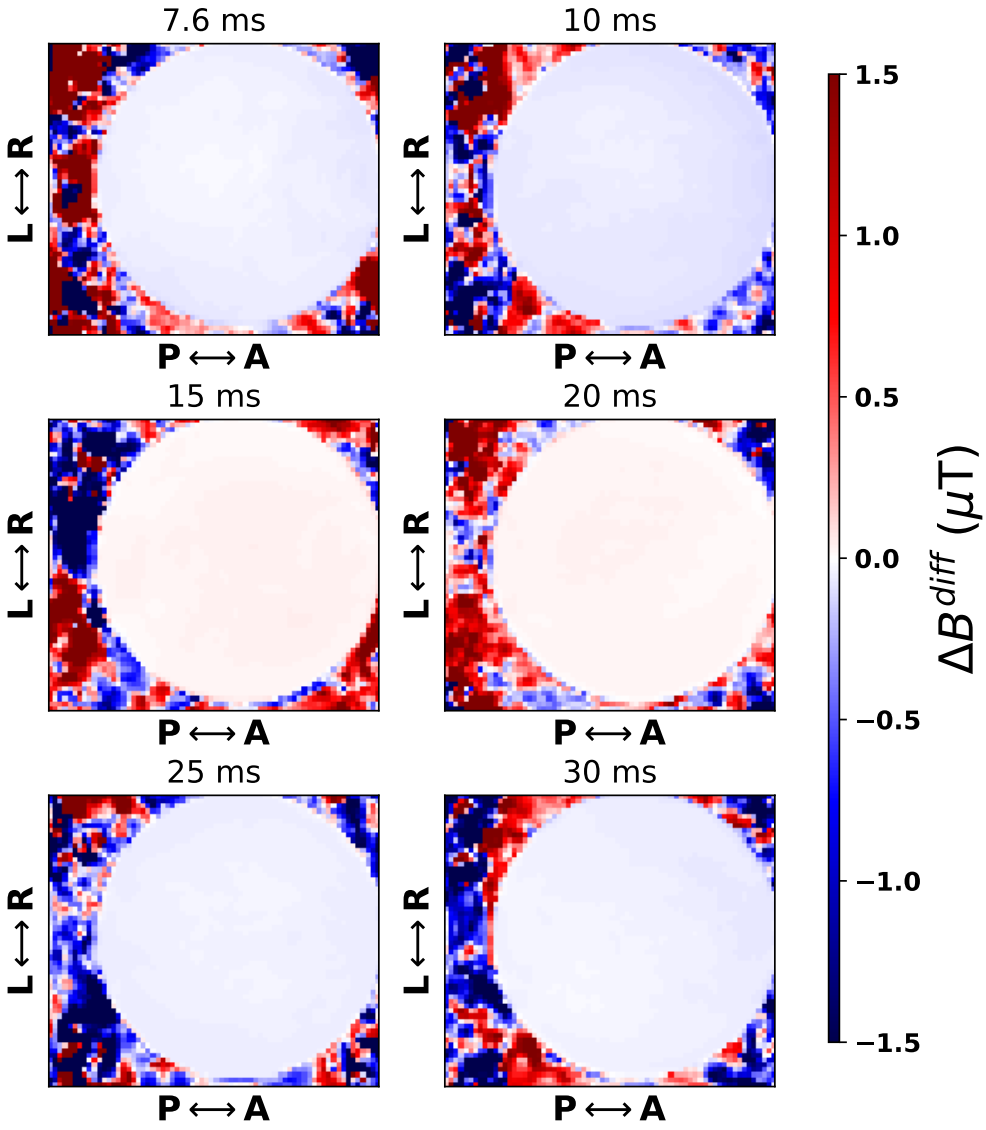

Figure H.5: Transverse slices of the difference map ΔB^{diff} from the third TR-experiment. The repetition time for a given slice is displayed above it.

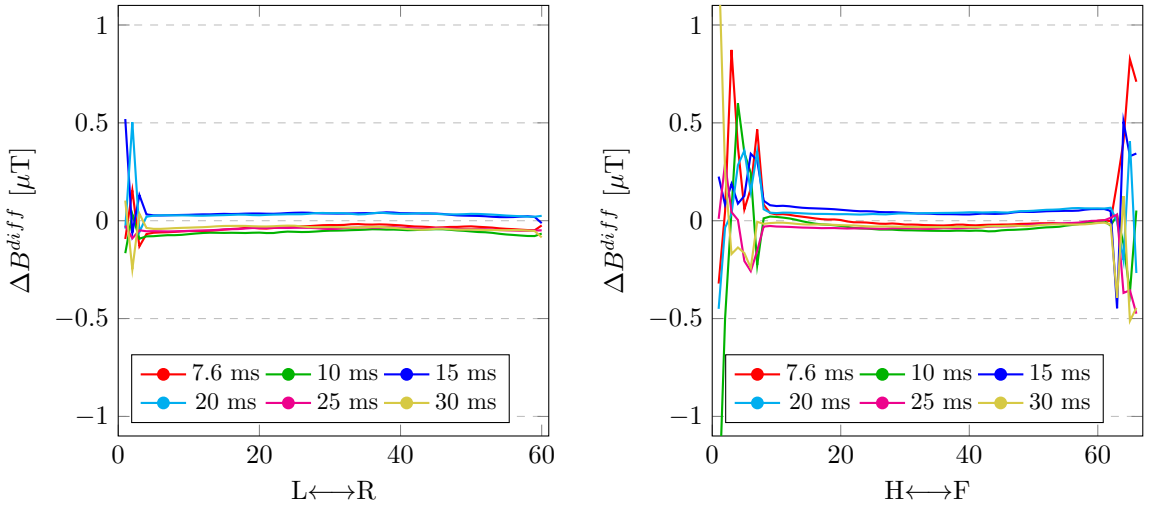

(a) Left-Right

(b) Head-feet

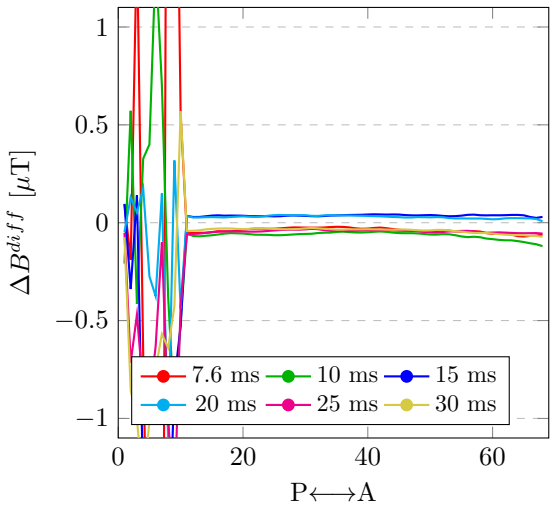

(c) Posterior-anterior

Figure H.6: Change of ΔB^{diff} across the center of the image for the third TR-experiment.

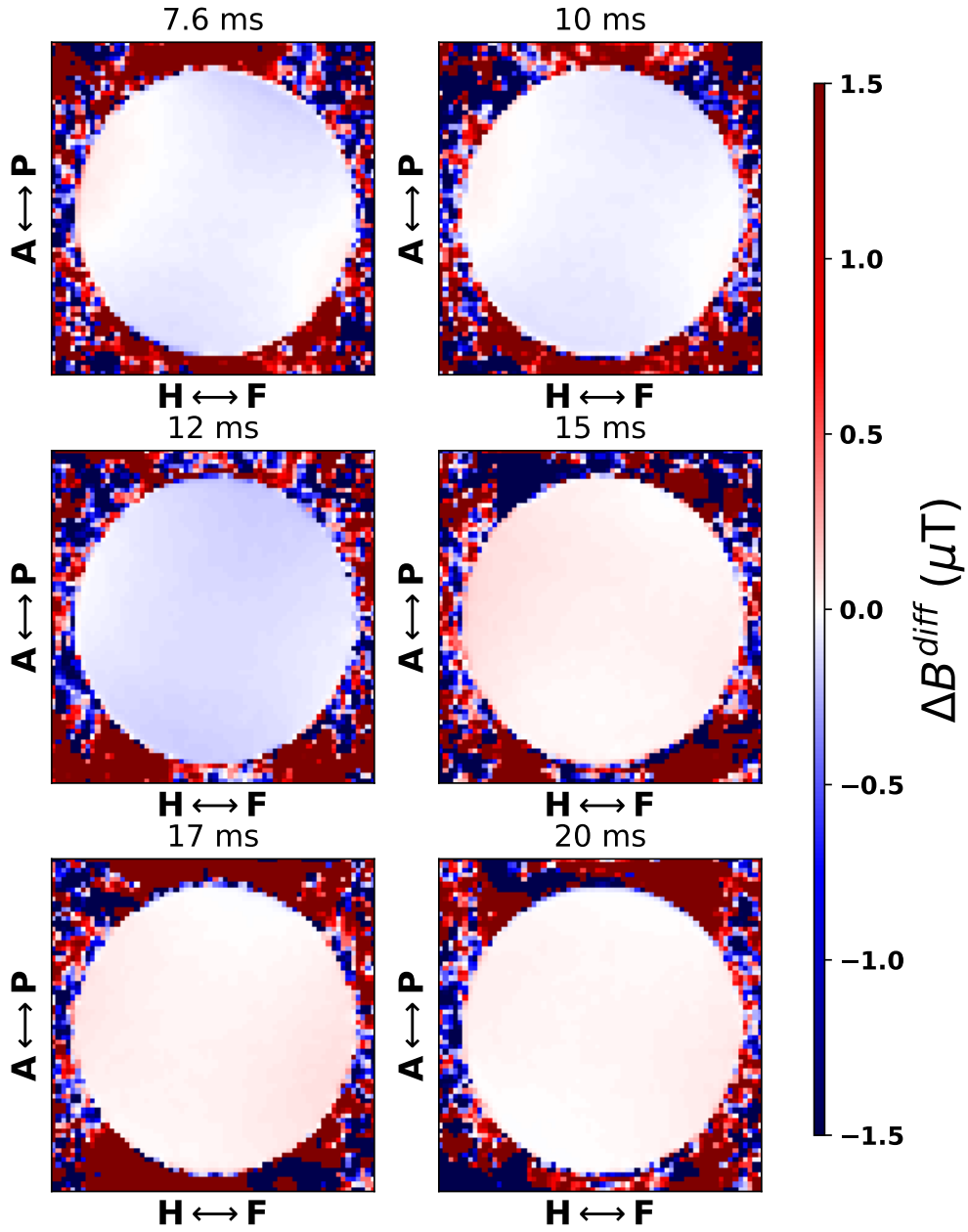

Figure H.7: Sagittal slices of the difference map ΔB^{diff} from the fourth TR-experiment. The repetition time for a given slice is displayed above it.

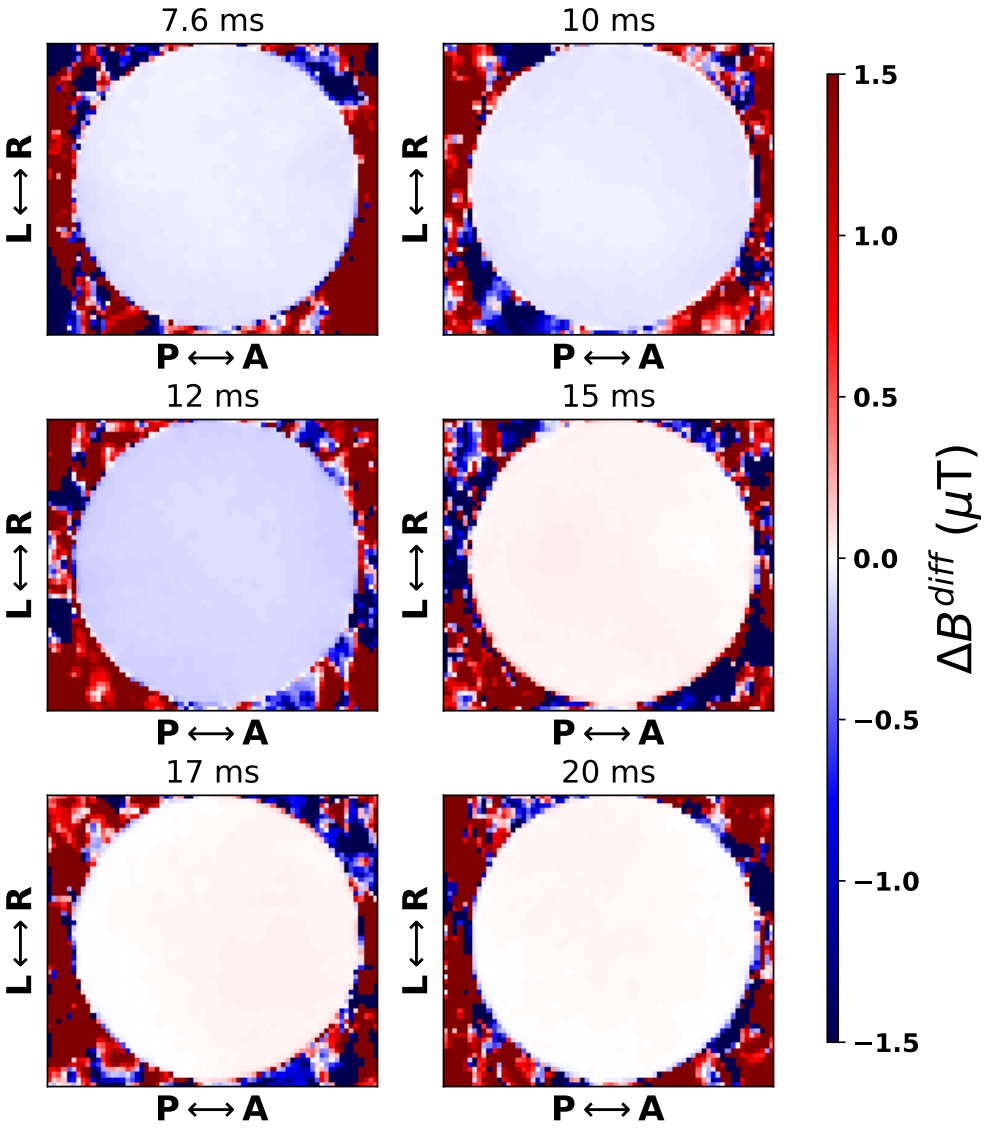

Figure H.8: Transverse slices of the difference map ΔB^{diff} from the fourth TR-experiment. The repetition time for a given slice is displayed above it.

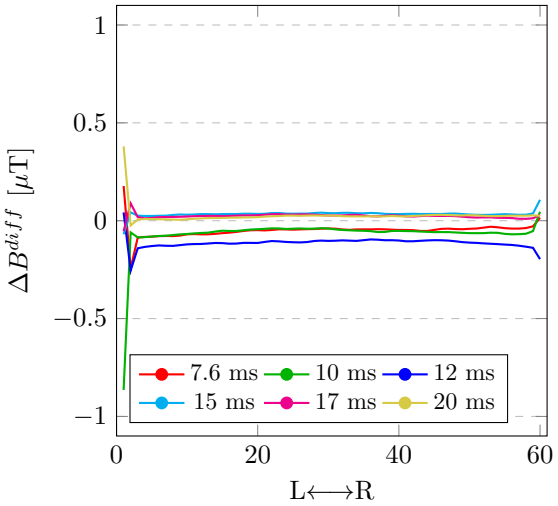

(a) Left-Right

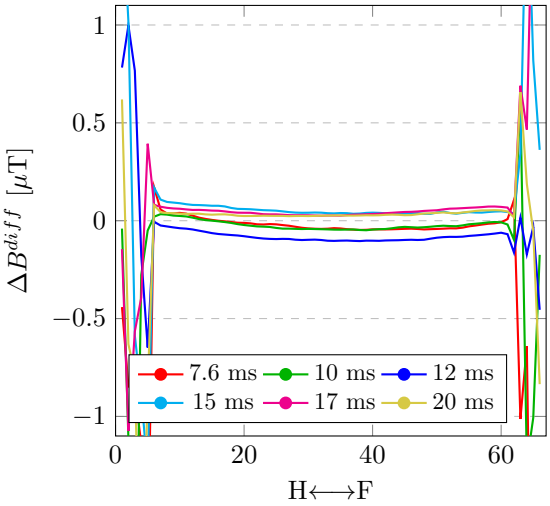

(b) Head-feet

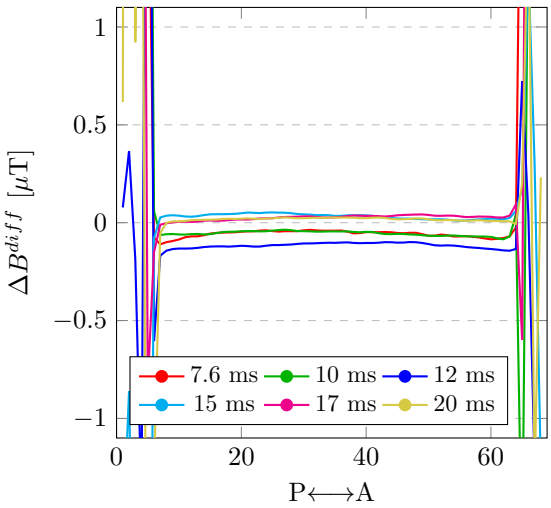

(c) Posterior-anterior

Figure H.9: Change of ΔB^{diff} across the center of the image for the fourth TR experiment.

Appendix I

Statistical data from shim comparison

Table I.1: Statistical data from the B_0-maps after applying the new shim method.

No	ID	Mean (Hz)	Sdd (Hz)	FWHM (Hz)	protocol
*1	a_1	9,5	67,7	23,4	tra
2	a_2	3,8	56,6	19,2	tra
3	a_3	8,0	55,5	19,7	tra
4	a_4	5,4	50,8	19,6	tra
5	a_5	6,0	51,8	19,6	tra
6	a_6	-11,2	63,4	23,7	sag
7	a_7	13,5	42,2	21,0	tra
8	a_8	4,7	61,4	27,2	tra
9	a_9	8,4	47,4	17,2	tra
10	a_{10}	8,7	71,4	22,2	sag
11	a_{11}	-2,5	56,6	29,8	sag
12	a_{12}	-4,6	53,4	20,5	sag
13	a_{13}	5,6	43,3	18,8	tra
14	a_{14}	5,9	49,8	22,7	tra
15	a_{15}	7,3	50,6	32,1	tra
16	a_{16}	11,1	44,3	20,5	tra
17	a_{17}	-3,8	62,5	23,9	sag
18	a_{18}	-2,9	53,4	22,9	sag
19	a_{19}	-6,1	47,4	14,4	sag

Table I.2: Statistical data from the B_0-maps after applying the standard shim.

No	ID	Mean (Hz)	Sdd (Hz)	FWHM (Hz)	protocol
27	c_1	-37,2	89,0	51,1	sag
28	c_2	-43,9	97,7	86,0	sag
29	c_3	-30,2	64,6	56,6	sag
30	c_4	-22,3	79,4	58,2	sag
□31	c_5	-8,0	64,6	30,2	tra
□32	c_6	-1,2	66,1	42,1	sag
33	c_7	-27,5	53,7	49,7	sag
34	c_8	-28,6	91,3	61,6	sag
35	c_9	-22,2	62,8	46,9	sag
36	c_{10}	-36,7	56,8	103,9	sag
37	c_{11}	-31,3	73,5	36,1	sag
38	c_{12}	-20,2	58,0	60,8	sag
39	c_{13}	-36,5	70,1	50,3	sag
40	c_{14}	-36,9	83,6	62,7	sag
△41	c_{15}	-16,8	64,8	57,3	tra
△42	c_{16}	-20,4	65,7	55,3	sag
♣43	c_{17}	-7,1	55,9	50,9	tra
▽44	c_{18}	-16,2	70,7	67,0	tra
⋆45	c_{19}	-50,8	98,3	90,7	tra

Table I.3: Statistical data from the B_0-maps after applying the standard shim iteratively.

No	ID	Mean (Hz)	Sdd (Hz)	FWHM (Hz)	protocol
◇20	b_1	-7,6	45,3	14,9	sag
◇21	b_2	15,4	44,2	20,1	tra
△22	b_3	-1,3	54,0	25,3	tra
△23	b_4	-9,0	54,7	21,2	sag
♣24	b_5	0,5	48,4	40,3	tra
▽25	b_6	-15,0	69,5	38,8	tra
26	b_7	-8,9	62,3	69,9	tra

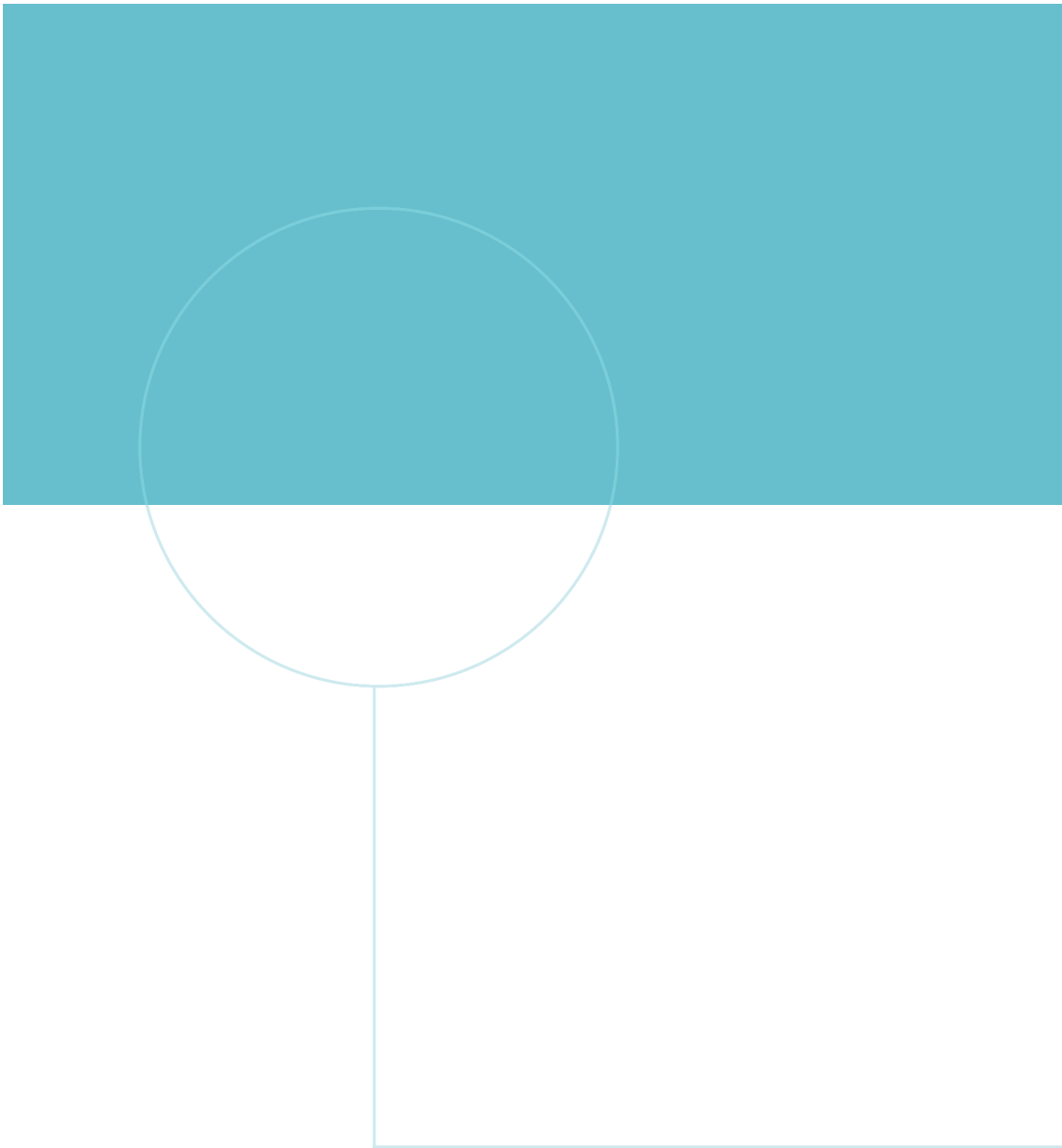

NTNU

Norwegian University of
Science and Technology